Understanding Nanoscale Hierarchical Nature of Pore and Chemical Heterogeneity in Bone as a Function of Tissue Ages

by

Taeyong Ahn

A dissertation submitted in partial fulfillment
of the requirements for the degree of
Doctor of Philosophy
(Macromolecular Science and Engineering)
in The University of Michigan
2020

Doctoral Committee:

Professor Ellen M. Arruda, Co-Chair
Professor Mark M. Banaszak Holl, Co-Chair, Monash University
Associate Professor Kenneth M. Kozloff
Assistant Professor Geeta Mehta
Professor Bradford G. Orr

Taeyong Ahn
tedahn@umich.edu
ORCID iD: 0000-0002-3664-4700

For those who suffer from mental health issues

There is no shame seeking help from institutions and/or your loved ones

There is no shame quitting your journey here and looking for other possibilities because you always have options

Do not measure and define your self-worth by a title or degree

When you have severe anxiety and self-doubt, please remember that you are not alone; you have your families and friends. They love you because of who you are, not because of what you are or what you are going to be

To my parents and Cathy & Steve

I must be the luckiest person in the world to have two sets of parents who love me dearly

Cathy & Steve: without your endless love, support and encouragement, I don't think I would have made this far

I am who I am because of you and you truly shaped my mind!

엄마, 아빠 지금까지 공부시켜 주셔서 너무 감사해요. 사랑해요!

ACKNOWLEDGEMENTS

I am thankful for so many people. I hope I will not miss any (if so, please forgive me)! First of all, I would like to thank my adviser, Dr. Mark Banaszak Holl. He taught me so many things about becoming a competent scientist; how to properly collect, interpret and process data, how to accurately present scientific findings and how to effectively prepare a manuscript (well, I think I am still working on that front). The one aspect of his advising I am most appreciative is his patience, especially for my writing or lack thereof. I still do not comprehend how he maintained his calmness for my last-minute abstract or paper submissions. He was always understanding and trying to accommodate my writing style (if there is any). I wish I could be as half calm and cool as you were for me when I work with my future colleagues! He showed me how to become a great mentor. But most importantly, he showed me how to become a decent person. I also thank him for the opportunity to research abroad at Monash University in Melbourne, Australia. To be honest, it was not the easiest time of my life, but it was one of the most transformative times for me. I never thought anything could really change me fundamentally after my college but my experience in Australia definitely did. To decide to join your lab was one of the best decisions I have ever made in my life. Thank you for everything!

I also like to thank my committee members. Dr. Ken Kozloff has been an integral part of my PhD journey. He has supported and advised me throughout my PhD process. He taught me a ton about bone biology and bone in general. I relied on his knowledge and expertise when I

encountered data sets that I had a hard time understanding. I really want to thank him for his optimism regarding my experiments and data. You were more optimistic about my data and me than I was about myself. I would like to thank Dr. Brad Orr for his advice throughout my PhD, especially on data analysis and instrumentation. Most importantly, I would like to thank him for connecting me to the PALS project. I never know how much further I was going to go with the PALS project, and I discovered more novel aspects of bone structure than I could possibly imagine. I would like to thank Dr. Ellen Arruda for being part of my dissertation committee and serving as the co-chair of my committee so I would maintain my status with the University of Michigan. You didn't have to do this for me, but you did it anyway. I really appreciate it! Lastly, I would like to thank Dr. Geeta Mehta for being part of my dissertation committee. Actually, this is her second time to be a part of committee for me; she was a part of my Macro 890 committee before. Also, she was one of the very first people I met when I toured the school. I still fondly remembered our interview.

I would like to thank Dr. David Gidley for his integral guidance and support for the PALS project. Without him, this project would have not happened. I was lucky to work with such an experienced and capable scientist side by side almost everyday. I was always inspired by his passion for science. He came to the lab and did experiments everyday not because he had to but because he loved doing them. I hope I can find a job that I will be that passionate about in the future.

Next, I would like to thank my awesome labmates from the Banaszak Holl lab. I couldn't have asked better labmates. Sriram and Meagan convinced me to join the lab initially and you guys were right! JJ and Rachel; you were a great example as a scientist and friend. I wish I could be as half capable as you guys! Jinhee; we moved to a different continent together. I will never

forget our journey together. Isabel; I still remembered the first time I met you during the summer term. That day, not only did I meet a great colleague but also, I met my dear friend. You were always here for me when I needed a person to talk to. Also, I would like to thank Dr. Jing Zhang at Monash University. Jing; I hope I didn't complain too much during our lunch time.

I would like to thank my labmates from the Kozloff lab. Rachel; you were always so nice to me. I can't wait to work with you at IU and share some draft beer together! Chris; thank you for all help in terms of animal preparation or instrumentation! Diana; from the day one, you made feel like a part of ORL. Without you, I honestly don't know how I would have fit in the new environment. Daniella; I remember our first beer session (and one of many) with Diana and I think it lasted for about 4 or 5 hours. It was the moment I knew I belonged to ORL. Hope you will be in town during May to join my last "Tour de Fries!"

ORL has been an integral part of my research. I would like to thank everyone in ORL who assisted me to conduct my experiments. Especially, I would like to thank Carole for helping me with bone sectioning, Bonnie for helping me handle mice, and Erin for helping me with the ashing experiment.

Macro is truly family-like. Even though we are spread, we stick together. I would like to thank everyone from Macro. Especially, I would like to thank Harry and Leanna. I was so lucky to meet you and we hung out for over three years. We went through so many ups and downs together. I am so glad to see you guys are doing great after school.

I would like to thank my parents. They sacrificed their whole lives to support me so I would have a chance to study in this gracious nation, which was never given to them. They work tirelessly and I hope to follow their work ethic.

Last, (but, definitely not least), I would like to thank Cathy and Steve. When I first met you guys, I wasn't sure I was good enough to go to any college in the US. I can't believe we spent over almost 13 years together. I was a boy when I entered your house for the first and now, I will be 31 years old pretty soon! Thank you for everything!

TABLE OF CONTENTS

LIST OF FIGURES

LIST OF TABLES

LIST OF APPENDICES

LIST OF ABBREVIATIONS

Atomic Force Microscopy = AFM

Atomic Force Microscopy-Infrared Spectroscopy = AFM-IR

Brunauer-Emmett-Teller = BET

Electron Microscopy = EM

Ellipsometric Porosimetry = EP

Energy-dispersive X-ray = EDX

Fourier-transform Infrared Spectroscopy = FTIR

Mean Free Path = MFP

Non-local Density Functional Theory = NLDFT

Nuclear magnetic resonance spectroscopy = NMR

One-way Analysis of Variance = ANOVA

Optical Photothermal Infrared Spectroscopy = O-PTIR

Osteogenesis Imperfecta = OI

Ovariectomized = OVX

Photothermal Infrared Spectroscopy = PTIR

Poly(methyl methacrylate) = PMMA

Pore Size Distribution = PSD

Positron Annihilation Lifetime Spectroscopy = PALS

Scanning Electron Microscopy = SEM

Scanning Transmission Electron Microscopy = STEM

Small Angle Neutron Scattering = SANS

Specific Surface Area = SSA

Transmission Electron Microscopy = TEM

Wild Type = WT

X-ray Diffraction = XRD

ABSTRACT

Bone is a biocomposite material mainly composed of two major components (Type I collagen and hydroxyapatite crystals) and it is constructed in a hierarchical fashion ranging from a nano to macro scale. Bone has been known to have nanoscale mechanical heterogeneity, which is proposed to enhance bone toughening, but the underlying reasons for the nanoscale mechanical heterogeneity are unknown. Nanoscale bone structure and chemical composition are hypothesized to contribute to the nanoscale mechanical properties of bone. However, until recently, measuring nanoscale porosity and chemical composition in bone was not feasible due to a lack of appropriate characterization techniques. In this thesis, two novel characterization techniques, PALS (positron annihilation lifetime spectroscopy) and PTIR (photothermal infrared spectroscopy), were utilized and elucidated new structural and chemical information that were unknown to the field: 1) Bone has a hierarchical arrangement of nanoscale pores in bone; 2) The nanoscale mineral structure in bone is likely to be interconnected; and 3) The Amide I/mineral domain sizes range from ~50 to 500 nm, which agrees with the length scale of nanoscale mechanical maps.

PALS has never been utilized to study nanoscale porosity in bone. Combining our PALS results with simulated pore size distribution (PSD) results from collagen molecule and microfibril structure, we identify pores with diameter of 0.6 nm that indicates porosity within the collagen molecule regardless of the presence of mineral and/or water. We find that water occupies three larger domain size regions with nominal mean diameters of 1.1 nm, 1.9 nm, and

4.0 nm—spaces that are hypothesized to associate with inter-collagen molecular spaces, terminal segments (d-spacing) within collagen microfibrils, and interface spacing between collagen and mineral structure, respectively. We revealed that similar to collagen and mineral structure, nanoscale porosity in bone is also constructed in a hierarchical fashion. Also, PALS data on the deproteinized bone samples showed an average spacing value between two mineral plates ranging from 5-6 nm, suggesting that the nanoscale mineral structure itself is likely to be interconnected. Combined with specific surface area (SSA) and PALS measurements, a range on the mean mineral plate thickness is deduced to 4-8 nm, which agrees with electron microscopy (EM) studies in literature.

PTIR is further divided into two techniques, depending on the probe methods for signal detection; 1) atomic force microscopy-infrared spectroscopy (AFM-IR) and optical photothermal infrared spectroscopy (O-PTIR). We found that the average Amide I/mineral ratio values from AFM-IR decreased as a function of tissue ages, agreeing with the general mineralization trend measured for comparable tissue ages by Raman spectroscopy. However, in addition to the agreement of the average Amide I/mineral ratio values between AFM-IR and Raman spectroscopy, the Amide I/mineral ratio values calculated from full IR spectra and IR ratio maps collected by AFM-IR revealed reduced Amide I/mineral ratio ranges, as a function of tissue age, demonstrated by decreasing box and whisker ranges. Even though we found an overall decrease in average Amide I/mineral ratio values and ranges across the different bone samples, the Amide I/mineral ratio values from AFM-IR and O-PTIR exhibited location to location and sample to sample variations of the IR ratio values. Also, we discovered that the domain size range of the Amide I/mineral ratio maps (~50 to 500 nm) has the same length scale as nanoscale mechanical maps.

Chapter 1

Introduction: Current Limitations of Understanding Nanoscale Bone Structure and Chemical Composition and Novel Approaches to Overcome Them

1.1 Abstract

Bone is a biocomposite material constructed in a hierarchical fashion ranging from a nano to macro scale and mainly consists of two components; Type I collagen (providing toughness) and hydroxyapatite crystals (providing stiffness). The nanoscale structures of collagen and hydroxyapatite crystals have been extensively studied by characterization techniques such as Atomic force microscopy (AFM), transmission electron microscopy (TEM), and X-ray Diffraction (XRD). However, the nanoscale pore structure below the mineralized collagen fibril level in bone has been poorly understood due to a lack of a characterization technique. For the first time, positron annihilation lifetime spectroscopy (PALS) was used to systematically study porosity profiles for individual bone components (pure collagen, pure mineral, and dehydrated collagen and mineral). Similar to a lack of a nanoscale porosity measurement, studying chemical composition at the nanoscale has been limited because of the spatial resolution (~10 μm) of conventional Fourier-transform infrared spectroscopy (FTIR). Two novel spectroscopy techniques, atomic force microscopy (AFM-IR) and optical photothermal infrared spectroscopy (O-PTIR), were employed to characterize how average, range and domain size of Amide I/mineral ratio values change as a function of tissue age.

1.2 Hierarchical nature of bone construction

Bone is a biocomposite material constructed in a hierarchical fashion ranging from a nano to macro scale.[1–4] Bone mainly consists of two components; Type I collagen and hydroxyapatite crystals.[5–7] The collagen and mineral components provide toughness and stiffness, respectively. Bone possesses optimized mechanical properties of both components; simultaneously being tough and strong.[6] These remarkable bone mechanical properties stem from its complex composite structure as shown in Figure 1.1.[1]

1.2.1 Collagen structure

Collagen is the most abundant structural protein found in animals[8,9] and specifically, ~70 % of all collagen is Type I collagen extensively utilized for constructing tissues such as bone, tendon, skin, teeth and cornea.[10] Collagen molecule is composed of three polypeptide chains with the typical amino acid sequence of Gly−X−Y, where X is most likely proline and Y is most likely hydroxyproline.[8] To understand how collagen molecules could be arranged into more complex collagen fibril, Petruska and Hodge proposed a model where collagen molecules are staggered to form a two-dimensional collagen structure with a regular 67 nm repeating unit by employing various physical-chemical data from X-ray diffraction (XRD) and scanning electron microscope (SEM).[11] Orgel at al. provided a fully three-dimensional structure of collagen molecule and provided a model for how five collagen molecules are arranged to construct a collagen microfibril structure based on experimentally determined XRD data.[12]

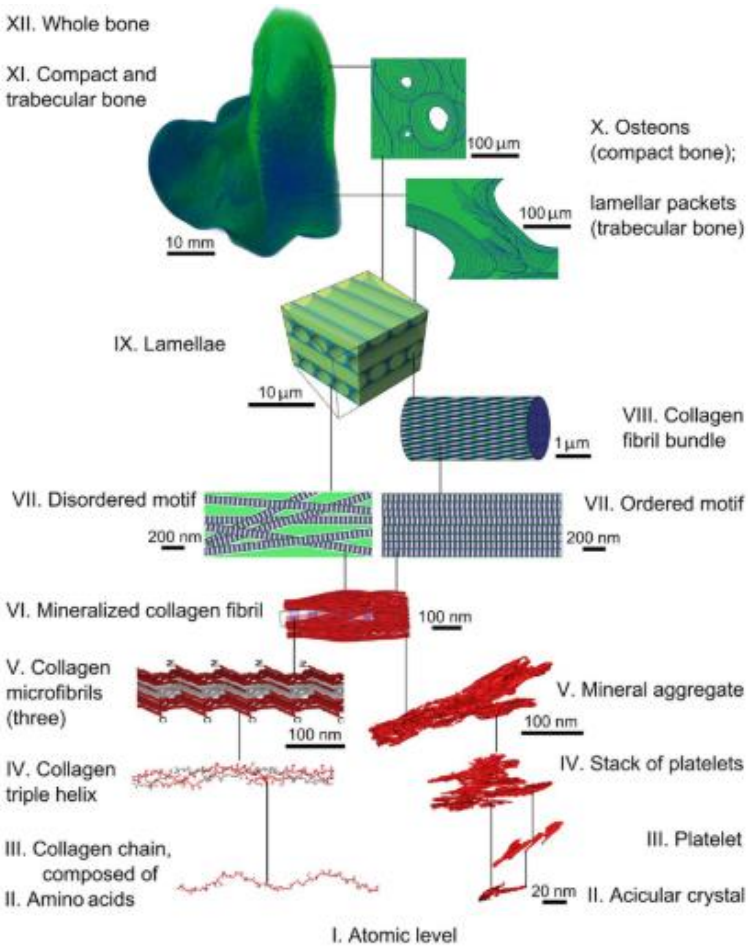

Figure 1.1 A schematic showing the hierarchical construction of bone structure from a nano to macro scale.[2] Both collagen and mineral components are built from the atomic level and formed into the mineralized collagen fibril, which is the basic building block of bone. Reprinted with permission; Copyright 2018 Science.[2]

1.2.2 Mineral structure

Unlike the general consensus of the collagen structure and sizes in bone, the reported physical dimensions of mineral crystals (length = 15-50 nm; width = 2-30 nm, and thickness = 0.6-10 nm) widely vary, depending on material characterization techniques (atomic force microscopy (AFM)[13], transmission electron microscopy (TEM)[14,15] and X-ray diffraction (XRD)[16–18]), sample preparation, tissue locations and animal species.[19] Historically, the shape of the mineral crystals has most commonly been proposed to follow a plate model.

1.2.3 Mineralized collagen fibril structure

The mineralized collagen fibrils are thought to be in the form of two collagen microfibrils engulfing the mineral plates.[6,20,21] However, recently published work by Reznikov et al. with high-resolution 3D scanning transmission electron microscopy (STEM) tomography favors an acicular shape and suggests that the acicular shape mineral crystals are merged into a platelet and eventually formed into aggregates of platelets with a complex irregular 3D shape. Also, their study suggests a different model of the mineralized collagen fibrils; instead of the traditional sandwich model of the mineralized collagen fibrils (an alternate order of parallel oriented mineral plates and collagen microfibrils), the collagen microfibrils and the mineral aggregates form a complex mineral-collagen structure where the mineral occupies inter-fibrillar space.[2]

1.3 Current characterization techniques for measuring bone structure and chemical composition

1.3.1 Current methods to measure bone structure

Tai et al. demonstrated with an AFM based nanoindentation technique that bone possesses nanoscale mechanical heterogeneity within a length scale of the mineralized collagen fibrils. The nanoscale mechanical heterogeneity in bone is proposed to play an import role in damage evolution and bone toughening. However, the underlying factors contributing to this nanoscale mechanical heterogeneity are poorly understood. Local structural and chemical variations are attributed to the nanoscale bone properties.[22]

Electron microscope (EM) methods such as TEM or SEM have been employed to measure the physical dimensions of the collagen fibril structure.[2,23–25]. With TEM technique, Starborg et al.[25] demonstrated a distribution of varying collagen diameter values and Quan and Sone[26] measured a periodic pattern of the collagen fibrils or D-spacing values to be 64.8 and

68.0 nm for skin and rat tail tendon respectively. However, the limitation of EM techniques is that it requires staining to achieve an image contrast. The electron density patterns constructing the image contrast are typically not directly registered with the collagen fibril structure. Rather, the electron density patterns reflect the electron density resulting from negative or positive stain.[27] In addition to EM, XRD has been used to characterize the collagen fibril structure. Orgel et al. constructed a full average collagen molecule structure for the first time, based on their XRD data. Also, they showed that average D-spacing value is 67 nm, which agrees with the Hodge–Petruska model. Their XRD study found the collagen microfibril coordinates, revealing how five collagen molecules construct a single collagen microfibril.[12] A recent XRD study performed by Roschger et al. demonstrated that depending on modelling and remodeling sites in bone, the mineral crystals have different thickness values; mineral crystals from the modelling sites are distinctly larger.[28] However, since XRD averages its signal over a certain volume, it cannot recognize a size variation resulting from individual collagen fibrils in bone.

AFM possesses a spatial resolution that can detect the individual mineralized collagen fibril level and physically measures surface topography with an AFM tip. AFM has been extensively applied to measure the mineralized collagen fibril morphology. Wallace et al. showed AFM could be used to study the nanoscale collagen morphology and demonstrated that the mineralized collagen fibrils or the collagen fibrils without the mineral components from teeth, bones and tendons have a distribution of D-spacing values rather than a single fixed D-spacing value as reported by previous TEM and XRD studies measuring average values.[29] Fang et al. further studied the D-spacing variation with respect to a collagen bundle rather than a single collagen fibril with skin, tendons and bones. They found that within a single fibril bundle, there is ~1 nm D-spacing variation. However, there exists a larger (~10 nm) D-spacing range

among different fibril bundles.[30] Not only is there a variation of D-spacing values in healthy tissues, the distribution of the D-spacing value is altered by diseases such as estrogen depletion and osteogenesis imperfecta (OI).[31,32]

Porosity in materials plays an important role in affecting mechanical properties. Especially, materials with pores can locally undergo a stress concentration, initiating crack formation and eventually leading to crack propagation and structural failure. Like other materials, bone also contains pores. Cortical bone presents two major size ranges of pore networks; the macroscopic osteonal and Volkmann canals (50-100 μm) that allow blood vessels and nerves to travel longitudinally and transversely across the bone respectively[33], and the microscopic lacuna-canalicular spaces (100-200 nm) that host the osteocytic network.[34] Currently, pores in a micrometer level are measured by a μ-CT technique. Bala et al. showed that even though the overall pore volume (measured using an 8.7 μm voxel size) does not differ between children and adults, adult bone exhibits a different pore network microarchitecture, including pore number, as compared to children. Pore network differences that result from lifetime bone remodeling may affect compressive and shear mechanical behavior in bone.[35] Weight-bearing bones such as the femur are shown to have a different pore microstructure (measured using 0.7 μm voxel size), compared to non-weight-bearing bone.[34] Microscopic pore structure changes with age and anatomical location and may also play a role in bone mechanical properties. Despite the important role that microscopic pore structure plays in bone biology and mechanical properties, the nanoscale pore structure in bone has been poorly understood unlike the relatively well-studied collagen and mineral structure on a nano scale by the TEM, XRD and AFM techniques mentioned above. With its ability to measure pores at the

sub-nanometer level, positron annihilation lifetime spectroscopy (PALS) provides a unique opportunity to probe the nanoscale structure in bone.

1.3.2 Current methods to measure bone chemical composition

Ove the years, researchers employed vibrational spectroscopy techniques such as Fourier-transform infrared spectroscopy (FTIR) and Raman spectroscopy to characterize chemical composition of various biological tissues such as bone, cartilage, and dentin.[36–39] There are three major material parameters typically used to assess bone quality by FTIR; mineral to matrix ratio, mineral maturity/crystallinity, and collagen maturity.[37] In this dissertation, the mineral to matrix ratio will be a key parameter to assess nanoscale chemical changes as a function of different tissue ages and genotypes. Recently, Hunt at al. showed cancellous bone samples from male patients with type 2 diabetes have a 7% higher mineral to matrix ratio value than bone samples without type 2 diabetes.[40] Gourion-Arsiquaud et al. revealed that bone samples from fractured femoral neck exhibited a significantly reduced level of chemical heterogeneity of mineral to matrix ratio values compared to bone samples from cadavers with no fracture history.[41] However, due to the spatial resolution limit of the conventional FTIR of ~10 μm[42], measuring chemical compositional changes smaller than the lamellae level (See Figure 1.1) has been limited. Another major limitation of conventional FTIR microscopy is that the technique needs a sample to be dehydrated in order to obtain a transmitted signal. With the invention of new types of photothermal infrared spectroscopy (PTIR) techniques (1. atomic force microscopy-infrared spectroscopy (AFM-IR) and 2. optical-photothermal infrared spectroscopy (O-PTIR)), obtaining chemical compositional information at the mineral collagen fibril level with fully hydrated bone samples is now possible.

1.4 Principle of positron annihilation lifetime spectroscopy (PALS) and its application for studying biological tissues

PALS is a porosity measuring technique with a nominal probe range of ~0.3 to 30 nm.[43] PALS has been extensively studied and used for 30 to 40 years in various material types such as metals, semiconductors[44] and polymers[45,46] to detect monovacancies and small vacancy clusters.

As shown in Figure 1.2, positrons (e^+) created from a radioactive source, such as Na^{22}, move into a sample. Due to the small size of the positrons, a sample does not need a porosity structure interconnected with the surface, unlike gas-based porosimetry techniques. When a positron encounters a preexisting electron (e-) in pores, both positron and electron combine and create an unstable state called positronium (Ps). Depending on a particular spin state of the positron and electron, there are two Ps lifetimes; one is *para*-Ps for the opposite spin state (the maximum lifetime is 0.125 ns), and another is *ortho*-Ps for the same spin state (the maximum lifetime is 142 ns). For the bulk PALS technique mainly used in this dissertation, the *ortho*-Ps lifetime is what is measured. When Ps is formed in an "infinitely" large pore (larger than 30 nm), the maximum Ps lifetime is 142 ns. As a pore size becomes smaller, the Ps lifetime decreases (i.e. the larger the pores, the longer the lifetime and the smaller the pores, the shorter the lifetime). In addition to the lifetime information (pore size values), PALS provides Ps lifetime intensity values. These intensity values provide a relative population of pores corresponding to specific Ps lifetimes.[43,46]

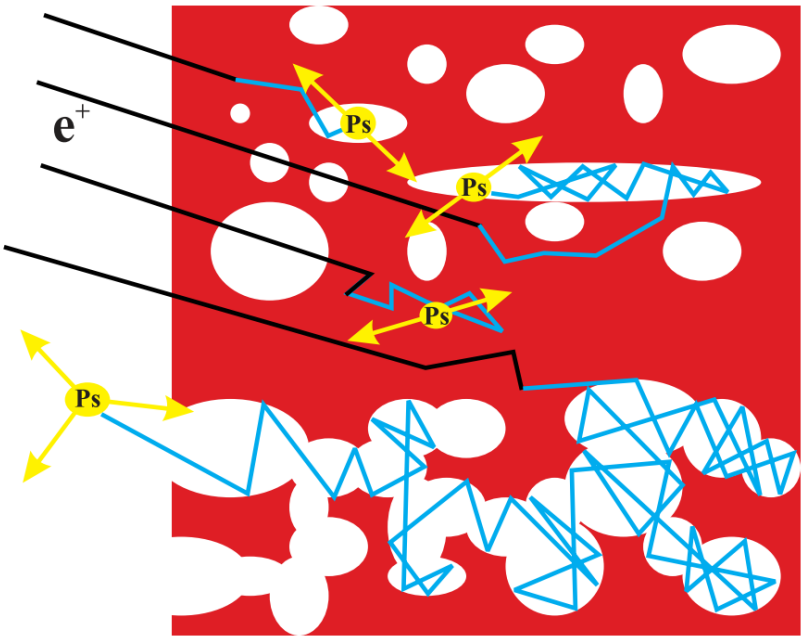

Figure 1.2 A schematic of positronium (Ps) formation in pores.[43] Positrons (e^+) generated from a radioactive source (Specifically, Na^{22} for this dissertation) penetrate pores inside materials and combine with electrons (e^-), forming an unstable state called positronium. the lifetime of Ps is determined by pore size; the larger the pores, the longer the lifetime and the smaller the pores, the shorter the lifetime. Reprinted with permission; Copyright 2006 Annu. Rev. Mater. Res.[43]

To this date, no peer-reviewed PALS study on bone samples has been published. However, researchers employed PALS to study porosity in collagen structure. Siles et al. measured Ps lifetime and intensity as a function of increasing unmineralized collagen from bovine tendon in a fully hydrated condition.[47] Akiyama et al. measured Ps lifetime and intensity changes for gelatin as a function of increasing water content to understand how water fills nanoscale pores.[48]

1.5 Principles of atomic force microscopy-infrared spectroscopy (AFM-IR), optical-photothermal infrared spectroscopy (O-PTIR) and their applications for studying bone

1.5.1 Principles of AMF-IR and O-PTIR

To overcome the spatial resolution of conventional FTIR microscopy techniques, instead of detecting how much infrared energy is transmitted through a sample, PTIR measures surface deflection induced by infrared energy absorbed onto a sample surface, detected by either a gold coated AFM tip (AFM-IR) [49,50] or green laser light (O-PTIR) as illustrated in Figure 1.3.[51] The spatial resolution values for both techniques are determined by each detection method. With the gold coated AFM tip having ~50 nm diameter, AFM-IR has a spatial resolution of ~50 nm.[50] Recent data acquired by AFM-IR with a tapping AFM tip demonstrates a spatial resolution around ~10 nm. O-PTIR achieves a sub-micrometer spatial resolution by using green light with an order of magnitude shorter wavelength (~500 nm) compared to mid infrared light (~20 μm). Zhang et al. determined a spatial resolution of O-PTIR around ~600 nm.[51] The manufacturer provides data showing that O-PTIR can distinguish different chemical signal with ~300 nm spatial resolution.

1.5.2 Applications of AFM-IR for studying bone

Even though AFM-IR has been utilized to study various biomaterials such as bacteria[52], ligament[53], and dentin[54,55], to this date, there are two peer reviewed AFM-IR studies on bone.[56,57] A preliminary study completed by Gourion-Arsiquaud et al. was the first published AFM-IR study on bone and demonstrated the feasibility of obtaining reproducible IR spectra. Also, they compared spectra collected from AFM-IR to spectra from FTIR, demonstrating AFM-IR is capable of capturing key IR peaks such as Amide I and Mineral that are biologically relevant.[56] Imbert et al. validated their experimental method by comparing IR

spectra of a known homogenous material, poly-methylmethacrylate (PMMA) obtained from AFM-IR to IR spectra of the same PMMA from FTIR. Also, their study showed an overall mineralization level increases as tissue ages of cancellous bone samples increase[57], which agrees with a known trend in literature.[58] Since O-PTIR is a relatively new characterization technique introduced to the field, there is no peer reviewed study of O-PTIR on bone.

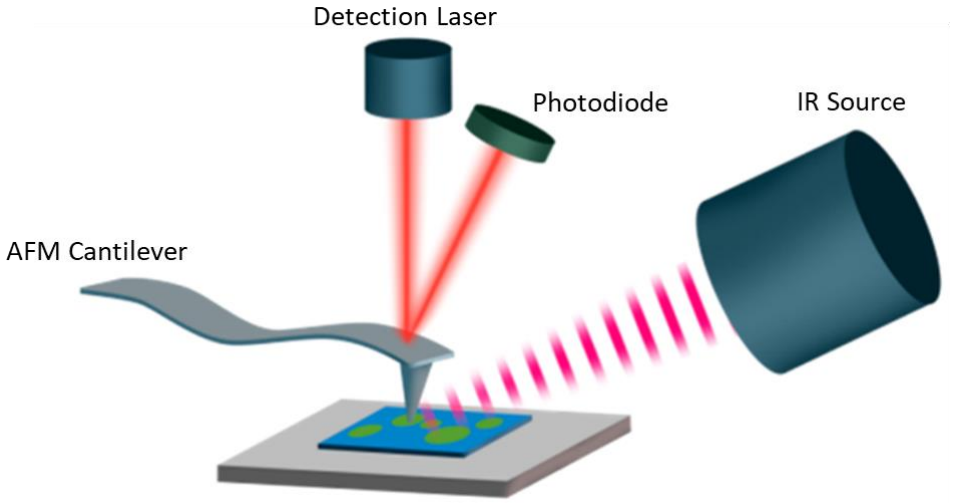

Figure 1.3 A schematic showing basic components of AFM-IR and how AFM-IR detects infrared absorption signal.[50] A gold coated AFM tip (either tapping or contact) measures a level of surface deflection induced by IR source. O-PTIR determines an amount of surface deflection by measuring how much green light is reflected by a surface expansion. For both AFM-IR and O-PTIR, a larger the deflection for a specific wavenumber, a stronger IR signal for that specific wavenumber. Reprinted with permission; Copyright 2017 American Chemical Society.[50]

1.6 Summary and outlook

Bone has been known to have nanoscale mechanical heterogeneity, which is proposed to enhance bone toughening. However, the underlying reasons for the nanoscale mechanical heterogeneity are unknown. Nanoscale bone structure and chemical composition are hypothesized to contribute to the nanoscale mechanical properties of bone.

The nanoscale characterization of the collagen and mineral components in bone have been extensively studied by various material characterization techniques such as TEM, XRD and AFM. However, the nanoscale porosity has been poorly understood due a lack of an appropriate technique that can probe pores in that fine scale. For the first time, we employed PALS with the probe range of ~0.3 to 30 nm to demonstrate the feasibility of using PALS as a powerful experimental technique providing the nanoscale porosity information of bone. Unlike the structural aspect of bone, studying chemical composition in a nanoscale has been relatively limited because of the spatial resolution (~10 μm) of the conventional FTIR technique. Also, bone samples have been chemically dehydrated to detect IR signal. In this dissertation, two newly developed PTIR techniques (AFM-IR and O-PTIR) are applied to capture the nanoscale chemical compositional changes from fully hydrated mouse femoral bone as a function of different tissue ages and genotypes.

In the following chapters, the readers will find how the nanoscale porosity and chemical composition data compare to data from known characterization techniques (nitrogen porosimetry and Raman spectroscopy respectively). Additionally, the readers will see new porosity and chemical composition results obtained by PALS, AFM-IR and O-PTIR providing new information that previously existing techniques could not reveal.

In **Chapter 2**, we report a nanoscale hierarchical nature of porosity in bone, similar to the collagen and mineral construction. We present four distinct pore sizes in dehydrated bone; ~0.5, ~1, ~2 and ~ 4 nm. We compare our experimentally determined pore sizes to simulation results, suggesting the origin of each pore size in the bone structure. We show the existence of ~5 nm plate spacing among mineral plates. This result reveals that the empty space surrounding the

mineral plates is interconnected, suggesting that the nanoscale mineral structure is interconnected as well.

In **Chapter 3**, we report the overall trend of Amide I/mineral ratio values from AFM-IR agrees with our Raman data of Amide I/mineral ratio values on the sample and similar data collection locations (similar tissue ages) between two spectroscopy techniques and the known mineralization trend in literature. However, with an order of magnitude smaller spatial resolution of AFM-IR, we present bone has chemical heterogeneity of Amide I/mineral ratio values where only single spectrum can be obtained by the conventional FTIR. With IR ratio maps, we show that the domain size of our nanoscale chemical maps has a similar length scale of nanoscale mechanical maps obtained by Tai et al.[22] Amide I/mineral ratio values from O-PTIR for wild type samples exhibit the IR ratio changes observed in location to location and animal to animal variations.

These hierarchical nature of nanoscale pores in **Chapter 2** and the nanoscale Amide I/mineral domain size range in **Chapter 3** could contribute to the nanoscale mechanical heterogeneity in bone. Also, the nanoscale pore sizes corresponding to specific bone structures by PALS and the domain size range by AFM-IR from healthy bones could be compared to aging and diseased bones to understand how bone aging and diseases induce nanoscale structural and chemical changes.

1.7 References

[1] H.P. Schwarcz, D. Abueidda, I. Jasiuk, The ultrastructure of bone and its relevance to mechanical properties, Front. Phys. 5 (2017) 1–13.

[2] N. Reznikov, M. Bilton, L. Lari, M.M. Stevens, R. Kröger, Fractal-like hierarchical organization of bone begins at the nanoscale, Science. 360 (2018) eaao2189.

[3] A. Gautieri, S. Vesentini, A. Redaelli, M.J. Buehler, Hierarchical structure and nanomechanics of collagen microfibrils from the atomistic scale up, Nano Lett. 11 (2011) 757–766.

[4] N. Reznikov, R. Shahar, S. Weiner, Bone hierarchical structure in three dimensions, Acta Biomater. 10 (2014) 3815–3826.

[5] S. Weiner, H.D. Wagner, The Material Bone: Structure-Mechanical Functions Relations, Annu. Rev. Mater. Sci. 28 (1998) 271–278.

[6] P. Fratzl, H.S. Gupta, E.P. Paschalis, P. Roschger, Structure and mechanical quality of the collagen–mineral nano-composite in bone, J. Mater. Chem. 14 (2004) 2115–2123.

[7] J.Y. Rho, L. Kuhn-Spearing, P. Zioupos, Mechanical properties and the hierarchical structure of bone, Med. Eng. Phys. 20 (1998) 92–102.

[8] P. Fratzl, Collagen: Structure and Mechanics, Springer, New York, 2008.

[9] K.E. Kadler, D.F. Holmes, J.A. Trotter, J.A. Chapman, Collagen fibril formation, Biochem. J. 11 (1996) 1–11.

[10] E.G. Canty, Procollagen trafficking, processing and fibrillogenesis, J. Cell Sci. 118 (2005) 1341–1353.

[11] J.A. Petruska, A.J. Hodge, A subunit model for the tropocollagen macromolecule, Biochemistry. 51 (1964) 871–876.

[12] J.P.R.O. Orgel, T.C. Irving, A. Miller, T.J. Wess, Microfibrillar structure of type I collagen in situ, Proc. Natl. Acad. Sci. 103 (2006) 9001–9005.

[13] S.J. Eppell, W. Tong, J. Lawrence Katz, L. Kuhn, M.J. Glimcher, Shape and size of isolated bone mineralites measured using atomic force microscopy, J. Orthop. Res. 19 (2001) 1027–1034.

[14] S. Weiner, P.A. Price, Disaggregation of bone into crystals, Calcif. Tissue Int. 39 (1986) 365–375.

[15] W. Traub, T. Arad, S. Weiner, Growth of mineral crystals in Turkey tendon collagen fibers, Connect. Tissue Res. 28 (1992) 99–111.

[16] N. Fratzl-Zelman, I. Schmidt, P. Roschger, F.H. Glorieux, K. Klaushofer, P. Fratzl, F. Rauch, W. Wagermaier, Mineral particle size in children with osteogenesis imperfecta type I is not increased independently of specific collagen mutations, Bone. 60 (2014) 122–128.

[17] R. a Robinson, M.L. Watson, Collagen-crystal relationships in bone as seen in the electron microscope., Anat. Rec. 114 (1952) 383–409.

[18] S.A. Jackson, A.G. Cartwright, D. Lewis, The morphology of bone mineral crystals, Calcif. Tissue Res. 25 (1978) 217–222.

[19] M.J. Olszta, X. Cheng, S.S. Jee, R. Kumar, Y.Y. Kim, M.J. Kaufman, E.P. Douglas, L.B. Gower, Bone structure and formation: A new perspective, Mater. Sci. Eng. R Reports. 58 (2007) 77–116.

[20] W.J. Landis, Mineral characterization in calcifying tissues: Atomic, molecular and macromolecular perspectives, Connect. Tissue Res. 34 (1996) 239–246.

[21] W.J. Landis, K.J. Hodgens, J. Arena, M.J. Song, B.F. McEwen, Structural relations between collagen and mineral in bone as determined by high voltage electron microscopic tomography, Microsc. Res. Tech. 33 (1996) 192–202.
[22] K. Tai, M. Dao, S. Suresh, A. Palazoglu, C. Ortiz, Nanoscale heterogeneity promotes energy dissipation in bone, Nat. Mater. 6 (2007) 454–462.
[23] P.P. Provenzano, R. Vanderby, Collagen fibril morphology and organization: Implications for force transmission in ligament and tendon, Matrix Biol. 25 (2006) 71–84.
[24] J.A. Chapman, M. Tzaphlidou, K.M. Meek, K.E. Kadler, The collagen fibril-A model system for studying the staining and fixation of a protein, Electron Microsc. Rev. 3 (1990) 143–182.
[25] T. Starborg, N.S. Kalson, Y. Lu, A. Mironov, T.F. Cootes, D.F. Holmes, K.E. Kadler, Using transmission electron microscopy and 3View to determine collagen fibril size and three-dimensional organization, Nat. Protoc. 8 (2013) 1433–1448.
[26] B.D. Quan, E.D. Sone, Cryo-TEM analysis of collagen fibrillar structure, 1st ed., Elsevier Inc., 2013.
[27] J. Chen, T. Ahn, I.D. Colón-Bernal, J. Kim, M.M. Banaszak Holl, The Relationship of Collagen Structural and Compositional Heterogeneity to Tissue Mechanical Properties: A Chemical Perspective, ACS Nano. 11 (2017) 10665–10671.
[28] A. Roschger, W. Wagermaier, S. Gamsjaeger, A. Berzlanovich, G.M. Gruber, R. Weinkamer, P. Roschger, E.P. Paschalis, K. Klaushofer, P. Fratzl, Newly formed and remodeled human bone exhibits differences in the mineralization process, Acta Biomater. (2020).
[29] J.M. Wallace, Q. Chen, M. Fang, B. Erickson, B.G. Orr, M.M. Banaszak Holl, Type I collagen exists as a distribution of nanoscale morphologies in teeth, bones, and tendons, Langmuir. 26 (2010) 7349–7354.
[30] M. Fang, E.L. Goldstein, A.S. Turner, C.M. Les, B.G. Orr, G.J. Fisher, K.B. Welch, E.D. Rothman, M.M. Banaszak Holl, Type I collagen D-spacing in fibril bundles of dermis, tendon, and bone: Bridging between nano- and micro-level tissue hierarchy, ACS Nano. 6 (2012) 9503–9514.
[31] J.M. Wallace, B. Erickson, C.M. Les, B.G. Orr, M.M. Banaszak Holl, Distribution of type I collagen morphologies in bone: Relation to estrogen depletion, Bone. 46 (2010) 1349–1354.
[32] J.M. Wallace, B.G. Orr, J.C. Marini, M.M.B. Holl, Nanoscale morphology of Type I collagen is altered in the Brtl mouse model of Osteogenesis Imperfecta, J. Struct. Biol. 173 (2011) 146–152.
[33] Jenifer Jowsey, Studies of Haversian systems in man and some animals, J. Anat. 100 (1966) 857–864.
[34] R. Gauthier, M. Langer, H. Follet, C. Olivier, P.J. Gouttenoire, L. Helfen, F. Rongiéras, D. Mitton, F. Peyrin, 3D micro structural analysis of human cortical bone in paired femoral diaphysis, femoral neck and radial diaphysis, J. Struct. Biol. 204 (2018) 182–190.
[35] Y. Bala, E. Lefèvre, J.P. Roux, C. Baron, P. Lasaygues, M. Pithioux, V. Kaftandjian, H. Follet, Pore network microarchitecture influences human cortical bone elasticity during growth and aging, J. Mech. Behav. Biomed. Mater. 63 (2016) 164–173.
[36] C. de C.A. Lopes, P.H.J.O. Limirio, V.R. Novais, P. Dechichi, Fourier transform infrared spectroscopy (FTIR) application chemical characterization of enamel, dentin and bone, Appl. Spectrosc. Rev. 53 (2018) 747–769.

[37] E.P. Paschalis, R. Mendelsohn, A.L. Boskey, Infrared assessment of bone quality: A review, Clin. Orthop. Relat. Res. 469 (2011) 2170–2178.
[38] A. Boskey, N. Pleshko Camacho, FT-IR imaging of native and tissue-engineered bone and cartilage, Biomaterials. 28 (2007) 2465–2478.
[39] M.D. Morris, G.S. Mandair, Raman assessment of bone quality, Clin. Orthop. Relat. Res. 469 (2011) 2160–2169.
[40] H.B. Hunt, A.M. Torres, P.M. Palomino, E. Marty, R. Saiyed, M. Cohn, J. Jo, S. Warner, G.E. Sroga, K.B. King, J.M. Lane, D. Vashishth, C.J. Hernandez, E. Donnelly, Altered Tissue Composition, Microarchitecture, and Mechanical Performance in Cancellous Bone From Men With Type 2 Diabetes Mellitus, J. Bone Miner. Res. 34 (2019) 1191–1206.
[41] S. Gourion-Arsiquaud, L. Lukashova, J. Power, N. Loveridge, J. Reeve, A.L. Boskey, Fourier transform infrared imaging of femoral neck bone: Reduced heterogeneity of mineral-to-matrix and carbonate-to-phosphate and more variable crystallinity in treatment-naive fracture cases compared with fracture-free controls, J. Bone Miner. Res. 28 (2013) 150–161.
[42] L.M. Miller, R.J. Smith, Synchrotrons versus globars, point-detectors versus focal plane arrays: Selecting the best source and detector for specific infrared microspectroscopy and imaging applications, Vib. Spectrosc. 38 (2005) 237–240.
[43] D.W. Gidley, H.-G. Peng, R.S. Vallery, Positron Annihilation As a Method To Characterize Porous Materials, Annu. Rev. Mater. Res. 36 (2006) 49–79.
[44] P.. Schultz, K.G. Lynn, Interaction of positron beams with surfaces, thin films, and interfaces, Rev. Mod. Phys. 60 (1988) 701–779.
[45] R.A. Pethrick, Positron annihilation - A probe for nanoscale voids and free volume?, Prog. Polym. Sci. 22 (1997) 1–47.
[46] Y.C. Jean, J.D. Van Horn, W.S. Hung, K.R. Lee, Perspective of positron annihilation spectroscopy in polymers, Macromolecules. 46 (2013) 7133–7145.
[47] S. Siles, G. Moya, X.H. Li, J. Kansy, P. Moser, Positron annihilation lifetime measurements in collagen biopolymer, J. Radioanal. Nucl. Chem. 240 (1999) 529–530.
[48] Y. Akiyama, Y. Shibahara, S.-I. Takeda, Y. Izumi, Y. Honda, S. Tagawa, S. Nishijima, Analysis of Swelling Process of Protein by Positron Annihilation Lifetime Spectroscopy and Differential Scanning Calorimetry, J. Polym. Sci. Part B Polym. Phys. 45 (2007) 2031–2037.
[49] A. Dazzi, C.B. Prater, Q. Hu, D.B. Chase, J.F. Rabolt, C. Marcott, AFM-IR: Combining atomic force microscopy and infrared spectroscopy for nanoscale chemical characterization, Appl. Spectrosc. 66 (2012) 1365–1384.
[50] A. Dazzi, C.B. Prater, AFM-IR: Technology and applications in nanoscale infrared spectroscopy and chemical imaging, Chem. Rev. 117 (2017) 5146–5173.
[51] D. Zhang, C. Li, M. Slipchenko, C. Zhang, J.X. Cheng, Depth-resolved mid-infrared photothermal imaging of living cells and organisms at sub-micron resolution, Sci. Adv. 2 (2016) 1–7.
[52] A. Dazzi, R. Prazeres, F. Glotin, J.M. Ortega, M. Al-Sawaftah, M. de Frutos, Chemical mapping of the distribution of viruses into infected bacteria with a photothermal method, Ultramicroscopy. 108 (2008) 635–641.
[53] J. Chen, J. Kim, W. Shao, S.H. Schlecht, S.Y. Baek, A.K. Jones, T. Ahn, J.A. Ashton-Miller, M.M. Banaszak Holl, E.M. Wojtys, An Anterior Cruciate Ligament Failure Mechanism, Am. J. Sports Med. 47 (2019) 2067–2076.

[54] G. Sereda, A. VanLaecken, J.A. Turner, Monitoring demineralization and remineralization of human dentin by characterization of its structure with resonance-enhanced AFM-IR chemical mapping, nanoindentation, and SEM, Dent. Mater. 35 (2019) 617–626.
[55] L. Huang, X. Zhang, J. Shao, Z. Zhou, Y. Chen, X. Hu, Nanoscale chemical and mechanical heterogeneity of human dentin characterized by AFM-IR and bimodal AFM, J. Adv. Res. 22 (2020) 163–171.
[56] S. Gourion-Arsiquaud, C. Marcott, Q. Hu, A.L. Boskey, Studying Variations in Bone Composition at Nano-Scale Resolution: A Preliminary Report, Calcif. Tissue Int. 95 (2014) 413–418.
[57] L. Imbert, S. Gourion-Arsiquaud, E. Villarreal-Ramirez, L. Spevak, H. Taleb, M.C.H. van der Meulen, R. Mendelsohn, A.L. Boskey, Dynamic structure and composition of bone investigated by nanoscale infrared spectroscopy, PLoS One. 13 (2018) 1–15.
[58] P. Roschger, B.M. Misof, Basic Aspects of Bone Mineralization, Springer Nat. (2020) 89–113.

Chapter 2

Hierarchical Nature of Nanoscale Porosity in Bone Revealed by Positron Annihilation Lifetime Spectroscopy

In collaboration with Prof. David W. Gidley*, Dr. Aaron W. Thornton, Dr. Antek G. Wong-Foy, Prof. Bradford G. Orr*, Prof. Kenneth M. Kozloff, Prof. Mark M. Banaszak Holl*

2.1 Abstract

Bone is a hierarchical material primarily composed of collagen, water, and mineral, organized into discrete molecular, nano-, micro-, and macroscale structural components. In contrast to the structural knowledge of the collagen and mineral domains, the nanoscale porosity of bone is poorly understood. In this study, we introduce a well-established pore characterization technique, positron annihilation lifetime spectroscopy (PALS), to probe the nanoscale size and distribution of each component domain by analyzing pore sizes inherent to native bone together with pores generated by successive removal of water and then collagen from samples of cortical bovine femur. Combining the PALS results with simulated pore size distribution (PSD) results from collagen molecule and microfibril structure, we identify pores with diameter of 0.6 nm that suggest porosity within the collagen molecule regardless of the presence of mineral and/or water. We find that water occupies three larger domain size regions with nominal mean diameters of 1.1 nm, 1.9 nm, and 4.0 nm—spaces that are hypothesized to associate with inter-collagen molecular spaces, terminal segments (d-spacing) within collagen microfibrils, and interface spacing between collagen and mineral structure, respectively. Subsequent removal of the collagen determines a structural size pore at 5-6 nm for deproteinized bone—suggesting the average

spacing between mineral plates. A new method to deduce the average mineral spacing from specific surface area (SSA) measurements of the deproteinized sample is presented and compared with the PALS results. Together, the combined PALS and SSA results set a range on the mean mineral plate thickness of 4-8 nm.

2.2 Introduction

Bone is a complex hierarchical nanocomposite consisting of protein fibrils (primarily Type I collagen), mineral plates (carbonated hydroxyapatite), and water.[1–4] The weight fraction range reported for each component is 18-25%, 65-70%, and 10-12%, respectively, and the volume fraction range of each component is 32-44%, 33-43%, and 15-25%, respectively.[5–11] The hierarchical structure of the bone composite from macroscopic to microscopic size scales results in stiffness and toughness properties exceeding those of the individual components.[2] Mechanical heterogeneity related to these multiple length scales present in bone has also been proposed to reduce microcrack formation by contributing to both ductility and energy dissipation.[12–14]

With μ-CT technique, the micro and sub-microstructure of bone (Figure 2.1) such as osteonal and Volkmann canals (50-100 μm) and smaller lacuna-canalicular network spaces (100-200 nm) have been well studied.[15–17] The ultra and nanostructure of bone (Figure 2.1) has been characterized by a number of techniques including scanning electron microscope (SEM),[18] transmission electron microscope (TEM),[19] X-ray diffraction (XRD),[20] and atomic force microscope (AFM).[21] Based on a variety of experimental physico-chemical data including XRD and SEM, Petruska and Hodge proposed an average two dimensional structure of staggered collagen molecules in bone with a regular 67 nm repeating unit.[22] Based on a more detailed XRD study, Orgel et al. developed a fully three-dimensional average packing model

illustrating how collagen molecules pack to form microfibrils.[23] Before Orgel and his colleagues' work on the three dimensional packing of the collagen structure, the widely accepted model of the mineralized fibril in bone contained staggered collagen molecules uniaxially aligned with mineral plates located between collagen microfibrils.[2,24,25] However, the physical dimensions reported for the mineral plates assuming this simple model (length = 15-50 nm; width = 2-30 nm, and thickness = 0.6-10 nm) exhibit wide variation that has been attributed to a number of possible factors including differences in animal species, tissue locations, sample preparation,[5] as well as the variation in sensitivity/resolution of the characterization techniques themselves (AFM,[26] TEM,[27,28] and XRD[20,29,30]). Moreover, recent high-resolution 3D scanning transmission electron microscopy (STEM) tomography studies by Reznikov et al.

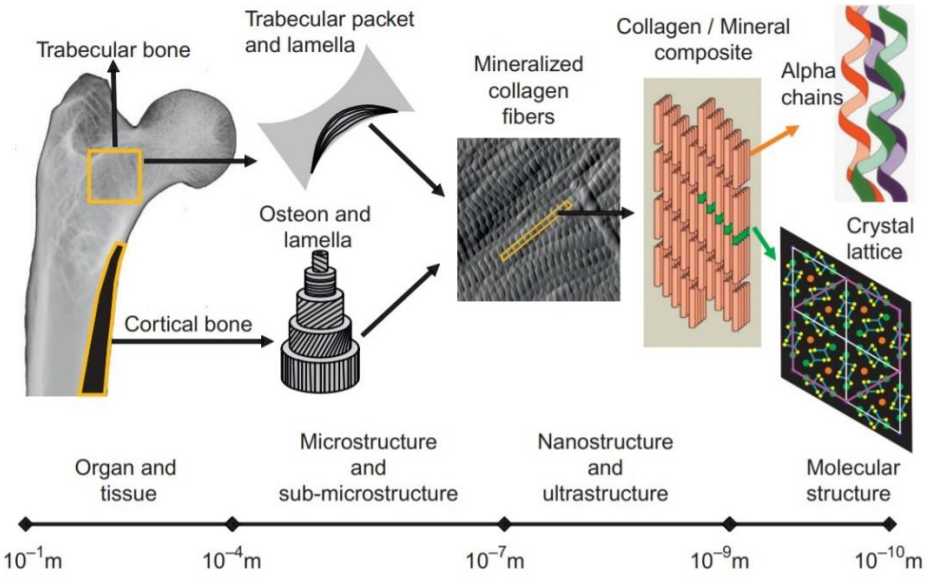

Figure 2.1 A schematic showing a hierarchical nature of the bone structure from macro to molecular level.[31] This study probes the nanostructure, ultrastructure and molecular structure of bone by utilizing positron annihilation lifetime spectroscopy (PALS). Reprinted with permission; Copyright 2014 Elsevier.[31]

indicate the presence of a complex nanoscale hierarchical mineral-collagen structure that gives rise to larger 100 nm stacked clusters of irregular shaped platelets (formed by combining long acicular crystals ~ 5 nm across) and a continuous cross-fibrillar collagen structure.[32] While this model features an interesting intra- and inter-network of mineral structure within the collagen microfibrils, the small acicular crystal building block proposed for mineral structure seems not to be quantitatively consistent with specific surface measurements (to be discussed).

The overall lack of a quantitative consensus on the three-component nanocomposite structure of bone prompted us to consider a technique, positron annihilation lifetime spectroscopy (PALS)[33], with proven sensitivity to *voids/pores* at the nanometer and sub-nanometer scale. Open (empty) pores play a crucial enabling role in this study. In addition to measurements on native bone structure, dehydration allows measurement of voids templated by the water-filled pores, and deproteinization reveals the open space between mineral plates. In this paper, we present the hierarchy in pore size of native voids, water-filled pores, and average mineral spacing in bovine cortical bone as revealed by PALS. For comparison with these results, we also present a new method to combine traditional measurements of specific surface area (SSA) of deproteinized bone mineral with a simple measurement of the corresponding porosity (ratio of void volume to total volume) to independently determine the average mineral plate spacing. Furthermore, our deduced plate spacing range, when limited by the measured porosity and the reported lateral size ranges of the plates, sets a narrower range on mineral plate thickness than previously published.

2.2.1 Positron annihilation lifetime spectroscopy (PALS) for porosity characterization

Unlike the material characterization techniques employed to date to characterize bone, such as SEM, TEM, XRD, AFM, and SSA, whose signal intensity derives from the physical presence of solid material, PALS utilizes positronium (Ps, the hydrogen-like bound state of an electron and its *antiparticle*, the positron) to detect and probe the *absence* of material (i.e. voids or pores). Ps is naturally formed by electron capture when positrons from a radioactive β^+-decay source stop in a porous material and the Ps so formed is energetically driven to localize in the open volume pores. The positron in Ps will annihilate with either its bound electron or with electrons in the material surrounding the pore, and it is this latter process that becomes increasingly dominant at the nanometer pore size. As a result, the average Ps annihilation lifetime measured in PALS can be directly related to pore size. The sensitivity range of PALS to pore size is ~0.3 nm to 30 nm.[33] The method has been employed to measure size and distribution of open void volumes in many materials including polymer composites,[34] unmineralized collagen, and denatured collagen in the form of gelatin.[35,36] PALS has been cross checked with other porosity measurement techniques such as ellipsometric porosimetry (EP), nitrogen gas adsorption, and small angle neutron scattering (SANS).[33,37] Despite its widespread and well documented application in probing voids in hard and soft materials for some 50 years, PALS has not been previously used to systematically study bone nanocomposite. PALS pore data complements the data from XRD, TEM, AFM, and SSA to present a fuller picture of nanoscale structure (collagen, mineral, and water) of bone.

2.3 Materials and Methods

2.3.1 Bovine femur and collagen powder

The bovine femur from a 12 to 18-month-old male was purchased from a local butcher in Ann Arbor, Michigan, USA. Collagen powder derived from bovine Achilles tendon (Sigma-Aldrich, St. Louis, Missouri, USA) was employed in the study.

2.3.2 Rat tail tendon

Tendon was collected from two male and two female rats (total 4 wild type rats) (strain: 403 – SAS FISCH). The rats were 12 to 17 weeks old. The tails were stored frozen in PBS solution in -20 °C freezer and thawed in room temperature. The skin of each tail was manually removed and ~1 mm tendon portion was isolated from fat and soft tissue with a surgical knife. The isolated tail tendons were stored in PBS solution until the PALS measurement.

2.3.3 Bone processing for PALS

The bovine femur was initially frozen at -20°C. When ready for processing, the sample was placed in a plastic bag in a room temperature water tub until it reached room temperature. Once the bovine femur was fully thawed, residual fatty tissue on the surface of the bone and marrow were manually removed and rinsed with tap water. The midshaft region of the bovine femur was perpendicularly cut into ~3.5 mm thick torus-shaped pieces using a pathology saw (Model 312; Exakt Technologies, Oklahoma City, Oklahoma, USA). A torus-shaped piece was further cut into 1-3.5 mm thickness and 15 mm by 10 mm rectangular shaped pieces using a low speed rotary saw (IsoMet; Buehler, Lake Bluff, Illinois, USA) to fit onto the PALS source and sample holder. The final cut pieces were rinsed with nanopure water, stored in a -20 °C freezer, and thawed as needed for experiments.

2.3.4 Sample treatments

There are four preparations of bone sample employed in this study; native, dehydrated, demineralized, and deproteinized. In this study, a native sample is referred to as the sample that was mechanically processed but not dehydrated and/or chemically treated.

2.3.5 Dehydration

The native bone sample was sonicated in nanopure water for 4 minutes to ensure an initial fully hydrated state. The sample was then heated overnight in a vacuum oven below 100 °C.[38] The mass of native bone before and after dehydration was measured to calculate the mass fraction of water loss.

2.3.6 Demineralization

The native bone sample was placed into a fixation buffer of 0.8% paraformaldehyde (prepared from the powder form, Acros Organics, New Jersey, USA) and 0.2% glutaraldehyde (Sigma-Aldrich, St. Louis, Missouri, USA) for 24 hours.[39] After the crosslinking process, an X-ray image (Faxitron microradiography system; Faxitron, Tucson, Arizona, USA) with the setting of 25 KV, 6 seconds of exposure, and 3X distance of the crosslinked bone was acquired to establish a baseline mineralization level. The crosslinked sample was immersed in a mixture of 20% EDTA solution (Fisher Chemical, New Jersey, USA), 0.2% paraformaldehyde and 0.05% glutaraldehyde[39] on a shaker for over 30 days with solution changes every 3 days.

Full demineralization was confirmed by X-ray image. A micro-CT image (In Vivo Bruker/Skyscan 1176; Bruker, Billerica, Massachusetts, USA) with the setting of 9 μm resolution, 0.5 mm aluminum filter, 2 frame averaging, and 0.3 degree rotation step was independently taken for the demineralized sample, which was verified by the X-ray image, to ensure that the sample was indeed fully demineralized. The fully demineralized sample was

dehydrated in a vacuum oven (80 °C, overnight) before PALS measurement. The mass before and after demineralization and dehydration was measured to calculate the mass fraction of mineralization loss.

2.3.7 Deproteinization

Native bone samples were immersed in 2.6 % 5%, and 8.25% of sodium hypochlorite solution (The Clorox company, Oakland, California, USA) at 37 °C on a temperature controlled shaker[40] for over 30 days to ensure that the full deproteinization was achieved. The solution was changed for every 3 days. For each deproteinization process, the sample was dehydrated in a vacuum oven at 80 °C overnight. The mass before and after deproteinization and dehydration was measured to calculate mass fraction of collagen loss. To test the efficiency of chemical deproteinization, the bovine femur was also thermally deproteinized and the change in mass fractions were compared. The bovine femur was ashed in an oven at 600 °C for 18 hours. As soon as the ashed sample was cool enough to be measured, the mass of bone before and after ashing was measured to calculate the mass fraction of collagen loss.

2.3.8 Bone volume measurement

Bone volume for the native, dehydrated, and deproteinized samples (a single sample moved serially through the treatments) was measured by micro-CT as described above. Values of the bone volume from the micro-CT images from each sample treatment were analyzed by NRecon (Bruker, Billerica, Massachusetts, USA) with the setting of 3 smoothing, 16 ring artifact reduction, 30% beam hardening correction and dynamic data range from 0 to 0.05.

2.3.9 Nitrogen gas porosimetry

Fully deproteinized bovine (mineral only) femur was granulated by pestle and mortar. N_2 adsorption/desorption isotherms were measured at 77 K in the range $1.00 \times 10^{-2} \leq P/P_0 \leq 1.00$ on

a NOVA 4200e instrument by Quantachrome Instruments (Boynton Beach, Florida USA), running version 11.03 of the NovaWin software package. Ultra-high purity N_2 (99.999%) was purchased from Cryogenic Gasses and used as received. BET surface area was calculated using the BET assistant and pore size distributions were calculated using the Non-local Density Functional Theory (NLDFT) N_2 silica adsorption branch kernel at 77 K based on a cylindrical/spherical pore model as implemented in NovaWin 11.03.

2.3.10 PALS experimental schematic

PALS experiments were performed on native, dehydrated, demineralized, and deproteinized bovine femur samples after each treatment was complete. For the collagen powder, as-received, vacuum with no heating (overnight), and heating at 80 °C under vacuum conditions were employed. For the rat tail tendon, no heating under vacuum condition was utilized. For the fluorapatite single crystal, PALS was performed in air with no heat. Each PALS spectrum was acquired for at least two days in order to collect 10^7 - 10^8 annihilation events to ensure reliable spectrum fitting.

2.3.11 PALS experiment

Three different spectrometers were used to collect PALS lifetime spectra: two "bulk" PALS spectrometers using various intensities of radioactive ^{22}Na sources to directly inject high energy beta decay positrons into the 1-3.5 mm thick bone samples; and a beam PALS spectrometer wherein a low energy focused beam of mono-energetic (1-10 keV) positrons are shallowly implanted within 1 μm of a bone sample surface.

Bulk spectrometers each have two gamma detectors: one labelled "start" to detect the 1270 keV gamma from the ^{22}Na nucleus that is emitted simultaneously with the beta decay positron; and one labelled "stop" that detects one of the two subsequent 511 keV annihilation

photons. Electronics measure the time between these two gamma rays and a histogram records each detected annihilation event as a lifetime spectrum for eventual computer fitting. The exceedingly wide range in sample porosity encountered from native, hydrated bone (almost none) to deproteinized and dehydrated bone (~ 50%) with attendant positron and positronium lifetimes in a wide range from ~0.2 ns to 140 ns led us to use two complementary bulk spectrometers. One is designed for fast time resolution to make sure all the short lifetime events are properly resolved and fitted while the second has high gamma detection efficiency that permits better fitting of long-lived Ps lifetimes.

The high time resolution spectrometer utilizes small 5 cm diameter plastic scintillators (start scintillator is 5 cm long, stop is 2.5 cm long) coupled to 5 cm diameter fast timing photomultipliers (Amperex XP2020) to allow fitting of the full range of lifetimes encountered in this experiment. These small detectors sacrifice gamma detection efficiency for time resolution and therefore we use stronger ^{22}Na sources in the 10 – 20 μCi range to achieve start-stop coincident event data rates around 100 cps. This spectrometer was used for the collagen powder, the rat tail tendon, the fluorapatite mineral crystal, the native bone, the demineralized bone, and the dehydrated bone where (10 – 60) million events could be collected in a day to a week of acquisition. The stronger positron source results in more random background noise events in the spectrum that makes it more difficult to resolve lower intensity, long-lived events from the random background. To remedy this the high efficiency bulk spectrometer utilizes two large 15 cm cubic plastic scintillators coupled to 13 cm diameter RCA 4582 photomultipliers to achieve an order of magnitude increase in gamma detection efficiency that permits the improvement in signal to background noise by a factor of 10 while concomitantly increasing the data rate to ~700 cps using only a ~1.5 μCi source. This spectrometer was principally used to collect ~ 500 million

events on fully demineralized samples where excellent delineation of Ps lifetimes distributed in the 60 ns -120 ns range is warranted. To this end a CAMAC-based LeCroy 4202 time digitizer of high accuracy and linearity is used for event timing instead of the analog (but fast) time-to-amplitude converter (Ortec 567) used in the fast timing spectrometer. Moreover, for long 10 day runs the sample chamber is back-filled with 20 psi He buffer gas so as not to expose the sample to prolonged oil exposure from the mechanical rough pump. The small effect of Ps annihilating with He was corrected for in the fitting of the spectrum.

The beam PALS spectrometer[33] incorporates a variable energy positron beam to implant positrons a controlled but shallow distance (up to ~ 1 μm) below the surface of a deproteinized sample held in high vacuum. It was used for one specific test to set limits on the ability of Ps to diffuse amongst the mineral crystals of the deproteinized sample.

2.3.12 PALS sample preparation

For bone samples both bulk spectrometers use radioactive positron sources deposited as ^{22}NaCl solution onto a tungsten plate within a designated 0.3 cm x 0.3 cm target area. The solution was deposited until the desired source strength was achieved. To prevent radioactive sample contamination, a 13 μm Kapton (polyimide) film was placed between the deposited radioactive source and the bovine femur (this film stops about 8% of the positrons entering it but does not form any positronium signal). Once the bovine femur was placed onto the Kapton film directly over the source mark, a piece of aluminum foil was wrapped to fixate the sample on the tungsten substrate. The aluminum foiled complex was placed in a flat disc-shaped aluminum vacuum chamber that fits compactly between the gamma detectors of each spectrometer. The collagen powder required a special aluminum cylindrical well 1.6 cm in diameter and 1.3 cm deep. Powder was poured to half fill the well volume, the radioactive source deposited on one

side of a thin 13 μm thick Kapton film was inserted, and the remaining volume above the source was filled with the collagen powder to achieve ~96% stopping of positrons in the collagen. This Al foil wrapped well was then placed in the flat vacuum chamber described above. The irregularly shaped fluorapatite mineral was placed over the tungsten backed source holder described above with a flat crystal plane face presented towards the source (to preclude source positrons from stopping in air). It was wrapped in aluminum foil and run in air in the fast timing spectrometer.

2.3.13 PALS spectrum fitting

Each spectrum collected is a time histogram of "start" – "stop" time intervals in which positron and positronium *lifetimes* are fitted with exponentially decaying lifetimes with intensities fitted as the fraction of all decays that occur with that fitted lifetime. A flat background of uncorrelated events is also present and fitted for. We focus on the positronium (Ps) lifetimes since they are most directly related to the void size from which the Ps decays. We use an updated and customized version of the discrete lifetime fitting program "posfit"[41] to fit for one positron component (lifetime about 0.4 ns and intensity) and any number (typically 2-4) of Ps components (Ps lifetimes in the range 1-140 ns each with corresponding intensities). Given the real possibility of a continuum distribution of Ps lifetimes we also use a modified version of the Laplace inversion fitting program "contin"[42] to fit plausible lifetime distributions. We use well established models of Ps decay in simple pore shapes[43] to make an analytic determination of pore size(s) from the fitted Ps lifetime(s) given an assumed pore shape, either spherical/cubical, cylindrical/channels, or slab shaped/slit pore.

2.3.14 Structures for collagen molecule and microfibril

For the single collagen molecule simulations, the triple-helix structure constructed by Buehler Gautieri et al.[44] based on PDB code 3HR2 was utilized. This relaxed structure included the complete atomic coordinates for all side chains including hydrogen atoms. For the microfibril simulations, the quasi-hexagonal packed structure constructed by Orgel et al.[23] was utilized based on PDB code 3HQV. This rigid structure consists of the backbone C^{α} carbons and highlights the intertwined rope-like configuration of the microfibril.

2.3.15 Pore size distribution

Pore size distribution was calculated using Zeo++ which is a geometrical tool based on the Voronoi decomposition of the void space.[45] Each node and edge of the Voronoi network is deleted if the distance to the nearest atomic surface (defined using the van der Waals radii of each element) is less than the probe radius. The algorithm commences using an infinitely small probe where the entire void space is accessible. The algorithm then repeats this process for increasing probe radius until the void space is inaccessible. The process results in a graph of diminishing void space where the derivative represents the pore size distribution.

2.4 Results

2.4.1 Mass and volume measurements of mineral, protein, and water constituents in bovine femur

Mass (by precision balance) and total volume (by μ-CT) were measured at each stage of processing for native, dehydrated and deproteinized samples. The total sample volume did not significantly change under processing (Table A.1 in Appendix A). Consistent with the literature,[5–10] it was found that water makes up 12 % of the sample bone mass while collagen accounts for 20 % (Table 2.1). For samples dried below 100 °C after the chemical

deproteinization process, the mineral accounts for the remaining 68 % of the bone mass. However, ashing (thermally removing collagen and other organic materials at high temperature) of the bovine femur at 600 °C revealed the mineral mass fraction to be 66 % where an additional 2% water was further removed by high temperature (600 °C). This is also consistent with literature reporting that more tightly bound water is released at elevated temperature (>500 °C).[46] Therefore, the deproteinization from chemical treatment is completed with 2% by mass water remaining in the mineral content of bone. We treat this bound water as occupying no explicit volume fraction except in so far as to add mass and some small volume to the mineral. The relative volume occupied by these component masses can then be estimated using accepted values for the respective densities of water, collagen, and hydroxyapatite as presented in Table 2.1 The porosity, P, of a sample is defined as the fraction of the total volume that is void. After dehydration, we expect P to be 24.3 ± 0.5% (the volume fraction of free water removed as shown in Table 2.1), whereas after deproteinization and dehydration, we expect P to be 55.6 ± 1.0 % (with the error ranges on P determined by how the bound water volume fraction is handled).

Table 2.1 Summary of mass and volume constituents of one gram of hydrated bovine femur.

Constituent	Mass fraction (%)	Density ($g/cm^{3)}$	Mass (g)	Volume (cm^3)	Volume fraction (%)
Free water*	12	1.0	0.12	0.120	24.3
Collagen	20	1.3[47]	0.20	0.154	31.3
Mineral	68	3.1[48]	0.68	0.219	44.4
Total	100	-	1.00	0.493	100

*Free water: water removed under the vacuum condition at 80 °C

2.4.2 Specific surface area (SSA) of deproteinized bovine femur by nitrogen adsorption

The SSA and pore volume distribution were measured with a Quantachrome-NOVA nitrogen adsorption analyser. From a Brunauer-Emmett-Teller (BET) analysis of the adsorption isotherm, the SSA of the deproteinized bone was 118 m^2/g mineral (not per gram of bone). This

is in a good agreement with earlier bovine femur SSA measurements around 100-115 m^2/g using BET.[46,49] However, more recent determinations using cross polarization NMR spectroscopy on mice and chicken bones present higher SSA values in the 137-177 m^2/g range (the mean value of the individual SSA values is 154 ± 15 m^2/g).[50] Utilizing the non-local density functional theory (NLDFT)[51] adsorption model, the pore volume distribution was computed for deproteinized bone (Figure 2.2).

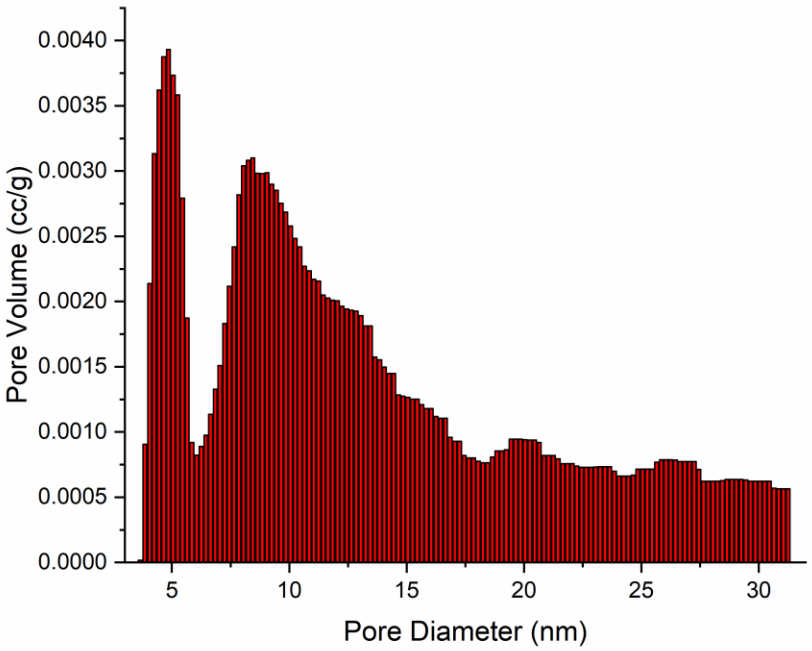

Figure 2.2 NLDFT pore size distribution from nitrogen adsorption data of the deproteinized bovine femur based on a cylindrical/spherical pore model shows a bimodal distribution.

2.4.3 PALS on intact collagen from rat tail tendon, collagen powder from bovine tendon, and demineralized bovine femur

PALS spectra from intact rat tail tendon collagen (vacuum dried without heating) and collagen powder from bovine tendon under the three experimental conditions (as-received in air,

vacuum dried without heating, and vacuum dried at 80 °C) required two Ps (positronium) lifetimes, ~1.4 ns and ~3 ns, for adequate fitting. As shown in Table 2.2, these two lifetimes were converted into corresponding pore sizes based on different assumed pore geometrics. Assuming either a spherical or long cylindrical pore shape yields the diameters D_{sphere} or $D_{cylinder}$. While Ps lifetime reflects pore size, Ps intensity is a measure of the fraction of positrons from the source that annihilate as Ps in each pore, and thus reflect relative amounts of each pore size. Our discrete two-lifetime spectrum fitting does not rule out the possibility that collagen has a *distribution* of Ps lifetimes over the ~1-3 ns range for which two discrete lifetimes adequately account for the breadth of the distribution. Indeed, the intensity-weighted average Ps lifetime for each sample is about 2 ns. Thus, there could be a corresponding distribution in pore sizes in collagen about a mean pore diameter (~0.56 nm for a sphere and 0.45 nm for a cylinder from the Ps lifetime of 2.0 ns). PALS data on the demineralized bovine femur exhibited two lifetimes, 1.28 ± 0.04 ns and 2.70 ± 0.05 ns, which are similar to those of the intact collagen and the collagen powder, suggesting commonly conserved collagen pores across intact, dehydrated, and demineralized sources. It should be noted that substantial shrinkage of 50% or more in total volume accompanied dehydration of the rat tail tendon and the demineralized bovine femur (the collagen powder was already partially air dried as received) indicating that the voids deduced in Table 2.2 are those that survived a more widespread pore collapse. With a support structure of rigid mineral to curtail collapse, we expect to observe much larger pores in dehydrated bone as discussed in the next section.

Table 2.2 Summary of Ps lifetime components and corresponding pore sizes based on different geometries of collagen. Identical values were obtained for as-received material and that vacuum dried at 80 °C. Intensity indicates the percentage of positrons from the source that annihilate as positronium in each lifetime component.

	Intact collagen from rat tail tendon		Collagen powder from bovine tendon		Demineralized bovine femur	
Ps lifetimes	1.48 ± 0.03 ns	3.09 ± 0.06 ns	1.40 ± 0.03 ns	2.90 ± 0.03 ns	1.28 ± 0.04 ns	2.70 ± 0.05 ns
D sphere	0.459 ± 0.007 nm	0.732 ± 0.008 nm	0.440 ± 0.007 nm	0.706 ± 0.004 nm	0.411 ± 0.010 nm	0.678 ± 0.007 nm
D cylinder	0.356 ± 0.006 nm	0.593 ± 0.007 nm	0.340 ± 0.006 nm	0.571 ± 0.004 nm	0.314 ± 0.009 nm	0.546 ± 0.006 nm
Ps intensity	7.1 ± 0.1 %	2.2 ± 0.2 %	7.1 ± 0.1 %	5.9 ± 0.2 %	2.9 %*	1.7 %*

* Absolute Ps intensity should be ignored since the radioactive source was partially dissolved by water leaching out of demineralized collagen during the data acquisition

2.4.4 PALS on native and dehydrated bovine femurs

The cortical portion of bovine femur was chosen for the research material because it provided a large enough volume of bone mass to fully stop the energetic source positrons thereby maximizing the Ps signal while maintaining the ability to process samples into desired shapes. Since the depth of positron penetration of bulk PALS is up to ~ 1 mm, a sample thickness of ≥ 1 mm was chosen. The following experimental tests were chosen with sample identifiers noted (Table 2.3, Figure A.1 in Appendix A). Reproducibility within identical samples and preparation conditions were assessed using sample treatments Dehydrated 1 and Dehydrated 2. To determine whether the heat applied for the dehydration process affected the nanoscale pore structure, Dehydrated 1, Dehydrated 2, and Dehydrated 3 were compared. Impact of source location on Ps intensity and lifetimes was assessed using Dehydrated 4. Sample thickness and chemical treatment effects on Ps intensity were assessed using Deproteinized 1, Deproteinized 2, Deproteinized 3, and Deproteinized 4. For Dehydrated 1 and Deproteinized 3, and Dehydrated 3 and Deproteinized 4, the same bovine femur pieces were serially dehydrated and deproteinized.

PALS fitting of native, hydrated bone spectra shows only a single Ps lifetime value of 2.16 +0.06 ns (Table 2.4). Upon dehydration, the 2.2 ns lifetime component persists along with the appearance of three new lifetime components of 6.5 ns, 21 ns and 56 ns (Figure 2.3, Table 2.4). The pores corresponding to Ps lifetime 2.2 ns showed the highest Ps intensity while the pores emerging following dehydration and corresponding to Ps lifetimes 6.5 ns and 21 ns displayed an equal intensity between them. The pores corresponding to Ps lifetime 56 ns shows the smallest occupation by Ps. Vacuum drying with or without 80 °C heating did not affect the lifetime or intensity values as long as the sample was evacuated under vacuum for at least 24 hours. All but the sub-nanometer voids (~2.2 ns Ps lifetime component) are the result of removing the "free water" (see Table 2.1) to produce a 24.3 % porosity organic-mineral bone nanocomposite.

Table 2.3 Summary of bovine femur samples employed in the paper with the experimental conditions.

Sample name	Sample thickness	Sample geometry	Sample treatment
Dehydrated 1	3.5 mm	Single femur*	Dehydrated overnight at 80 °C under vacuum
Dehydrated 2	3.5 mm	Single femur	Dehydrated overnight at 80 °C under vacuum
Dehydrated 3	3.5 mm	Single femur	Dehydrated overnight under vacuum with no heat
Dehydrated 4	3.5 mm	Two femora **	Dehydrated overnight at 80 °C under vacuum
Deproteinized 1	1 mm	Single femur	8.25 % bleach for over 30 days
Deproteinized 2	1 mm	Single femur	2.6 % bleach for over 30 days
Deproteinized 3	3.5 mm	Singe femur	8.25 % bleach for over 30 days
Deproteinized 4	3.5 mm	Single femur	2.6% bleach for over 30 days
Ashed bovine femur	3.5 mm	Single femur/ Granulated	600 °C for 18 hours, further granulated after an initial PALS measurement on the same intact ashed femur
Demineralized bovine femur	3.5 mm	Single femur	20 % EDTA for over 30 days
Collagen powder	-	Granulated	Dehydrated under vacuum at 80 °C and with no heat
Rat tail tendon	-	Segmented	Dehydrated under vacuum with no heat

* Single femur indicates that one bovine femur covering the radioactive source for PALS measurement
** Two femora indicate that two bovine femur pieces engulfing the radioactive source for PALS measurement

Table 2.4 Summary of Ps lifetime components and corresponding pore sizes based on different geometries from the native and dehydrated bovine femurs (an average of Dehydrated 1-3).

	Ps lifetime in a hydrated/dehydrated state	Ps lifetimes appearing in a dehydrated state		
Ps Lifetime	2.16 ± 0.06 ns	6.5 ± 0.2 ns	21.4 ± 0.7 ns	56.0 ± 1.5 ns
D sphere	0.59 ± 0.01 nm	1.08 ± 0.01 nm	1.92 ± 0.03 nm	4.01 ± 0.14 nm
D cylinder	0.47 ± 0.01 nm	0.90 ± 0.01 nm	1.61 ± 0.03 nm	3.07 ± 0.08 nm
X slab*	0.30 ± 0.01 nm	0.63 ± 0.01 nm	1.2 0± 0.02 nm	2.11 ± 0.05 nm
Ps Intensity	4.9 ± 0.2%	2.3 ± 0.1%	2.2 ± 0.1%	1.5 ± 0.1%

*X slab indicates an empty space between two infinite area slabs

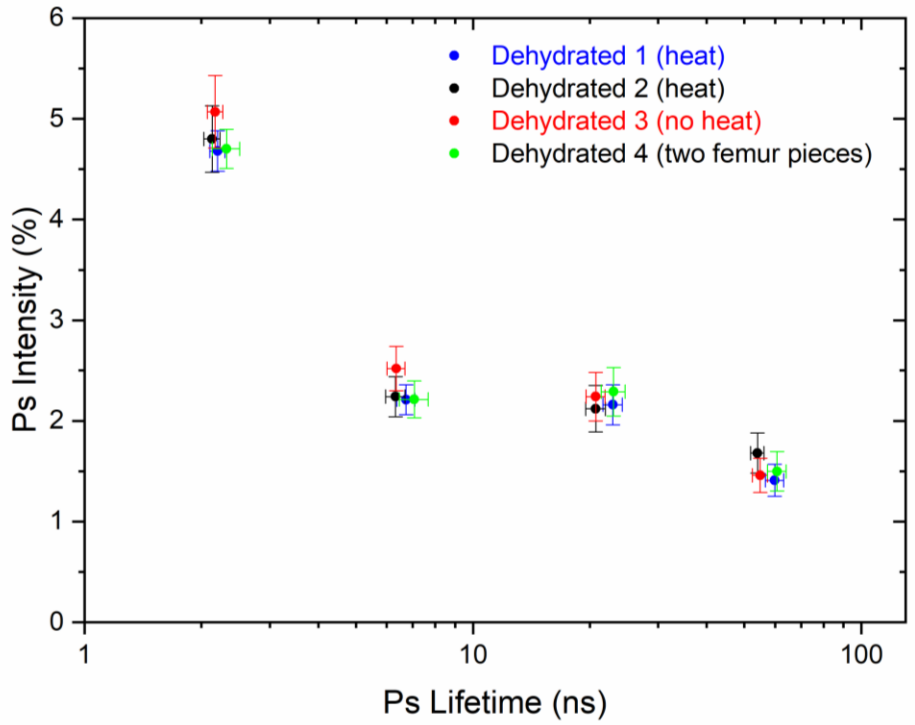

Figure 2.3 The four fitted Ps lifetimes and their corresponding fitted Ps intensities for dehydrated bovine cortical femur bone. Dehydrated 1 and Dehydrated 2 were dehydrated under vacuum with heat. Dehydrated 3 was dehydrated under vacuum with no heat. Dehydrated 4 (two bovine femur pieces surrounding the source) had its fitted intensities reduced by a normalization factor to account for its special source geometry. The four independent sample treatments showed consistent results.

2.4.5 PALS on deproteinized bovine femurs

A variety of deproteinization treatments involving different bleach concentrations, durations, and temperatures up to 50 °C were utilized for bovine bone samples ranging in thickness from 1 - 3.5 mm. It was found that all of the treatments asymptotically converged where the final dried mineral sample weighed 68 % of the native bone mass (Table 2.1). To confirm the complete deproteinization process by bleach, a bovine bone sample was ashed at 600 °C for 18 hours. The ashed bovine sample showed 66 % weighed mass fraction. The 2 % mass fraction differential between the bleached and ashed bovine samples could be explained by the removal of bound water (water that could be only removed by under high temperature). Thus, low temperature bleach deproteinization is complete without the irreversible mineral nanostructure change observed in the PALS results from the ashed bovine sample (see Figure A.2 and Table A.2 in Appendix A).

The PALS spectrum for bleach deproteinized bovine femur is both quantitatively and qualitatively different from the spectra obtained on dehydrated bone. Deproteinization shifted the dominant fitted Ps lifetimes upward into the 75 - 110 ns range (Figure 2.4). All other components, except that of the sub-nm voids, effectively disappeared in these high porosity mineral samples for which the void volume fraction of 55.6% is larger than the mineral volume fraction of 44.4%.

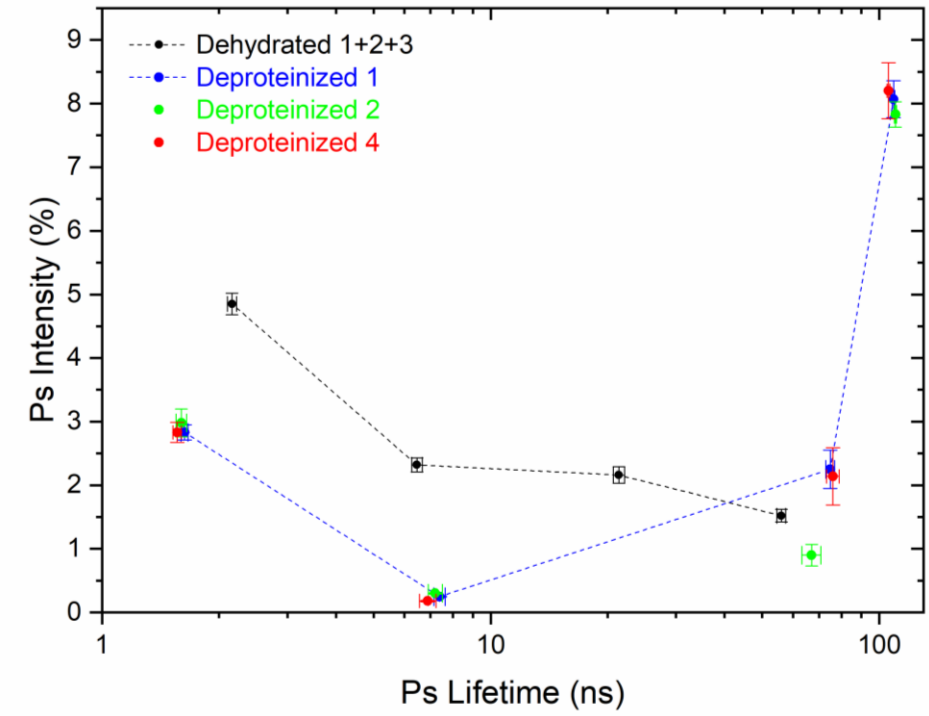

Figure 2.4 PALS discrete lifetime fitting results for Deproteinized 1, 2, and 4 bone samples. Average data for Dehydrated 1, 2, and 3 bone is provided for comparison. Dehydrated 3 and Deproteinized 4 data are from the same bovine femur piece. The black dotted line guides the eye through dehydrated sample data. The blue dotted line connects data from the deproteinized samples.

For such high porosity samples, we expect the voids to be percolated into a continuous open network (conceptually one pore that extends throughout the sample) in which the light and mobile Ps atom probes an average spacing between mineral crystals and results in a single fitted Ps annihilation lifetime. However, the discrete lifetime fitting presented in Figure 2.4 requires *at least* two long lifetimes, suggesting that there is a range or distribution of Ps lifetimes present in the PALS spectrum. This prompted us to use a continuum lifetime fitting program called CONTIN[52] that fits a distribution and determines an average Ps lifetime from that distribution without the bias induced by preselecting the number of Ps lifetimes to be fitted in discrete lifetime fitting.

Ps lifetime spectra from four different deproteinized treatments measured by PALS with the high gamma detection efficiency spectrometer (appropriate for measuring the longer Ps lifetime) were fit with CONTIN, yielding mean Ps lifetimes that ranged from 99.7 ± 0.2 ns to 106.3 ± 0.2 ns (Table 2.5), and a range of lifetime values from ~80 ns to 115 ns. Based on the general consensus of prior literature that bone mineral shapes are plate-like,[2,24,25] we adopted such a model with PALS to determine the average plate spacing between mineral plates X (plates can be parallel, inclined to each other or even gently curved). Because of the breadth of this PALS lifetime distribution, it is technically *not correct* to convert the mean Ps *lifetime* to a plate spacing using the slab geometry pore model. This value is called $X(\tau_{mean})$. Instead, one needs to first convert the CONTIN-fitted number distribution of Ps decays in lifetime τ, dNPs/dτ, to a distribution in X, $dN_{ps/}dX$, and then determine the average in X. To obtain the number distribution of decays in plate spacing X, we need the following:

$$\frac{dN_{Ps}}{dX} = \frac{dN_{Ps}}{d\tau}\frac{d\tau}{dX}$$

Our version of CONTIN has been modified to directly fit the lifetime spectrum into a slab pore geometry to determine the appropriate number distribution in X and hence the correct X_{mean}. A typically fitted distribution in plate spacing X is shown for the Deproteinized 1 sample in Figure 2.5. Overall, X_{mean} is found to be 7-10 % larger than $X(\tau_{mean})$ as shown below in Table 2.5.

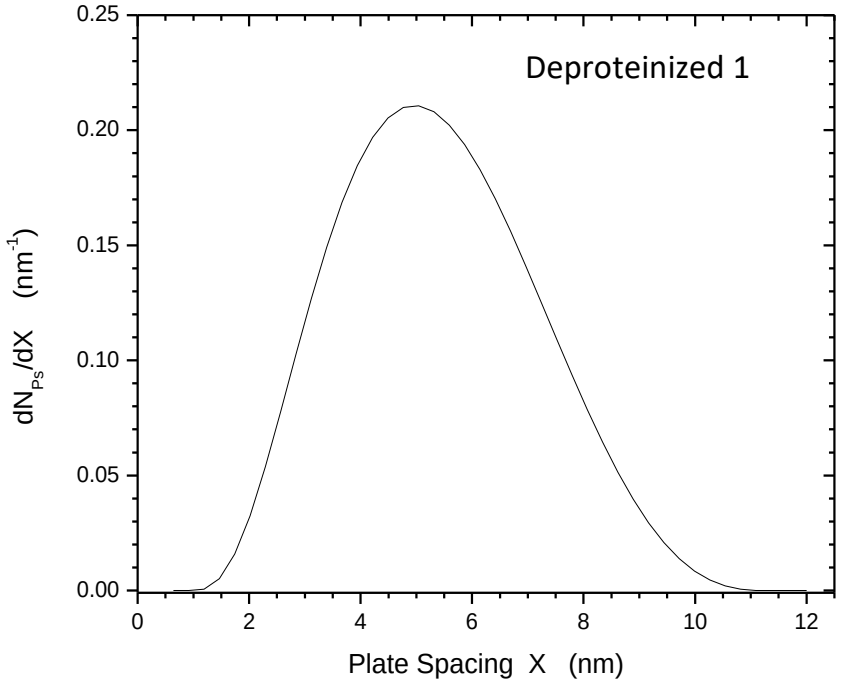

Figure 2.5 A typical distribution in plate spacing X deduced using the continuum fitting program, CONTIN. The area under the curve is normalized to unity. For Deproteinized 1, the average of this distribution is X_{mean} = 5.38 ± 0.03 nm.

Table 2.5 Results of Ps continuum lifetime fitting for four deproteinized treatments. The mean Ps lifetime of the distribution is shown along with the deduced value of $X(\tau_{mean})$ using the infinite plate model. The correctly averaged plate spacing, X_{mean}, is shown in the shaded column.

Deproteinized Sample	Mean lifetime τ_{mean}	$X(\tau_{mean})$	X_{mean} (Plate Spacing)
Deproteinized 1	101.9 ± 0.2 ns	4.88 ± 0.03 nm	5.38 ± 0.03 nm
Deproteinized 2	106.3 ± 0.2 ns	5.52 ± 0.03 nm	6.00 ± 0.03 nm
Deproteinized 3	100.6 ± 0.2 ns	4.72 ± 0.03 nm	5.14 ± 0.025 nm
Deproteinized 4	99.7 ± 0.2 ns	4.61 ± 0.03 nm	4.95 ± 0.02 nm
Deproteinized 4*	100.5 ± 0.2 ns	4.70 ± 0.03 nm	5.02 ± 0.03 nm

*Repeated PALS experiment with the same sample

It is important to note that the fitted total Ps intensity at about 11 % (regardless of discrete lifetime or continuum fitting) was largely unchanged by the removal of collagen to leave just the self-supporting mineral framework. We know from Table 2.2 that pure collagen forms Ps intensity at 13 % but collagen only comprises ~23 % of the dehydrated bone mass (it is mass that

stops positrons and forms Ps). Clearly, the mineral is forming Ps with intensity at ~11%. This is a surprisingly large Ps formation since one observes no Ps formation in *macroscopic* apatite crystals. We acquired a PALS spectrum on a cm-sized single crystal facet of a larger fluorapatite mineral specimen and observed no Ps formation as expected (the pore space between *atoms* in the single crystal is too small for Ps to form). The high Ps formation fraction must be related to the nanometer-sized crystals in native bone. It is well known that positrons in non-defective solids can diffuse up to tens of nanometers before annihilating or encountering a solid surface where positrons can trap in surface states or form Ps that is emitted into the vacuum (there is an extensive body of literature in which low energy (keV) positrons *beams* (see below) are employed to probe Ps formation near surfaces[33]). Bone mineral crystals must therefore be at this small 1-30 nm size scale in order to form Ps at such a high 11% fraction.

2.4.6 Depth-profiled beam-PALS on deproteinized bovine femur

As a test of how well interconnected the space between mineral plates is, a variable energy, 5 mm diameter focused beam of positrons was used to implant positrons at controlled mean distances (from 30 nm to 1 μm) below the surface of a deproteinized sample in high vacuum. This PALS beam technique is much more sensitive to the sample surface compared to bulk PALS where the depth of penetration is ~1 mm. To minimize the damage to this surface from cutting and preparation, it was successively polished with diamond and then alumina paste down to 50 nm grit. All the Ps lifetime spectra acquired at beam energies from 1.2 keV (mean depth 30 nm) to 10 keV (mean depth 1.0 μm) have the same feature in common: copious Ps formation (~15%) and one fitted Ps lifetime ≈ 140 ns corresponding to that of Ps annihilating *in vacuum*. The interpretation is simply that all Ps formed inside the sample up to at least 1 μm deep can readily diffuse between the mineral plates and escape through the sample surface into

the vacuum of the spectrometer. This confirms our suspicion that *deproteinized bovine femur is a fully interconnected void network* in which Ps has the ability to diffuse at least a couple μm (this experiment sets no upper limit).

2.4.7 Simulated pore size distribution (PSD) result of single type I collagen molecule and collagen microfibril

When the single collagen molecule triple-helix structure containing amino acid side chains constructed by Gautieri et al.[44] was analyzed using the Voronoi decomposition of the void space, a nominal spherical pore diameter of around 0.3 nm was identified. These sub-nanometer pores were found within the triple helical structure of the collagen molecule itself, see the portion of the PSD result highlighted as blue in Figure 2.6A and noted as α in Figure 2.6B. Such an intra-molecule PSD would correspond to Ps lifetimes in the range from ~0.8 ns to 3.2 ns based on the spherical model. This Ps lifetime range of ~0.8 ns to 3.2 ns is consistent with the previously published PALS experimental result obtained from collagen in plasma water, showing ~ 2 ns Ps lifetime.[35] When a microfibril containing the carbon backbone of 5 collagen molecules without the presence of the amino acid side chains was constructed based on the coordinates reported by Orgel at al.,[23] two distinct porosity ranges were found as shown in Figure 2.6A. Pores ranging from 0.9 to 1.3 nm (corresponding to 4.5 to 8.9 ns Ps lifetimes based on the spherical model) were found in the region between the collagen molecules (within collagen microfibril), as noted β in Figure 2.6B. In addition, 1.6 to 2.1 nm pores (corresponding to 15 to 25 ns Ps lifetimes based on the spherical model) were found at the terminal segments of the collagen molecules within the collagen microfibril, noted as γ in Figure 2.6B. The same pore range of 1.6 to 2.1 nm (γ) from the PSD result also corresponds to 21 to 35 ns Ps lifetimes based on the cylindrical model, which more closely resembles the elongated pore shape at the terminal

segments of the collagen molecules (Figure A.4 in Appendix A). When the PALS intensity percentage (indicated by three grey circles on each grey dotted line (α, β and γ)) is compared to the simulated porosity percentage from Figure 2.6A, there is a reasonably good agreement between the PALS intensity and the peaks of the simulated PSD.

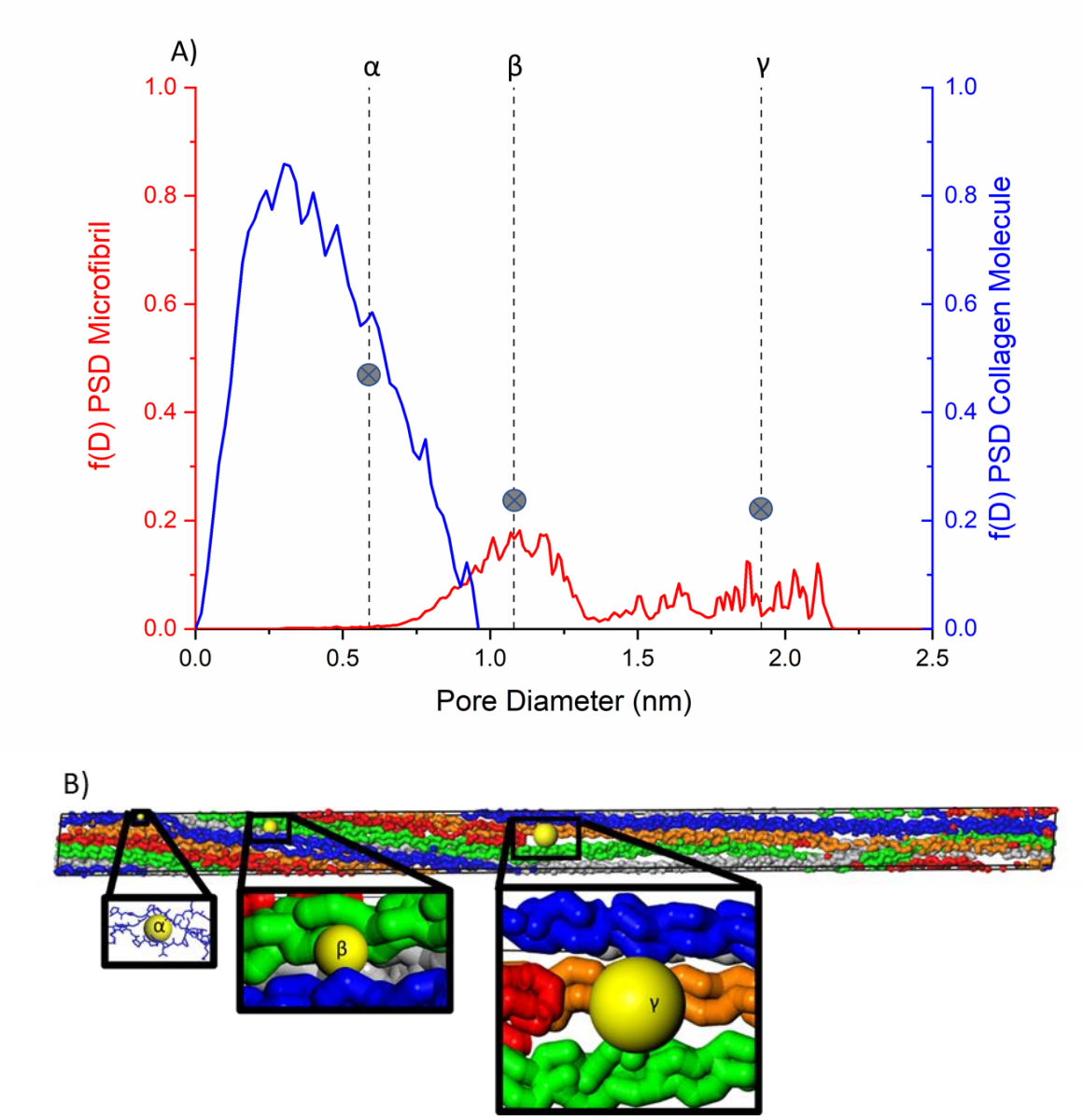

Figure 2.6 A) Calculated pore size distribution (PSD) functions of collagen molecule (blue color) and collagen microfibril (red color) assuming spherical geometry. Three grey dotted lines indicate experimentally determined pore diameter sizes, corresponding to 2.16, 6.5 and 21.4 ns Ps lifetimes, based on the spherical pore shape. Three grey circles on the grey dotted lines indicate experimentally determined Ps intensity values for each lifetime component from Table 2.4. B) Visualization of the collagen microfibril illustrating where three pore sizes are located. α indicates pores within collagen molecules. β indicates pores between collagen molecules. γ indicates pores that are located at the termini of collagen molecules within the collagen microfibril.

2.5 Discussion

2.5.1 Pores within collagen structure without mineral presence

PALS results from the fully dehydrated collagen from intact rat tail tendon and collagen powder from bovine tendon all indicate at least two Ps lifetimes (Table 2.2), suggesting the presence of either a bimodal distribution containing at least two different void sizes or a broad, unimodal distribution of sub-nanometer voids. The collagen from our fully demineralized and dehydrated bovine femur showed PALS results consistent with those of the tail tendon and collagen powder. Such voids at 0.5 nm diameter scale exist in intermolecular regions governed by weak interchain van der Waals forces and are typical of polymeric materials.[37]

When the native, hydrated bovine femur was characterized by PALS, only one Ps lifetime (~2.2 ns), near the average lifetime of the collagen powder, was detected. We know there are larger voids in bovine femur as shown in Table 2.4 and Figure 2.3. However, when they are filled with water, they are not detected as voids. The fitting of a single 2.2 ns Ps lifetime (instead of two Ps lifetimes, 1.4 and 2.9 ns) in hydrated bone indicates that water is partially filling the sub-nanometer voids (narrowing the range of void sizes) and/or that the packing structure of collagen in between the mineral structure (to form a nanocomposite) is now different from that of the pure collagen packing. The simulated PSD result from the collagen molecule with the amino acid side chains (Figure 2.6A) supports the claim that both Ps lifetime components (1.4 and 2.9 ns) from the pure collagen without mineral and the shortest Ps lifetime component (2.2 ns) from the hydrated bone come from intra-collagen molecular spacing.

2.5.2 Spacing between collagen molecules occupied by water

Ps lifetime data of the dehydrated bovine femur shows three additional longer Ps lifetimes after the dehydration process (Table 2.4). The three additional Ps lifetime components

have more total Ps intensity combined than that of the sub-nanometer voids inherent to the collagen (6.0% intensity after dehydration at 80 °C for overnight vs. 4.9% before dehydration). Since the additional lifetimes appeared only after removing water in bone, it is reasonable to conclude that Ps is probing the 24.3% by volume in bone that water used to occupy. The PSD result (noted as β in Figure 2.6A) shows the range of the converted Ps lifetime, from 4.5 to 8.9 ns, based on the identified porosity sizes, which covers the 6.5 ns Ps lifetime. Thus, the 6.5 ns Ps lifetime component from the dehydrated bone is most likely from pores located between adjacent collagen molecules. The PSD result also shows the nominal pore diameter range of 1.6 to 2.1 nm (15 to 25 ns Ps lifetime) found at the terminal segments within collagen microfibril suggesting that the 21 ns Ps lifetime component most likely comes from the termini of collagen molecules within collagen microfibril, associated with the D-spacing commonly observed in EM and AFM images.

Despite its low Ps intensity, the 56 ns component corresponding to void diameters in the 3-4 nm range would be difficult to reconcile with intra-fibril voids. Since the largest identified pores from the collagen microfibril structure is ~2.1 nm, the 56 ns Ps lifetime component could come from inter collagen microfibrils and/or from the interface between the collagen and mineral structure. Constraints on the packing of collagen fibrils imposed by their confinement to the limited space between mineral plates, and their interaction with the surfaces of nanoscale mineral crystals suggest a more rigid collagen packing between mineral plates that results in some unusually large voids. Indeed, the volume vacated by water (24.3 %) is comparable to the volume occupied by the collagen itself (31.3 %) as shown in Table 2.1. Unlike other conventional material characterization techniques such as XRD or TEM, PALS measures signal from empty space, which enabled us to measure the voids created by water removal. The

existence of these four separate Ps lifetimes indicate that four distinct void sizes at the 0.6 nm, 1.1 nm, 1.9 nm and 4.0 nm level exist in the collagen rich region between the mineral crystals. These pores sizes are consistent with the mineral plate spacing since the larger voids that are detected (2.11 to 4.01 nm component) are smaller than a maximum size set by the plate spacing itself of ~5 nm (see Table 2.5). These different-sized voids compete for and trap Ps which leads to different intensities of Ps annihilating in each respective pore size. Also, the porosity comparison between the pure collagen structure without mineral and the dehydrated bone demonstrates the importance of rigid mineral as a structural component. It is the mineral component that allows the dehydrated bone to stabilize the hierarchical porosity structure from 0.63 to 4.01 nm as opposed to the pure collagen structure with just intra-collagen molecule porosity. The next step was to remove the collagen altogether to reveal the full-size scale available for the collagen (and water) packing.

2.5.3 Spacing between mineral plates – a new method for assessing the distance

The deproteinized and dried bovine femur in PALS presented a broad Ps lifetime distribution about a centroid value in the 100-106 ns range. If we assume the mineral crystals are flat plates, this corresponds to average mineral plate spacing in the 5-6 nm range as shown for X_{mean} in Table 2.5. In addition, the specific surface area of one of our deproteinized bovine femur samples was measured by BET analysis to be SSA of 118 m^2/g. SSA, when combined with our determination of the porosity P of the deproteinized bone (55.6 ± 1.0%), our data provides *a completely independent measurement of average mineral plate spacing* as discussed below.

A general measure of the distance an atom or molecule would travel between collisions with the surface of a collection of arbitrarily shaped solid particles (or the distance between

collisions inside a closed pore of any shape) is called the mean free path, MFP. From the kinetic theory of gases the MFP for a gas molecule is

$$MFP = \frac{4V_{void}}{S_{void}}$$

where V_{void} and S_{void} are the volume and surface area of the void (for our sample, one can think of the void as all of the network volume vacated by water and collagen and the surface as that of all the mineral crystals, which is determined by SSA).

Since porosity P is defined as $P = \frac{V_{void}}{(V_{void} + V_{mineral})}$ then $V_{void} = \frac{P}{1-P} V_{mineral}$ and

$$MFP = \frac{4P}{1-P} \frac{V_{mineral}}{S_{void}} \qquad \text{eq. 1}$$

We can equivalently use in the above formula the specific *mineral volume per gram of mineral* (which is $1/\rho_{mineral}$) and the void surface area per gram (which is the SSA) to relate MFP directly to SSA and P as,

$$MFP = \frac{4}{\rho_{mineral}} \frac{P}{(1-P)} \frac{1}{SSA} \qquad \text{eq. 2}$$

This formula is independent of crystal shape, but if we assume for comparison to PALS a large, thin plate model then the plate gap is X = ½MFP. For a mineral density of 3.16 g/cm^3 and P of 55.6 ± 1.0%, we can thus know the ratio P/(1-P) to about ± 4% accuracy. The real limitation might well be the accuracy to which we know the SSA. There is the absolute error (*accuracy*, a systematic error that is mainly relevant in comparing SSA using different techniques) and the statistical error for each measurement (*precision*, which can be determined experimentally by simply rerunning the same sample many times). The error in accuracy appears to be quite large since we have different SSA values from BET (our value at 118 m^2/g agrees well with literature values in the 100-115 m^2/g range[46,49]) compared with SSA from NMR that is 30% higher at 154 m^2/g.[50] Using the equation above, we determine X_{BET} (plate spacing based on SSA by

BET) to be 6.7 nm and X_{NMR} (plate spacing based on SSA by NMR) to be 5.1 nm. This range agrees quite well with the range of X_{mean} from PALS but closer inspection of Table 2.5 indicates that all but the Sample 6 result clearly favour the lower value from X_{NMR}.

Based on these PALS and SSA data, we can show how plate spacing is linearly related to mineral plate thickness. PALS directly probes the porous space between crystals but SSA is related directly to crystal size without regard to porosity once the crystal shape is known. Assuming a rectangular solid with dimensions t (thickness), w (width), and L (length) and with surface area 2(tw+tL+wL) and volume twL, then

$$SSA = \frac{2}{\rho_{mineral}}\left(\frac{1}{t}+\frac{1}{w}+\frac{1}{L}\right) \qquad \text{eq. 3}$$

Substituting this expression for SSA back into equation 2 and continuing to use the plate model where X = ½MFP we find after some rearranging,

$$X = \left(\frac{P}{1-P}\right) t \left(1+\frac{t}{w}+\frac{t}{L}\right)^{-1} \qquad \text{eq. 4}$$

Once we pick a porosity and mineral plate shape such that t/w and t/L are constant then X is linearly related to thickness.

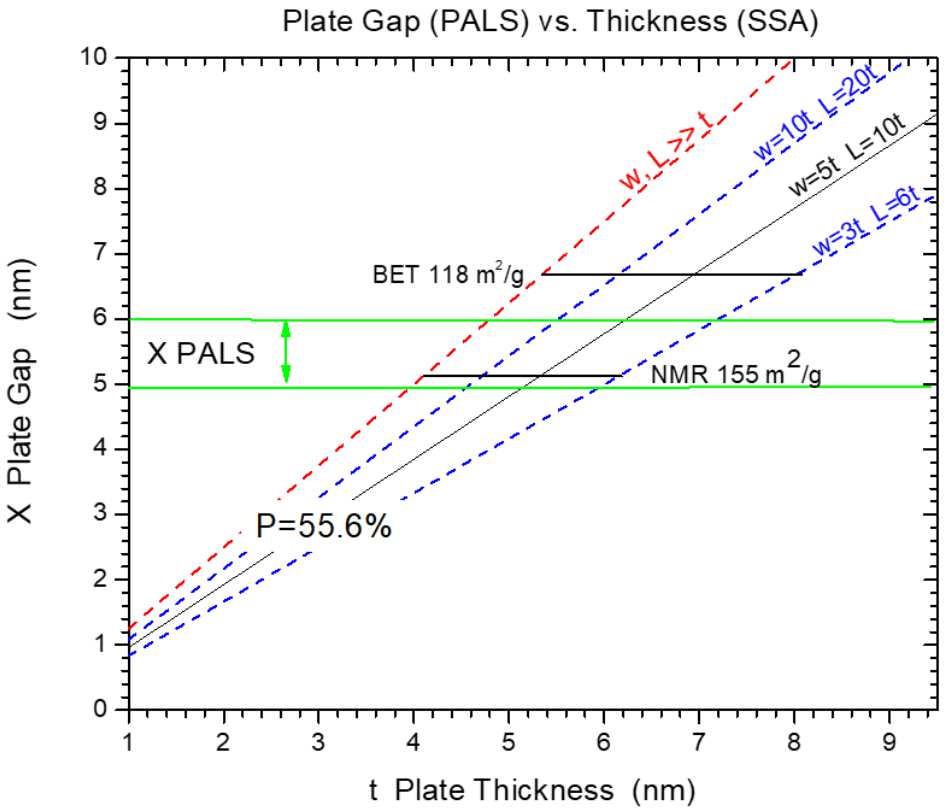

Figure 2.7 Plate spacing X is linearly related to mineral plate thickness t with porosity fixed at 55.6% for four different rectangular shapes of mineral plates. Constraints on the average value of X imposed by results from PALS and SSA from BET and NMR (plus porosity measurement) determine a range in the deduced average mineral plate thickness in native bovine femur. Selected plate sizes for rectangular plates are assumed to have length that is twice the width.

This linear connection between X and t, shown graphically in Figure 2.7, assumes the value of P = 55.6% and for four shapes of mineral plates that vary from infinite width and length to quite small plates with w = 3t and L = 6t. For these examples, we have constrained the length to be twice the width consistent with several reports in the literature, sometimes referred to as the "plywood sheet" model (L~2w).[53,54] A range of thickness values is deduced for each value of SSA. From the NMR result, we deduce a hard-lower limit on t of 4.1 nm when w and L are infinitely larger than t that gets progressively larger to a soft upper limit of t = 6.1 nm as the crystal size approaches (t x 3t x 6t). For the BET result, the range on t is 5.4 nm to 8.0 nm, which

nominally agrees with the mineral plate thickness of ~5-8 nm revealed by electron microscopic techniques.[25,32,55]

2.5.4 Mineral plate geometry based on SSA from mineral structure in bone

The recent article by Reznikov et al.[32] suggests a more complicated arrangement of platelets very close to the size deduced herein (5 nm x 25 nm x 75nm) but then 2-4 of the platelets are stacked together with a gap of only 1-2 nm. If we had solely depended on the PALS data, we could argue that Ps would not really probe the close spacing interior to the putative stacks since any Ps formed at these interior surfaces would quickly diffuse into the inter-*stack* space and not return to probe the narrow 1-2 nm gap spacing. Ps is a quantum mechanical particle and the zero-point energy in such a narrow gap is too high a barrier to surmount once Ps has approached thermalization in the larger spaces. However, the nitrogen adsorption and SSA measurements by NMR should be fully sensitive to both the interior and exterior surface area of the stacks and the comparably large values of deduced plate spacing does not support such small gaps between platelets. Moreover, based on the equations for calculating SSA of the platelet-shaped crystal and the acicular crystallite using specific dimensions for both shapes chosen by Reznikov et al.[32], the SSAs are 158 m^2/g and 290 m^2/g respectively (SSA is conventionally measured as per gram of mineral). In reference 32, equations 1-3 contain an extra multiplicative factor of 0.32 which appears to be related to the fact that mineral is 32% of a whole body skeletal mass,[56] indicating the SSA per gram of skeleton rather than per gram of mineral. The calculated SSA of the platelet-shaped crystal of 158 m^2/g is closer to our measured SSA value of 118 m^2/g and previously reported values of 100-115 m^2/g and 154 ± 15 m^2/g measured by nitrogen adsorption and NMR respectively. These results do not support the conclusion in

reference 32 that the acicular mineral crystal shape is favoured over that of the platelet (see also reference 46 and 49).

2.5.5 Interconnected nature of space surrounding mineral structure in bone

The results of PALS depth-profiling below the surface of deproteinized bone indicate that the voids surrounding the mineral plates are an interconnected network. If Ps is *delocalized* in a sample-wide porous network (as opposed to *localized* in voids of various sizes which produce 4 distinct Ps lifetimes in the dehydrated collagen-mineral nanocomposite), we would expect to fit a *single* average Ps lifetime with no distribution. The premise is that every Ps atom samples the same average environment in a network and hence has the same average lifetime/void size. The observed distribution in Figure 2.5 is inconsistent with this premise. To resolve this inconsistency, we conclude that there must be some natural variation in average network plate spacing due to a variation in mineral plate size, mineral/collagen ratio, and/or porosity on a size scale that is larger than that probed by a *single* Ps atom (hence the ensemble of Ps atoms presents a distribution of lifetimes). A Ps atom can only probe the sample environment within ~one diffusion length. We know from the depth-profiling that Ps is able to diffuse at least 1-2 μm as discussed in the Results section. A better estimate of a lower limit can be made, assuming Ps thermalizes in the sample and then diffuses unimpeded for a lifetime of ~100 ns with an MFP ~ 10 nm. This Ps thermal diffusion length is estimated to be ~ 5 μm (see Appendix A). This diffusion length is *long* enough to be consistent with virtually all Ps escaping into vacuum when implanted only 1-2 μm deep with the positron beam. Concomitantly, the Ps sampling sphere it defines with 10 μm diameter is also *small* enough to assure that our positron source implants positrons into and forms Ps over a probe volume of the sample that is 10^5-10^6 times larger than the volume sampled by a single Ps atom (the source is ~2 mm in diameter with typical

implantation depth of ^{22}Na positrons of ~200 μm). This suggests that the mineral spacing must have some natural variation at a size scale that is larger than 10 μm and much smaller than the 2 mm size of the radioactive source since all of our PALS spectra of the deproteinized mineral present a broad pore size distribution.

2.5.6 Study limitations and future directions

A central conclusion from this study is that the PALS technique has the sensitivity to resolve a detailed hierarchy in size scale present in the collagen-water-mineral nanostructure of bone. In future work, PALS could be sensitive in detecting differences between bone nanostructure due to such effects as aging or genotype, etc. For instance, Fratzl-Zelman et al. revealed that bone samples from patients with osteogenesis imperfecta (OI) type VI have thinner nanoscale mineral crystals, compared to the control population.[57] Combining this information of nanoscale structural change induced by aging or genetic mutations with the porosity change obtained by PALS, it may be possible to understand how these types of genetic changes affect the nanostructure of bone.

The mean lifetime for Ps annihilating in the evacuated space between the mineral crystals can be measured to high and reproducible precision of ± 0.2%. This precision in the Ps lifetime would result in a ±0.6% statistical precision in the deduced MFP once a pore shape model is selected. However, the systematic uncertainty (or *accuracy*) in the MFP deduced from different pore shape models is an order of magnitude larger and arises from the pore shape model dependence in converting an average Ps lifetime into a pore size and hence into MFP. Nevertheless, precise comparisons of mean plate spacing or pore diameter assuming the identical pore shape model are feasible at better than the 1% statistical level. To be cautious, sub 1% comparisons in pore size/mineral spacing may be difficult to realize as shown in Table 2.5 where

different samples taken from the same (large) bovine femur present a range in deduced plate spacing, X, that is ±5% of the average for the first four samples and even higher when Deproteinized 2 is included. Roschger et al. recently published a study examining mineral crystal sizes between modelling and remodelling bone regions by employing X-ray scattering. The study shows that depending on different locations, mineral crystals have different thickness. More specifically, mineral crystals from the modelling sites are distinctly larger.[58] This mineral crystal size variation as a function of different locations could result in the mineral plate spacing variation in Table 2.5, which is larger than the 1 % statistical precision of PALS. This suggests that another future study could sensitively probe 3-D position dependence of bone nanostructure at the millimeter scale by tracking the location of each bone sample section.

2.6 Conclusions

This is the first comprehensive PALS study conducted on bone. By *directly* probing the void structure, PALS complements characterization methods that image or probe electron density. It provides a completely independent view of a complicated nanocomposite system where complexity of structure leads to widely varied approximations of the physical dimensions from various characterization methods.

This study reveals the presence of five separate levels in nanocomposite phase size scales. Sub-nanometer voids appear within collagen regardless of the presence of mineral and/or water. Water-templated voids in dehydrated bone are found to occupy three size scales of voids: 1.1 nm, 1.9 nm, and 4 nm. The largest size scale is observed in deproteinized samples as a 5-6 nm mean spacing between mineral plates. The simulated PSD from the collagen molecule and microfibril clearly delineate a corresponding series of pores. The diameter range around 0.6 nm originates from intra-collagen molecular voids (inherent to the triple helix structure). The pores

with mean diameter of 1.1 nm comes from inter-collagen molecular spacing and 1.9 nm comes from spacing created between two ends of collagen molecules. These water-filled pores are located in regions that have been routinely observed to generate the “D-spacing” commonly observed in EM and AFM studies. The pores with mean diameter near 4 nm are most likely from the interfaces between the collagen fibrils as constrained at the upper limit by the mineral plate spacing. After removal of the collagen, the mineral phase is self-supporting which indicates that the putative platelets are interconnected into a rigid network. The high porosity (~55.6%) empty space between the mineral plates is found to be completely interconnected. The distribution of Ps lifetimes in this porous mineral network indicates that there is a natural variation in average plate spacing on a size scale that is not less than 10 μm. The overall average spacing between the mineral plates deduced by PALS, 5-6 nm, is in quantitative agreement with independent measurements using porosity and SSA (from NMR, less so for BET). This suggests that a collagen microfibril consisting of 5 collagen molecules could fit in between two mineral plates. The mineral spacing (~5-6 nm) and mineral thickness (~4-8 nm based on BET and NMR) deduced here with PALS and in concert with the SSA measurements contradicts some reports in the literature[20,26] of rather small crystal sizes well less than 3 nm while agreeing with other reports.[25,32,55]

In summary, native bone is shown to possess an inherent nanoscale porosity associated with collagen molecules/fibrils. Upon dehydration, three additional features associated with water-filled voids are detected. All four of these nanoscale structures, as well as the mineral plate size and spacing, are likely to play an important role in the macroscopic mechanical properties of bone.[12–14]

2.7 Acknowledgment

The authors would like to thank for support by the National Science Foundation (NSF1634680), the National Insitutes of Health for the microCT shared instrumentation support (S10 OD017979) and the National Institute of Arthritis and Musculoskeletal and Skin Diseases for the Michigan Integrative Musculoskeletal Health Core Center (P30 AR069620), the University of Michigan, and Monash University for support of this work. The authors appreciate help from Carol Whitinger for sample sectioning and Chris Stephan for μ-CT imaging.

2.8 References

[1] S. Weiner, H.D. Wagner, The Material Bone: Structure-Mechanical Functions Relations, Annu. Rev. Mater. Sci. 28 (1998) 271–278.

[2] P. Fratzl, H.S. Gupta, E.P. Paschalis, P. Roschger, Structure and mechanical quality of the collagen–mineral nano-composite in bone, J. Mater. Chem. 14 (2004) 2115–2123.

[3] J.Y. Rho, L. Kuhn-Spearing, P. Zioupos, Mechanical properties and the hierarchical structure of bone, Med. Eng. Phys. 20 (1998) 92–102.

[4] H.P. Schwarcz, D. Abueidda, I. Jasiuk, The ultrastructure of bone and its relevance to mechanical properties, Front. Phys. 5 (2017) 1–13.

[5] M.J. Olszta, X. Cheng, S.S. Jee, R. Kumar, Y.Y. Kim, M.J. Kaufman, E.P. Douglas, L.B. Gower, Bone structure and formation: A new perspective, Mater. Sci. Eng. R Reports. 58 (2007) 77–116.

[6] J.E. Eastoe, B. Eastoe, The organic constituents of mammalian compact bone., Biochem. J. 57 (1954) 453–459.

[7] J.D. Currey, Role of collagen and other organics in the mechanical properties of bone, Osteoporos. Int. 14 (2003) 29–36.

[8] L.W. Fisher, J.D. Termine, Noncollagenous proteins influencing the local mechanism of calcification, Miner. Tissue Res. 200 (1985) 362–385.

[9] J.D. Currey, P. Zioupos, D. Peter, A. Casinos, Mechanical properties of nacre and highly mineralized bone, Proc. R. Soc. B Biol. Sci. 268 (2001) 107–111.

[10] S. V. Dorozhkin, M. Epple, Biological and Medical Si
gnificance of Calcium Phosphates, Angew. Chemie - Int. Ed. 41 (2002) 3130–3146.

[11] J.D. Currey, Biomechanics of Mineralized Skeletons, Skelet. Biominer. Patterns, Process. Evol. Trends. 5 (1999) 11–25.

[12] P. Fratzl, Bone fracture: When the cracks begin to show, Nat. Mater. 7 (2008) 610–612.

[13] K. Tai, M. Dao, S. Suresh, A. Palazoglu, C. Ortiz, Nanoscale heterogeneity promotes energy dissipation in bone, Nat. Mater. 6 (2007) 454–462.

[14] J. Chen, T. Ahn, I.D. Colón-Bernal, J. Kim, M.M. Banaszak Holl, The Relationship of Collagen Structural and Compositional Heterogeneity to Tissue Mechanical Properties: A Chemical Perspective, ACS Nano. 11 (2017) 10665–10671.

[15] Jenifer Jowsey, Studies of Haversian systems in man and some animals, J. Anat. 100 (1966) 857–864.

[16] R. Gauthier, M. Langer, H. Follet, C. Olivier, P.J. Gouttenoire, L. Helfen, F. Rongiéras, D. Mitton, F. Peyrin, 3D micro structural analysis of human cortical bone in paired femoral diaphysis, femoral neck and radial diaphysis, J. Struct. Biol. 204 (2018) 182–190.

[17] Y. Bala, E. Lefèvre, J.P. Roux, C. Baron, P. Lasaygues, M. Pithioux, V. Kaftandjian, H. Follet, Pore network microarchitecture influences human cortical bone elasticity during growth and aging, J. Mech. Behav. Biomed. Mater. 63 (2016) 164–173.

[18] P.P. Provenzano, R. Vanderby, Collagen fibril morphology and organization: Implications for force transmission in ligament and tendon, Matrix Biol. 25 (2006) 71–84.

[19] J.A. Chapman, M. Tzaphlidou, K.M. Meek, K.E. Kadler, The collagen fibril-A model system for studying the staining and fixation of a protein, Electron Microsc. Rev. 3 (1990) 143–182.

[20] N. Fratzl-Zelman, I. Schmidt, P. Roschger, F.H. Glorieux, K. Klaushofer, P. Fratzl, F. Rauch, W. Wagermaier, Mineral particle size in children with osteogenesis imperfecta type I is not increased independently of specific collagen mutations, Bone. 60 (2014) 122–128.
[21] M. Fang, E.L. Goldstein, A.S. Turner, C.M. Les, B.G. Orr, G.J. Fisher, K.B. Welch, E.D. Rothman, M.M. Banaszak Holl, Type I collagen D-spacing in fibril bundles of dermis, tendon, and bone: Bridging between nano- and micro-level tissue hierarchy, ACS Nano. 6 (2012) 9503–9514.
[22] J.A. Petruska, A.J. Hodge, A subunit model for the tropocollagen macromolecule, Biochemistry. 51 (1964) 871–876.
[23] J.P.R.O. Orgel, T.C. Irving, A. Miller, T.J. Wess, Microfibrillar structure of type I collagen in situ, Proc. Natl. Acad. Sci. 103 (2006) 9001–9005.
[24] W.J. Landis, Mineral characterization in calcifying tissues: Atomic, molecular and macromolecular perspectives, Connect. Tissue Res. 34 (1996) 239–246.
[25] W.J. Landis, K.J. Hodgens, J. Arena, M.J. Song, B.F. McEwen, Structural relations between collagen and mineral in bone as determined by high voltage electron microscopic tomography, Microsc. Res. Tech. 33 (1996) 192–202.
[26] S.J. Eppell, W. Tong, J. Lawrence Katz, L. Kuhn, M.J. Glimcher, Shape and size of isolated bone mineralites measured using atomic force microscopy, J. Orthop. Res. 19 (2001) 1027–1034.
[27] S. Weiner, P.A. Price, Disaggregation of bone into crystals, Calcif. Tissue Int. 39 (1986) 365–375.
[28] W. Traub, T. Arad, S. Weiner, Growth of mineral crystals in Turkey tendon collagen fibers, Connect. Tissue Res. 28 (1992) 99–111.
[29] R. a Robinson, M.L. Watson, Collagen-crystal relationships in bone as seen in the electron microscope., Anat. Rec. 114 (1952) 383–409.
[30] S.A. Jackson, A.G. Cartwright, D. Lewis, The morphology of bone mineral crystals, Calcif. Tissue Res. 25 (1978) 217–222.
[31] D.B. Burr, O. Akkus, Basic and Applied Bone Biology, Elsevier Inc., 2014.
[32] N. Reznikov, M. Bilton, L. Lari, M.M. Stevens, R. Kröger, Fractal-like hierarchical organization of bone begins at the nanoscale, Science. 360 (2018) eaao2189.
[33] D.W. Gidley, H.-G. Peng, R.S. Vallery, Positron Annihilation As a Method To Characterize Porous Materials, Annu. Rev. Mater. Res. 36 (2006) 49–79.
[34] R.A. Pethrick, Positron annihilation - A probe for nanoscale voids and free volume?, Prog. Polym. Sci. 22 (1997) 1–47.
[35] S. Siles, G. Moya, X.H. Li, J. Kansy, P. Moser, Positron annihilation lifetime measurements in collagen biopolymer, J. Radioanal. Nucl. Chem. 240 (1999) 529–530.
[36] Y. Akiyama, Y. Shibahara, S.-I. Takeda, Y. Izumi, Y. Honda, S. Tagawa, S. Nishijima, Analysis of Swelling Process of Protein by Positron Annihilation Lifetime Spectroscopy and Differential Scanning Calorimetry, J. Polym. Sci. Part B Polym. Phys. 45 (2007) 2031–2037.
[37] Y.C. Jean, J.D. Van Horn, W.S. Hung, K.R. Lee, Perspective of positron annihilation spectroscopy in polymers, Macromolecules. 46 (2013) 7133–7145.
[38] L. Smith, E.M.R. Bigelow, K.J. Jepsen, Systematic evaluation of skeletal mechanical function., Curr. Protoc. Mouse Biol. 3 (2013) 39–67.

[39] B.D. Quan, E.D. Sone, Cryo-TEM analysis of collagen fibrillar structure, 1st ed., Elsevier Inc., 2013.
[40] P.Y. Chen, D. Toroian, P.A. Price, J. McKittrick, Minerals form a continuum phase in mature cancellous bone, Calcif. Tissue Int. 88 (2011) 351–361.
[41] P. Kirkegaard, Positronfit extended: a new version of a program for analyzing positron lifetime spectra, Comput. Phys. Commun. 7 (1974) 401–409.
[42] R.B. Gregory, Y. Zhu, Analysis of positron annihilation lifetime data by numerical laplace inversion with the program CONTIN, Nucl. Inst. Methods Phys. Res. A. 290 (1990) 172–182.
[43] D.W. Gidley, W.E. Frieze, T.L. Dull, J. Sun, A.F. Yee, C. V. Nguyen, D.Y. Yoon, Determination of pore-size distribution in low-dielectric thin films, Appl. Phys. Lett. 76 (2000) 1282–1284.
[44] A. Gautieri, S. Vesentini, A. Redaelli, M.J. Buehler, Hierarchical structure and nanomechanics of collagen microfibrils from the atomistic scale up, Nano Lett. 11 (2011) 757–766.
[45] T.F. Willems, C.H. Rycroft, M. Kazi, J.C. Meza, M. Haranczyk, Algorithms and tools for high-throughput geometry-based analysis of crystalline porous materials, Microporous Mesoporous Mater. 149 (2012) 134–141.
[46] A.S. Posner, R.A. Beebe, The surface chemistry of bone mineral and related calcium phosphates, Semin. Arthritis Rheum. 4 (1975) 267–291.
[47] I.G. Fels, Hydration and density of collagen and gelatin, J. Appl. Polym. Sci. 8 (1964) 1813–1824.
[48] H.M. Rootare, R.G. Craig, Characterization of the compaction and sintering of hydroxyapatite powders by mercury porosimetry, Powder Technol. 9 (1974) 199–211.
[49] J.M. Holmes, D.H. Davies, W.J. Meath, R.A. Beebe, Gas Adsorption and Surface Structure of Bone Mineral, Biochemistry. 3 (1964) 2019–2024.
[50] A.J. Taylor, E. Rendina, B.J. Smith, D.H. Zhou, Analyses of mineral specific surface area and hydroxyl substitution for intact bone, Chem. Phys. Lett. 588 (2013) 124–130.
[51] C. Lastoskie, K.E. Gubbins, N. Quirke, Pore size distribution analysis of microporous carbons: A density functional theory approach, J. Phys. Chem. 97 (1993) 4786–4796.
[52] S.W. Provencher, A constrained regularization method for inverting data represented by linear algebraic or integral equations, Comput. Phys. Commun. 27 (1982) 213–227.
[53] S. Weiner, W. Traub, H.D. Wagner, Lamellar Bone: Structure–Function Relations, J. Struct. Biol. 126 (1999) 241–255.
[54] M. M. Giraud-Guille, Twisted plywood architecture of collagen fibrils in human compact bone osteons, Calcif Tissue Int. 42 (1988) 167–180.
[55] M.A. Rubin, I. Jasiuk, J. Taylor, J. Rubin, T. Ganey, R.P. Apkarian, TEM analysis of the nanostructure of normal and osteoporotic human trabecular bone, Bone. 33 (2003) 270–282.
[56] H.H. Mitchell, T.S. Hamilton, F.R. Steggerda, H.W. Bean, The chemical composition of the adult human body and its bearing on the biochemistry of growth, J. Biol. Chem. 158 (1945) 625–637.
[57] N. Fratzl-zelman, I. Schmidt, P. Roschger, A. Roschger, F.H. Glorieux, K. Klaushofer, W. Wagermaier, F. Rauch, P. Fratzl, Unique micro- and nano-scale mineralization pattern of human osteogenesis imperfecta type VI bone, Bone. 73 (2015) 233–241.

[58] A. Roschger, W. Wagermaier, S. Gamsjaeger, A. Berzlanovich, G.M. Gruber, R. Weinkamer, P. Roschger, E.P. Paschalis, K. Klaushofer, P. Fratzl, Newly formed and remodeled human bone exhibits differences in the mineralization process, Acta Biomater. (2020).

Chapter 3

Atomic Force Microscopy-Infrared Spectroscopy (AFM-IR) and Optical Photothermal Infrared Spectroscopy (O-PTIR) Characterization of Wild Type (WT) Mice Femurs

In collaboration with Max Jueckstock, Dr. Diana Dillstrom, Dr. Gurjit S. Mandair, Dr. James Henderson, Dr. Benjamin P. Sinder, Prof. Kenneth M. Kozloff*, Prof. Mark M. Banaszak Holl*

3.1 Abstract

Nanomechanical heterogeneity in bone has a length scale of ~100 to 500 nm and may play a role in damage evolution and toughening bone. Infrared (IR) and Raman spectroscopy techniques with ~10 μm spatial resolution are unable to resolve chemical information at the length scale of collagen fibrils (~20-250 nm) and mineral plates (~20-40 nm); however, the invention of atomic force microscopy-infrared spectroscopy (AFM-IR) provides ~ 50 nm spatial resolution, making it possible to study the nanoscale chemical heterogeneity in fully hydrated bone. Also, a novel optical photothermal infrared spectroscopy (O-PTIR) allows acquisition of full IR spectra with 1 μm spacing over a larger region of interest that AFM-IR cannot reasonably image in a timely manner. This study is the first to combine AFM-IR and O-PTIR techniques with fluorescently labeled bone samples indicating specific tissue ages. The overall Amide I/mineral ratio values from AFM-IR agree with the ratio trend from Raman spectroscopy; as tissue becomes mature, the mineralization level increases. However, the ratio values from AFM-IR reveal additional chemical information that as tissue becomes mature, the Amide I/mineral ratio variation decreases as well. Domain sizes analysis obtained from the IR ratio maps display a diameter range from ~50 to 500 nm, which agrees with the length scale of nanomechanical heterogeneity. The Amide I/mineral ratio values from O-PTIR reveal significantly different

location to location and animal to animal chemical variations; even though the animals have the same genotype, some animals have significantly higher average Amide I/mineral ratio values than the rest (about 30% ratio value reduction). Some animals have no IR ratio changes as a function of bone age whereas other animals show decreasing average IR ratio values with age.

3.2 Introduction

Bone is a biocomposite material that mainly consists of collagen and mineral and is constructed in a hierarchical fashion from nano to macro-level length scale.[1–6] Bone exhibits the optimized mechanical properties of both components; simultaneously achieving strength and toughness.[7]

Vibrational spectroscopy techniques such as Fourier-transform infrared spectroscopy (FTIR)[8–10] and Raman spectroscopy[11] have been extensively utilized to study chemical composition in bone and other biological tissues such as cartilage, enamel and dentin. The field has primarily focused on three major chemical parameters to assess bone quality change as a function of disease or aging; 1) mineral to matrix ratio; 2) mineral maturity/crystallinity; 3) collagen maturity.[8] For instance, Wang et al. utilized FTIR to study the effects of fracture history and drug treatment on all three chemical parameters. Bone samples without fracture history showed different chemical means and distributions of mineral to matrix ratio, mineral maturity/crystallinity, and collagen maturity than bone samples with a history of fracture and drug treatment.[12] However, due to the spatial resolution (defined by x and y two-dimensional area measured by a technique) limit of conventional FTIR microscopy (~10 μm)[13], examining chemical variation below the lamellae structure (Figure 3.1) has only recently become possible. In this chapter, chemical data from both atomic force microscopy-infrared spectroscopy (AFM-IR) and optical phothermal infararedspectrooscpy (O-PTIR) are shown as Amide I

(matrix)/mineral ratio values. The single wavenumber peak and wavenumber ranges for peak area are selected based on previously published work; Amide I (1694-1625 cm^{-1} [8]) and mineral 1200-900 cm^{-1} [9])

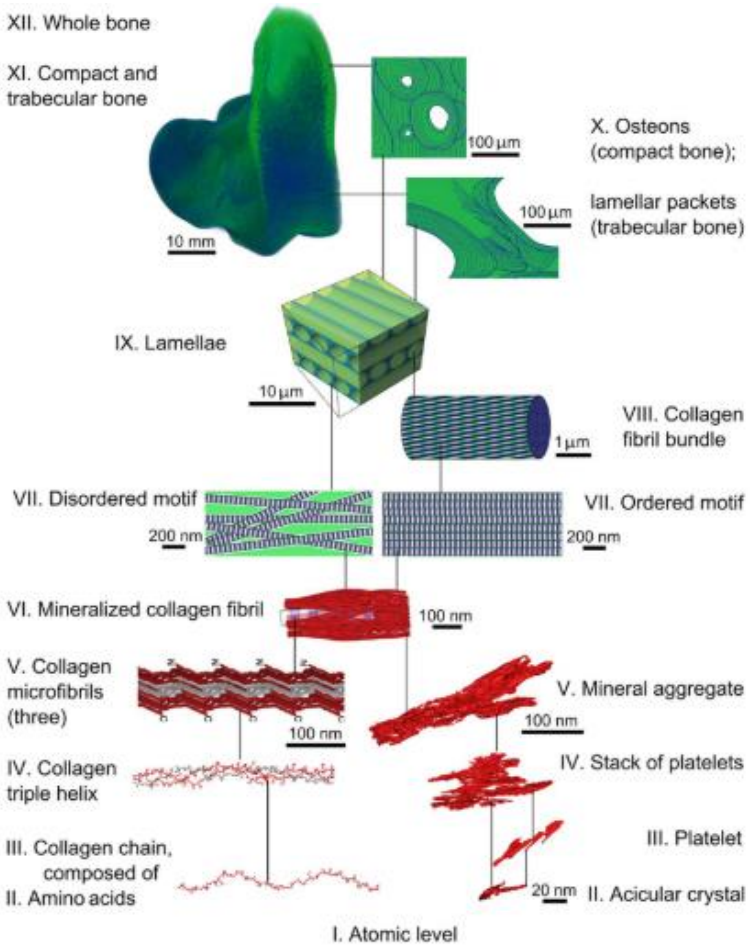

Figure 3.1 Hierarchical arrangement of collagen and mineral components in bone.[3] Most spectroscopic studies investigating chemical compositions to date have sufficient areal resolution (~ 10 µm) to resolve variation at the level of the lamellae or larger features. Investigations measuring chemical compositions at the level of the collagen fibril bundle and below are substantially more limited. Recent advances in atomic force microscopy-infrared (AFM-IR) spectroscopy offer a nominal areal resolution as small as 10 nm. Reprinted with permission; Copyright 2018 Science.[3]

AFM-based nanoindentation studies[14,15] demonstrated bone has nanoscale mechanical heterogeneity with a length scale of one or two collagen fibrils. These studies suggested that having the mechanical heterogeneity at the nanoscale length may enhance energy dissipation in bone and as a result, toughening the bone. There are two potential reasons contributing to the nanoscale mechanical heterogeneity; structure and chemical. AFM[16–18] and TEM[19] studies demonstrated the nanoscale bone structure has been relatively well studied. However, studying the chemical composition of bone at the nanoscale has been limited due to the spatial resolution limit of conventional infrared microscopy until the invention of atomic force microscopy-infrared spectroscopy (AFM-IR) was invented. Also, bone samples probed by conventional infrared microscopy need to be chemically dehydrated to detect IR signal. This sample prepration requirement does not allow researchers to obtain chiemcal information from samples that are more relevant to a physiologcal condition. Raman spectrosocpy, which is not sensitive to water, has been utilized to probe hydrated bone samples.[11] AFM-IR is a novel infrared spectroscopy technique that utilizes an AFM tip as a probing method to achieve a nominal spatial resolution of ~50 nm.[20,21] AFM-IR along with optical phothermal infarared spectrooscpy (O-PTIR)[22] can aquire chemical information on fully hydated bone samples, which is a major advantage of employing AFM-IR and O-PTIR over conventional infrared microscopy. There are a few studies that employed AFM-IR to study biological tissues such as bone[23,24], dentin[25,26] and anterior cruciate ligament.[27] In particular, Imbert et al. validated AFM-IR by comparing both chemical spectra of the same PMMA from AFM-IR and FTIR. Also, they showed the overall increasing mineralization over tissue maturity.[24] In this manuscript, combining our chemical data by AFM-IR with fluorescence images of the same bone samples indicating specific tissue ages, we revealed overall mineralization (more specifically, Amide

I/Mineral ratio values) and a level of chemical variation as a function of specific tissue ages. Also, we obtained IR ratio maps of Amide I/Mineral and quantified different domain sizes from the different Amide I/Mineral ratio value ranges.

3.3 Materials and Methods

3.3.1 Sample preparation

The total nine wild type mice femur samples (five 6-month-old mature and four 2-month-old rapidly growing samples) were originally prepared by Sinder et al.[28] including the fluorescence injection scheme (labelled for day 1, week 1, week 3 and week 5 tissue ages), polymer embedding and sectioning. In addition to their original sample preparation, there were two more steps to prepare the wild type samples for AFM-IR and O-PTIR; 1) since the original samples were too tall for both instruments, the samples were sectioned to about 4 to 5 mm tall by a low speed rotary saw (IsoMet; Buehler, Lake Bluff, Illinois, USA). To capture new fluorescence images for the samples, additional steps with P1200, P2400, P4000 and 3 μm diamond suspension polishing (Buehler, Lake Bluff, Illinois, USA) were applied for 10 seconds per each polishing step. After polishing, the samples were washed with distilled water. To give a point of reference between different spectroscopy techniques, a fiducial mark was cut with a sharp knife onto a bone surface.

3.3.2 Fluorescence imaging

An upright Nikon microscope connected with a DS-Fi2 digital camera (Nikon Eclipse Ni-U, Tokyo, Japan) was employed to take fluorescence images with a 10X dry objective. First, the microscope was set to obtain a calcein image and an alizarin image was taken subsequently. Since the fluorescence signal from the alizarin dye was typically weaker than that of the calcein dye, an exposure time for the alizarin image was adjusted to match the fluorescence signal

intensity of the calcein image. NIS BR software (Nikon, Champigny-sur-Marne, France) was used to combine both calcein and alizarin images with a scale bar.

3.3.3 Individual IR spectra collection by NanoIR 2 and spectral processing

NanoIR 2 (Anasys Instruments, California, USA) was utilized to acquire full IR spectra with 860 to 1900 cm^{-1} wavenumber range with 4 cm^{-1} spectral resolution on one 2-month-old and one 6-month-old mouse femur sample. NanoIR 2 was operated for the contact mode with a contact mode AFM tip (gold coated silicon cantilever, nominal radius 25 nm, force constant 0.07-0.4 N/m, resonance frequency 13±4 kHz). NanoIR 2 was operated with the setting of the laser power as 2.54 % with an OPO laser, center frequency as 189 kHz with 50 kHz of frequency window and band pass filter turned on. Each IR spectrum was averaged over four spectra. For both 2-month-old and 6-month-old samples, each IR spectrum was collected with 1 μm. The locations and length of line spectra were determined by the previously collected fluorescence images.

To process the IR spectra, first of all, each spectrum was smoothed by the Savitzky-Golay filter with the polynomial order as 3 and side points as 5 by Analysis Studio (Anasys Instruments, California, USA). The smoothed spectra were imported to Origin software (version Origin 2009, Northampton, Massachusetts, USA). The baseline of each spectrum was manually corrected by using “Peak Analyzer” function of Origin and the peak areas of Amide I and mineral were calculated by using “Integrate” function of Origin.

3.3.4 Individual Raman spectroscopy

Before obtaining Raman spectra, IR data collection for the 2-month-old mouse femur sample was performed first. Based on the optical image from AFM-IR with the fiducial mark from the sample, the x and y coordinates for the AFM-IR data collection were determined.

Raman microscope used for this experiment was able to precisely move to a specific point by the in-house Matlab software. With the same coordinate information, AFM-IR and Raman data collection for the comparable tissue ages were possible. For each tissue age (Week 1, Week 3 and Week 5), single Raman spectrum was acquired.

Raman microscope was equipped with a 785 nm diode laser (Innovative Photonics Solutions, Monmouth Junction, NJ, USA) and a 25 μm slit which can provide the spectral resolution of 4 cm^{-1}. The exact details of the instrumentation and experimental condition can be found by Shi et al.[29]

3.3.5 Amide I/mineral IR ratio map collection by NanoIR 2 and NanoIR 3

There were two dimensions for the IR ratio images; 1) 10 by 20 μm and 10 by 10 μm. Two wavenumbers (one for Amide I image and another for mineral image) were selected based on individual IR spectra obtained prior to the IR ratio maps. Regardless of 10 by 20 or 10 by 10 μm dimensions, each image was obtained with 300 by 300 points which was predetermined by the OPO laser pulse rate with respect to AFM scanning speed. The experimental parameters were set for the laser power as 2.54 % with an OPO laser, center frequency as 189 kHz with 50 kHz of frequency window and band pass filter turned on with the contact mode and the same AFM tip for the individual IR spectra collection. The scan rate was set as 0.1 Hz. When single wavenumber IR images were collected, AFM height and deflection images were simultaneously obtained. NanoIR 3 (Bruker, Santa Barbra, CA, USA) was operated under the same experimental condition with 10 by 10 μm having 300 by 300 points.

To process the IR ratio maps from two individual singe wavenumber IR images, two height images accompanying two single wavenumber IR images were plane fitted with 1^{st} fit order by Analysis Studio. It is crucial to maintain that the IR images **were not** processed at all

throughout the whole imaging processing. Two single wavenumber images were subsequently ratioed by “Ratio” function under “Calculate Image” tap. The two plane fitted height images were used to correct any thermal drift. Once a ratioed IR ratio image was generated as a csv file, the ratio image could be used by other graphing software to create a figure or further analyzed to calculate domain sizes by Fiji.

Typically, PMMA and bone had a different topography and could be distinguished by AFM maps. However, to ensure the data collection began with the first day of bone, individual IR spectra were collected between PMMA and bone as shown in Figure B.5.

3.3.6 Domain size analysis procedure

Once the Amide I/mineral IR ratio maps were generated and stored as a csv file, the csv file was directly imported to Fiji version of ImageJ by using the function “Text Image” under “Import” tap. Once the image was imported, a scale was set with “Set Scale” function. The imported IR ratio image was thresholded by an incremental 1 ratio range. Each thresholded image was converted to 8-bit binary file and watershed by “Watershed” function under “Binary” tab. The watershed image was used to generate individual diameter sizes for each watershed region by using “Analyze Particles” function. Since the data collection step size was smaller than that of the nominal AFM-IR resolution of ~50 nm (contact mode), the particle analyzing parameter was set up to exclude particle sizes under 50 nm. Each watershed image examples used for generating diameter sizes can be found in Figure B.4.

3.3.7 EDX experimental setup

Before obtaining any EDX data, a 4 mm mouse femur sample was further sectioned to ~ 1 mm thickness with the low speed rotary saw and was coated with a gold layer for SME imaging. Similar to obtaining Raman spectra, the IR ratio map by AFM-IR was collected first to

provide coordinates for the EDX experiment. A scanning electron microscope equipped with EDX capability (BSEM, Tescan MIRA3 FEG- SEM, Czech) was operated under at 15 kV accelerating voltage, 141 pA current, 197.82 μm depth of focus, 366X magnifications, and 10 beam intensity. Ca and P concentration was measured for the nominally similar region where AFM-IR data was taken.

3.3.8 Hyperspectral data collection by O-PTIR and hyperspectral data processing by Cytospec

There were four 2-month-old wild type mice femur samples. For each animal, three locations were imaged for hyperspectral data sets by O-PTIR (Photothermal Spectroscopy Corp. Santa Barbara, CA, USA). The nominal dimension of each hyperspectral data set is 5 by 130 μm. The hyperspectral data collection size is 1 by 1 μm, meaning one hyperspectral data set of 5 by 130 μm would contain 786 full IR spectra. The length of 130 μm was chosen to cover Day 1 to Week 5 bone region and determined based on fluorescence images of the bone samples. Before O-PTIR was employed to collect hyperspectral data, single IR spectrum from the test, Polyethylene terephthalate (PET) sample with the known IR spectrum was obtained and compared to peak ratios across all PET spectra to make sure that O-PTIR would collect consistent chemical signal as a quality assurance. O-PTIR was operated at IR power, 80 % and probe power, 10% with a QCL laser. The spectral range was 800 to 1840 cm^{-1} with a spectral resolution of 2 cm^{-1}. This setting was used throughout the entire sample set to make sure that the Amide I/mineral ratio values would change as a function of tissue ages not from different laser powers.

Raw hyperspectral data from PTIR studio (Photothermal Spectroscopy Corp. Santa Barbara, CA, USA) was converted to the ASC II format. The converted hyperspectral file was

imported to Cytospec software (Berlin, Germany), specialized for processing hyperspectral data sets. The imported file was processed with two steps; 1) Noise reduction with 0 to 20 setting and 2) Savitzky-Golay filter with the polynomial order as 3 and side points as 11. The processed hyperspectral was used to generate IR ratio values of Amide I/mineral (peak area 1694 to 1626 cm^{-1})/(peak area 1130 to 900 cm^{-1}). Instead of integrating full peak of 1200 to 900 cm^{-1} for the ratio values from AFM-IR, the peak range was limited up to 1130 cm^{-1} since after 1130 cm^{-1} wavenumber, the QCL laser output was significantly reduced, meaning the noise level after 1130 cm^{-1} was too high.

3.3.9 Statistical analysis

There are two statistical analyses employed for this study; 1) The one-way analysis of variance (ANOVA) with Tukey's test as a mean comparison. This analysis was used to analyze box plots within individual location where only the variable is tissue age.

For the Amide I/mineral ratios values from multiple locations and animals, the linear mixed effect model was employed to compare the ratio values with multiple variables. Lme4 package with RStudio was chosen for this analysis. A long format for lme4 package was constructed with 5 levels; 1) genotypes, 2) drug treatment, 3) animals, 4) locations, and 5) tissue ages. In this chapter, the genotypes and drug treatment are excluded since the samples are all wild type (WT) animals with different locations and tissue ages.

3.4 Results

3.4.1 Summary of animal samples and experimental techniques in Chapter 3

Table 3.1 Summary of wild type mice femur samples specifying tissue age, number of locations per animal, characterization techniques, and data collected.

Tissue age	Sample ID	Location ID	Characterization techniques	Figure types generated	Data collection step size
6-month-old	N030	Loc 1	AFM-IR	IR ratio image, domain size and box plot	33 by 33 nm
		Loc 2		IR ratio image, domain size and box plot	
	N041	Loc 1		IR ratio image and box plot	33 by 66 nm
		Loc 2		IR ratio image and box plot	
	N045	Loc 1	AFM-IR & EDX	IR ratio image and box plot, Ca and P element concentration	33 by 66 nm for AFM-IR, 200 by 200 nm for EDX
		Loc 2	AFM-IR	IR ratio image, domain size and box plot	33 by 33 nm
	N070	Loc 1		Box plot from individual IR spectra	1 by 1 μm
	N046	Loc 1	AFM-IR*	IR ratio image overlapped with IR ratio values from individual IR spectra	33 by 33 nm
2-month-old	N448	Loc 1	AFM-IR & Raman	Box plot from individual IR spectra and data points from individual Raman spectra	1 by 1 μm for AFM-IR
		Loc 2	O-PTIR	Box plot from hyperspectral data sets	1 by 1 μm
		Loc 3			
		Loc 4			
	367	Loc 1			
		Loc 2			
		Loc 3			
	368	Loc 1			
		Loc 2			
		Loc 3			
	N383	Loc 1			
		Loc 2			
		Loc 3			

* Data collected with Bruker NanoIR 3 instrument. All other AFM-IR data collected with Anasys NanoIR 2 instrument.

There are total 9 femur samples from 9 individual wild type mice. The mice are further divided into two age groups; 6-month-old and 2-month-old. The 6-month-old age group was employed to represent mature bone whereas the 2-month-old age group was employed to represent rapidly growing bone. Four different characterization techniques were employed: 1) AFM-IR using an Anasys nanoIR2 or Bruker nanoIR3 instrument; 2) Optical photothermal infrared (O-PTIR) spectroscopy; 3) Raman spectroscopy; 4) energy-dispersive X-ray (EDX) analysis.

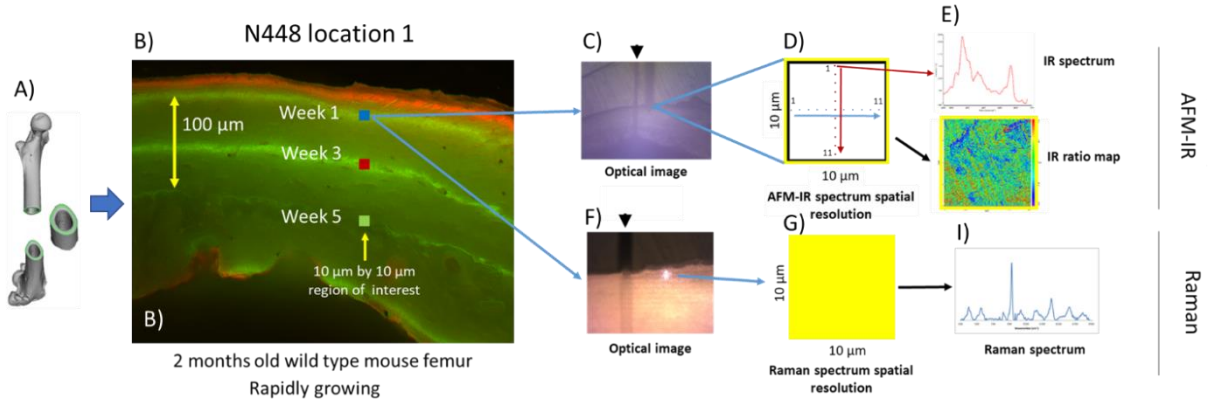

Figure 3.2 Summary of AFM-IR spectroscopy (C, D, E) and Raman spectroscopy (F, G, I) locations for data collection on 2-month old wild type mouse femur. A) Femur cross-section. B) Fluorescence microscopy with imaging sample locations. C) Optical image from AFM-IR microscope D) Locations of horizontal and vertical IR spectra obtained within 10 µm region. E) Examples of AFM-IR spectra and images F) Optical image from Raman microscope. G) Raman spectral resolution is approximately equal to the 10 x 10 µm region. I) Example of Raman spectrum. The colored squares indicating imaging regions in panel B are drawn to scale. The colored circles in panel D indicate the locations of IR spectra but are drawn substantially larger than scale to be visible.

AFM-IR and Raman spectroscopies were employed to compare the overall trend of Amide I/mineral ratio values over different tissue ages (Figure 3.2). The fluorescence image of 2-month-old wild type mouse femur contains 4 fluorochrome labels indicating a corresponding tissue age (Figure 3.2B). The red line indicates 1-day-old bone. The 1st, 2nd, and 3rd green lines indicate tissue ages of 1, 3, and 5 weeks old, respectively. The yellow double-headed arrow indicates the distance from week 1 to week 5 bone. Optical images of the mouse femur from AFM-IR (Figure 3.2C) and Raman spectroscopy (Figure 3.2F) were used to obtain chemical data from two techniques at locations of comparable tissues age. The black arrowheads indicate a cut line serving as a fiducial mark to aid in acquiring AFM-IR and Raman data over similar regions of interest.

3.4.2 AFM-IR and Raman data obtained from the same 2-month-old wild type mouse femur

As shown in Figure 3.3, the overall average Amide I/mineral ratio values and ratio ranges (defined as whiskers and box ranges in Figure 3.3) decrease as bone tissue becomes mature. Figure 3.3A and C illustrate that the largest ratio changes occur after Week 1 tissue age. For the horizontal and vertical directions, the average ratio values change from 1.6 to 1.1 and 1.8 to 1.0, respectively. However, the average ratio values do not significantly differ between Week 3 and Week 5, compared to Week 1. The Amide I/mineral ratio variation is the largest for Week 1 as well. The ratio ranges and the standard deviation decrease as tissue becomes mature. A one-way ANOVA analysis indicates the Week 1 Amide I/mineral ratio data for the horizontal and vertical directions are statistically different from Week 3 and Week 5 data. However, Week 3 and Week 5 IR ratio values are not statistically different (p = 0.99 for H 2 & H3, p = 0.63 for V2 & V3).

Comparatively, Raman spectra spatial resolution is ~10 by 10 μm. Raman-derived Amide I/mineral ratio values (1662 cm^{-1}/958 cm^{-1}[11]) over the similar week 1, 3, and 5 bone regions are 0.23, 0.08 and 0.09 respectively. Figure 3.3D illustrates that with normalized Amide I/mineral ratio values from Raman and AFM-IR (both horizontal and vertical directions), the overall Amide I/mineral ratio trend from Raman agrees with that of AFM-IR. However, the ratio data from AFM-IR demonstrates how the Amide I/mineral ration variation changes within bone regions where Raman can provide a single ratio value.

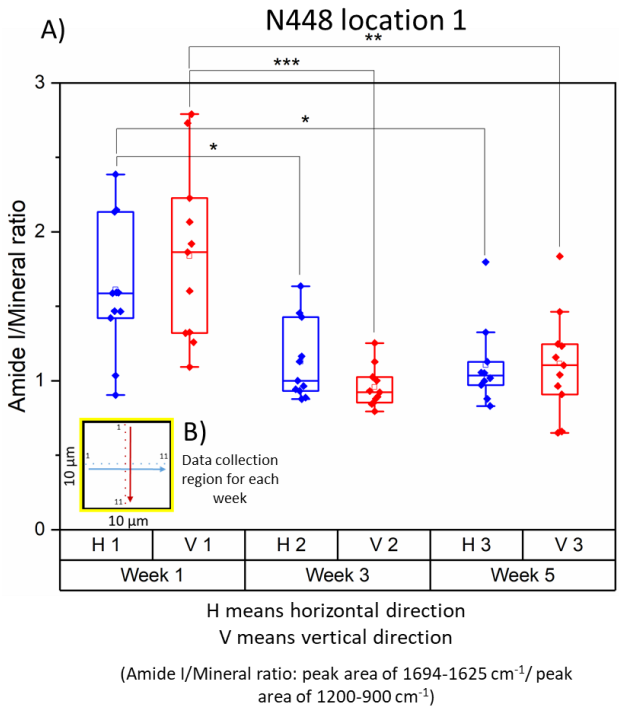

C)

Tissue Age	Horizontal IR ratio values average	Vertical IR ratio values average
Week 1	1.6 ± 0.4	1.8 ± 0.6
Week 3	1.1 ± 0.3	1.0 ± 0.1
Week 5	1.1 ± 0.3	1.1 ± 0.3

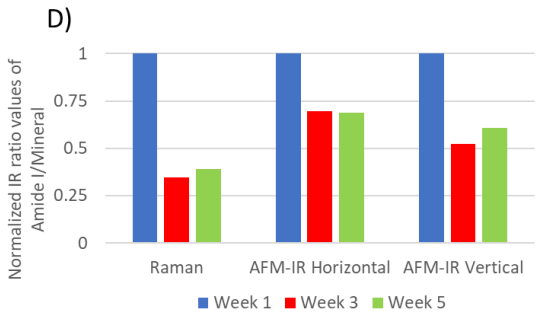

Figure 3.3 Amide I/mineral ratios (defined as peak area of 1694-1625 cm^{-1} / peak area of 1200-900 cm^{-1}) obtained using AFM-IR for 2-month-old mice femur collected from the 1 µm spaced horizontal (H: blue label) and vertical (V: red label) locations for week 1, 3, and 5 tissue ages as highlighted in Figure 3.2. A) Box plots of Amide I/Mineral ratios. Each plot contains 11 data points except Week 5 H box (10 data points due to a high noise level). B) Location of horizontal and vertical spectra collected with 1 um spacing in 100 μm^2 box. C) Average ratio values for week 1, 3, and 5. D) Bar graph showing normalized IR and Raman spectroscopy Amide I/mineral ratio values for corresponding tissue ages. (* p <0.05, ** p <0.005, *** p < 0.0005). W = week, in all cases. (Whisker ranges; H1- 0.9 to 2.4, V1- 1.1 to 2.8, H2-0.9 to 1.6, V2- 0.8 to 1.3, H3 -0.8 to 1.3 and V3- 0.7 to1.5). (Box ranges; H1- 1.4 to 2.1, V1- 1.3 to 2.2, H2- 0.9 to 1.6, V2- 0.9 to 1.0, H3- 1.0 to 1.1 and V3- 0.9 to 1.2)

3.4.3 AFM-IR data obtained from 6-month-old wild type mouse femur

Similar to the Amide I/mineral ratio values from the 2-month-old femur, the AFM-IR data from 6-month-old femur displays a consistent trend; as tissue becomes mature, the average Amide I/mineral ratio values decrease along with the ranges and standard deviations. The average IR ratio values decrease from 2.4 to 0.7 for the horizontal direction and 1.3 to 0.9 for the vertical direction. For this data set, the degree of the ratio value change is larger for the horizontal direction than the vertical direction. The IR ratio ranges and standard deviations from

Figure 3.4C and D show a steady decline over tissue age. However, the statistical difference between W1 to W3, W3 to W5 and >W5 (older than Week 5 tissue age) for the vertical direction is not significantly different from one another (p = 0.16 for W1 to W3 & W3 to W5, p = 0.17 for W1 to W3 & >W5, p = 0.93 for W3 to W5 & >W5).

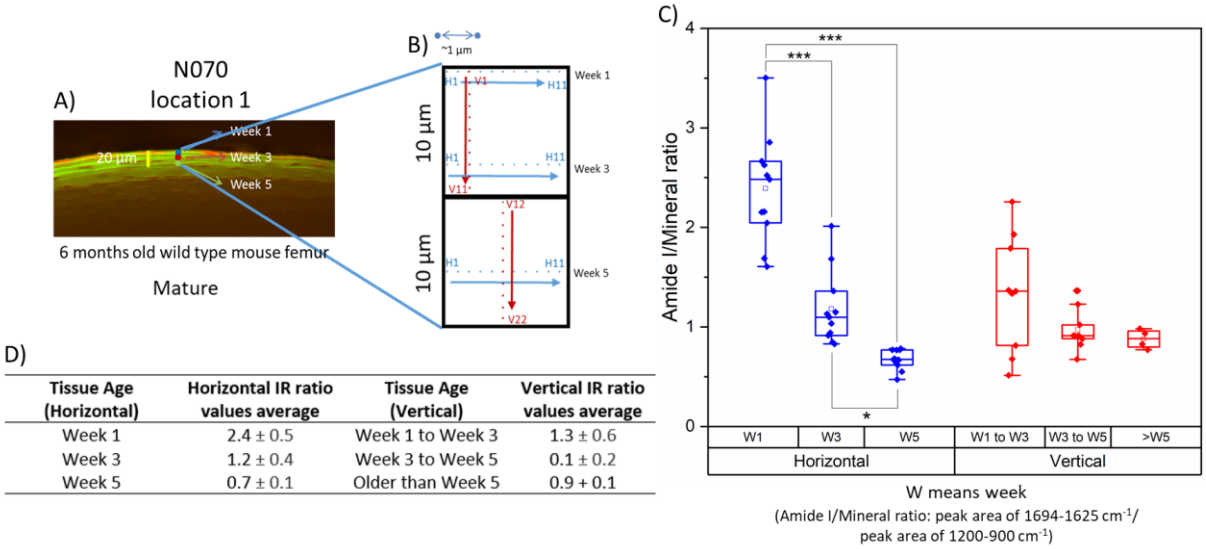

D)

Tissue Age (Horizontal)	Horizontal IR ratio values average	Tissue Age (Vertical)	Vertical IR ratio values average
Week 1	2.4 ± 0.5	Week 1 to Week 3	1.3 ± 0.6
Week 3	1.2 ± 0.4	Week 3 to Week 5	0.1 ± 0.2
Week 5	0.7 ± 0.1	Older than Week 5	0.9 + 0.1

Figure 3.4 Amide I/Mineral ratios (defined as peak area 1694-1625 cm^{-1} / peak area 1200-900 cm^{-1}) obtained using AFM-IR for 6-month-old mice femur. A) Fluorescence image of 6-month-old wild type mouse femur B) Location of horizontal and vertical spectra collected with 1 um spacing in 100 μm^2 box. C) Box plot of Amide I/Mineral ratio for week 1, 3 and 5 tissue ages. Each horizontal box plot contains 11 data points while W1 to W3 and W3 to W5 vertical box plots contain 9 data points each and >W5 vertical box plot contains 4 data points. D) Average IR ratio values from horizontal and vertical directions for week 1, 3, 5 and >W5 with standard deviations. (* p <0.05 for W3 & W5, *** p < 0.0005 for W1 &W 3 and W1 and W5, all for horizontal direction) (p = 0.16 for W1 to W3 & W3 to W5, p = 0.17 for W1 to W3 & >W5, p = 0.93 for W3 to W5 & >W5, all for vertical direction). W = week in all cases.

3.4.4 AFM-IR data obtained from Amide I/mineral ratio maps from 6-month-old wild type mouse femurs

The IR ratio map Figure 3.5C is divided into two parts; 1) top half and 2) bottom half. The top half IR ratio map shows a larger amount of bone area occupied by the green colored region indicating higher IR ratio values than the blue colored region indicating lower IR ratio values. The bottom half IR ratio map shows the opposite trend. Along with the IR ratio map, two

histograms from Figure 3.5B demonstrate the same trend; Day 1 to Week 3 bone region (less mature bone region) has higher Amide I/mineral ratio values with a wider distribution compared to Week 3 to Week 5 bone region (more mature bone region), where the width of its histogram is a half of the histogram from the top half region. Three full IR spectra, locations noted by red circles, from Figure 3.5D agree with the overall IR ratio trend with the IR ratio map. The IR ratio map from Figure 3.5E displays the consistent map features regardless of the scan direction. Consistent IR ratio maps, independent of AFM scan direction, are also demonstrated by additional data in Figure B.2 with much smaller two 3 by 3 μm images instead of 10 by 10 μm. The IR ratio map and histograms from sample N046 acquired using a Bruker NanoIR 3 (a newer version of AFM-IR) are shown in Figure B.1 in Appendix B and are consistent with trends illustrated in Figure 3.5.

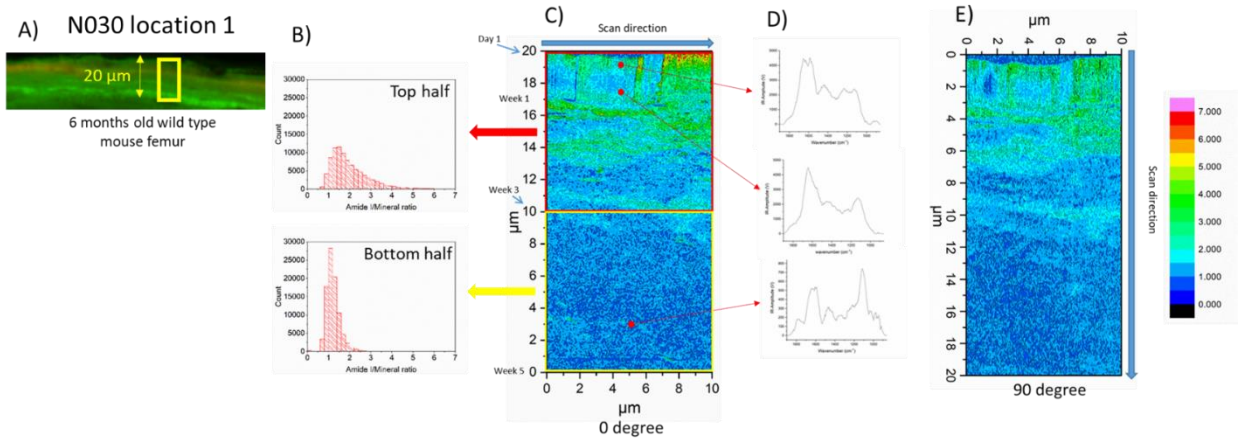

Figure 3.5 Amide I/Mineral ratio (defined as 1676 cm^{-1}/1080 cm^{-1}) maps obtained using AFM-IR as a function of scan angle (0 and 90 degree). A) Fluorescence microscope image of 6-month-old wild type mouse femur. The vertical yellow box indicates the area where IR data was collected. B) Histograms of each 10 x 10 μm IR ratio map from panel C. C) IR ratio map from day 1 to week 5 measured using a 0 degree scan (standard operating condition) D) Individual IR spectra obtained from red circled regions on the IR ratio map. E) IR ratio measured using a 90-degree scan angle.

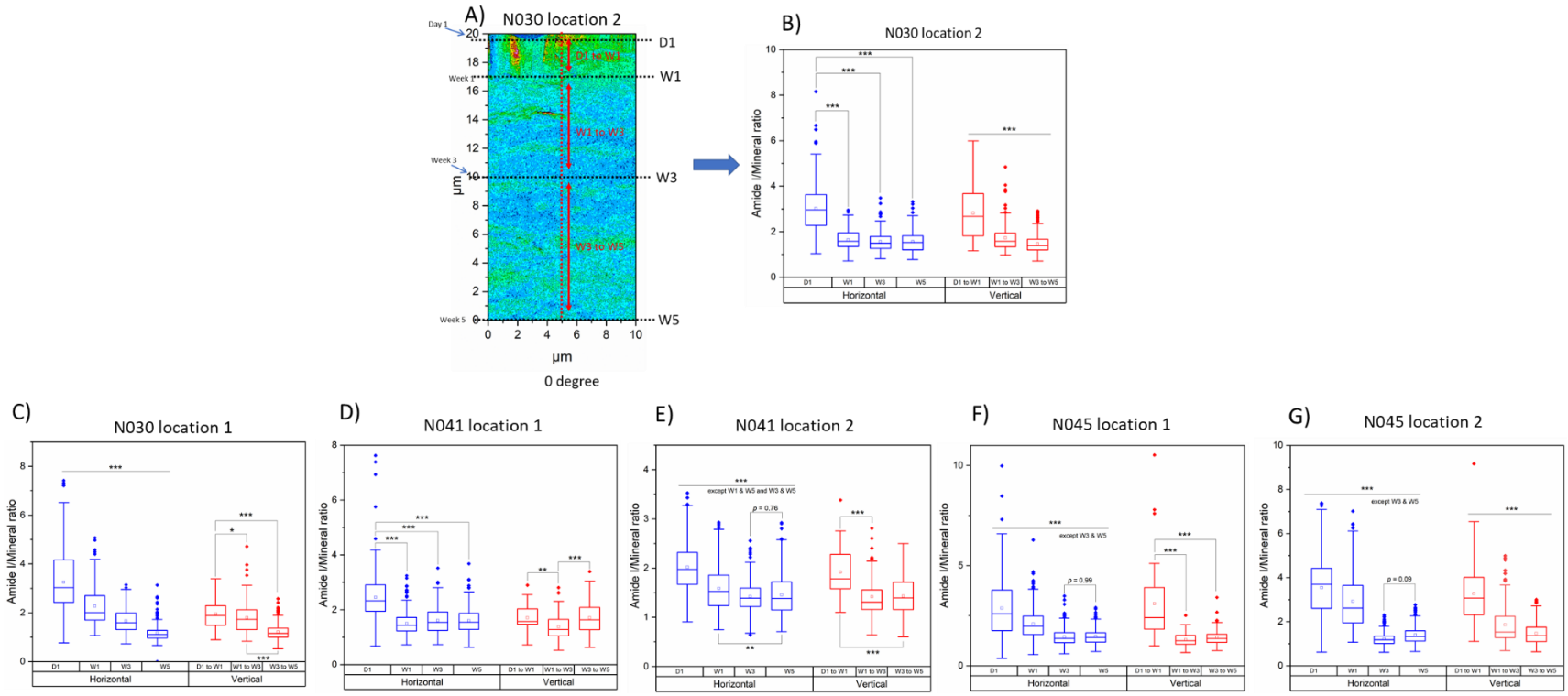

Figure 3.6 Box plots summarizing Amide I/mineral ratio values as a function of sample and tissue age. A) Amide I/mineral ratio map indicating horizontal and vertical cross-section of data used to generate box plots. B-G) Box plots of Amide I/mineral ratios. The ratio values for N030 and N041 are based on Amide I (1676 cm^{-1})/mineral (1080 cm^{-1}). For N045, Amide I (1664 cm^{-1})/mineral (1108 cm^{-1}). Amide I values were selected based on the average maximum peak position. IR ratio images for panels C) through G) are provided in Figure B.3 in Appendix B. All box plots consistently show that as bone samples become mature, the mean IR Amide I/mineral ratio values decrease as well as the extent of IR ratio variation. (* p <0.05, ** p <0.005, *** p < 0.0005). D = day, W = week in all cases.

There are total of three samples producing six Amide I/mineral ratio maps by AFM-IR (all six IR ratio maps are presented in Figure B.3 in Appendix B. Each IR ratio map generates one set of box plots presented by Figures 3.6B through G. There are two consistent trends from the box plot sets; 1) as tissue becomes mature, the average Amide I/mineral ratio values decrease. The largest change is observed after Week 1 tissue age. 2) as tissue becomes mature, the Amide I/mineral ratio range decreases. Those two trends are consistent with the previous data sets shown in Figure 3.3 and 3.4. For all box plot sets, the IR ratio values from Day 1 are statistically different from the rest of the IR ratio values from more mature tissues. However, after Day 1, the box plot sets show location to location and animal to animal variations. For instance, two box plot sets (Figure 3.6B and C) from sample N030 exhibit statistically different IR ratio trends. Four box plots from the horizontal direction of N030 location 1 in Figure 3.6C are all statistically different from one another. However, for another four box plots from the horizontal direction of N030 location 2 in Figure 3.6B, only the IR ratio values from Day 1 are statistically different from the rest of the box plots. Also, box plot sets from sample N041 and N045 have different statistical significances among different tissue regions. Another trend emerging from the box plot sets is that between Week 3 and Week 5 for the horizontal direction except N030 location 1, the IR ratio values from these two tissue ages are not chemically significantly different.

3.4.5 Domain sizes analysis from Amide I/mineral ratio maps from 6-month-old wild type mouse femurs

The I-shaped box plots from three locations show different domain size ranges sorted by different IR ratio value ranges. The domain sizes belonging to lower IR ratio values tend to be larger (or the range of the domain sizes is wider). The IR ratio range from 1 to 2 exhibits the

largest domain size range nominally up to 700 nm dimeter. After the IR ratio range 3 to 4, the domain sizes tend to be smaller as shown in Figure 3.7C. The combined box plot data from Figure 3.7F shows the nominal range of the domain sizes is from ~50 to 500 nm except the box plot for the IR ratio range of 1 to 2. Examples of each measured individual domains with different thresholds can be found in Figure B.4.

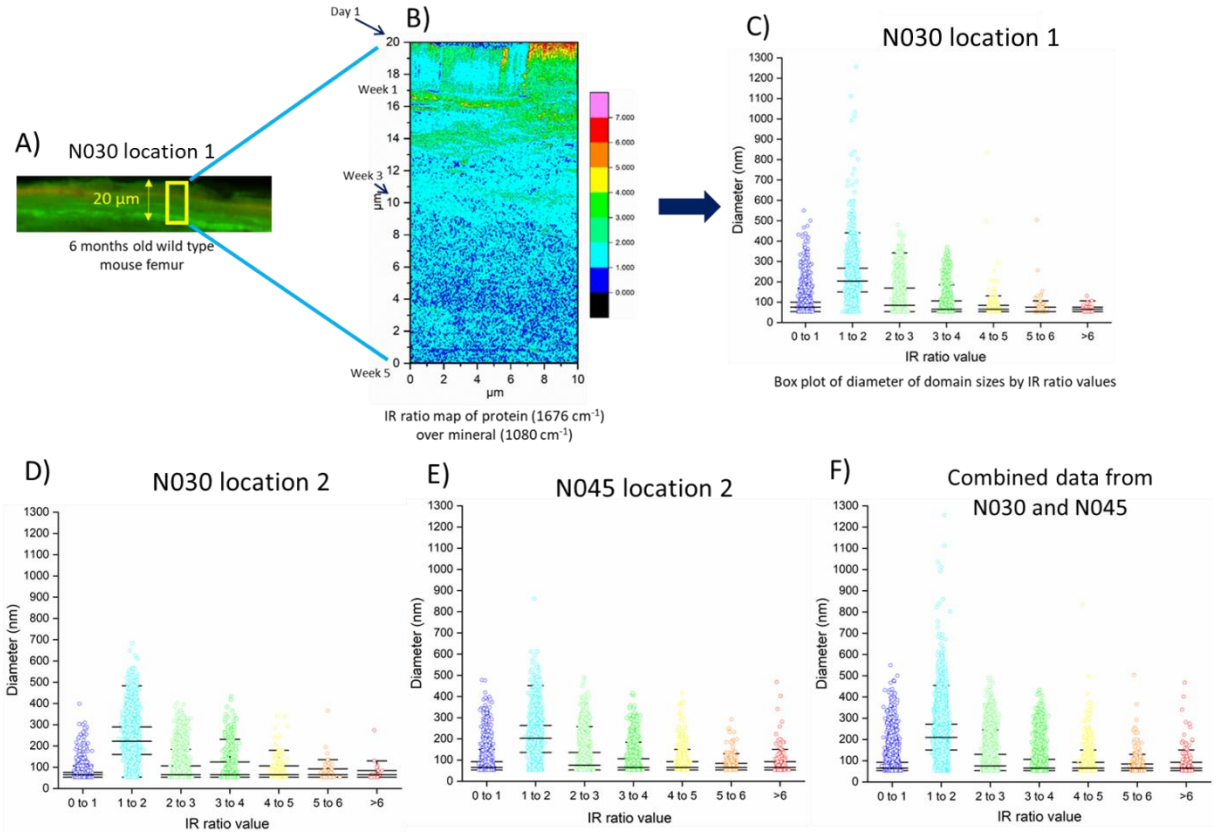

Figure 3.7. Quantification of domain sizes for a given range of Amide I/mineral ratios. A) Exemplar fluorescence microscope image indicating location of IR map B) Exemplar IR ratio map C) I-shaped box plot summarizing domain size as a function of Amide I/mineral ratio for data shown in panel B, N030 location 1 D) I-shaped box plots for N030, location 2 E) I-shaped box plots for N045, location 2. F) I-shaped box plot containing all three data sets. The color of each I-shaped box plot matches the color scale of the IR ratio map. There are four black lines for each I-shaped box plot. Two outer lines indicate whisker ranges. Two inter lines indicate box ranges.

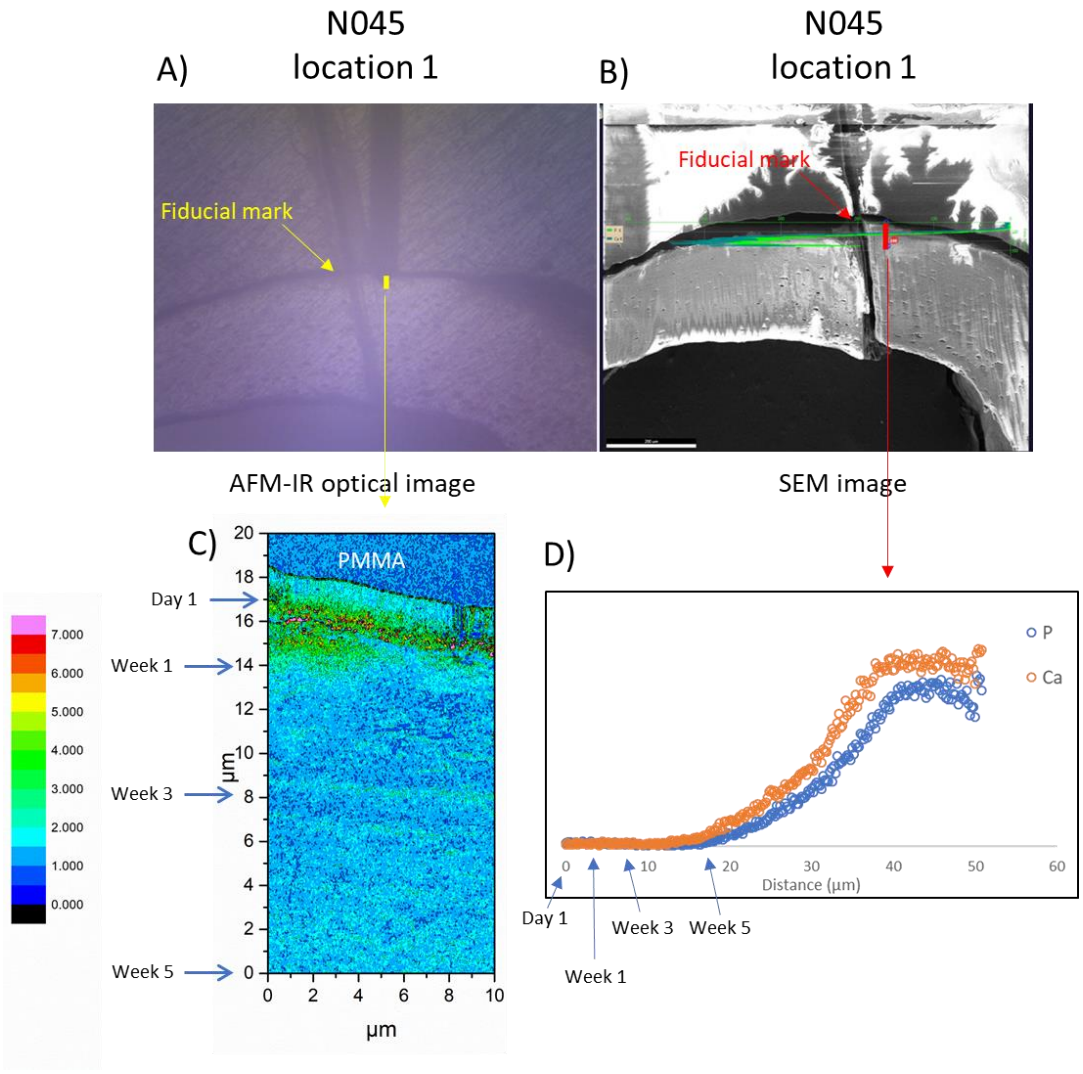

Figure 3.8 Comparison of AFM-IR derived Amide I/mineral ratio map and EDX measurement of P and Ca for wild type mouse femur. A) Optical image from AFM-IR microscope indicating location of IR ratio map of sample N045 is obtained. B) SEM image of EDX data location. C) IR ratio map of Amide I/Mineral ratio (1664 cm^{-1}/1108 cm^{-1}). D) EDX data of phosphorus and calcium concentration. The IR ratio map indicates the lowest mineralization level is from day 1 to week 1where the EDX data does not show a significant level of P and Ca concentration.

3.4.6 A comparison between the Amide I/mineral ratio map from AFM-IR and calcium and phosphorus measurement from EDX

The Amide I/mineral ratio map from Figure 3.8C exhibits the highest IR ratio values identified in the bone region between Day 1 and Week 1. The box plots from N045 location 1 in Figure 3.6F indicates that the Amide I/mineral ratio values decrease up to Week 1 tissue age and

becomes constant between Week 3 and Week 5. On the other hand, EDX data shows that until Week 5 tissue age, calcium (Ca) and phosphorus (P) concentration does not increase much and starts to increase after Week 5. The Ca and P concentration increases steadily up to 40 μm distance from D1 tissue age.

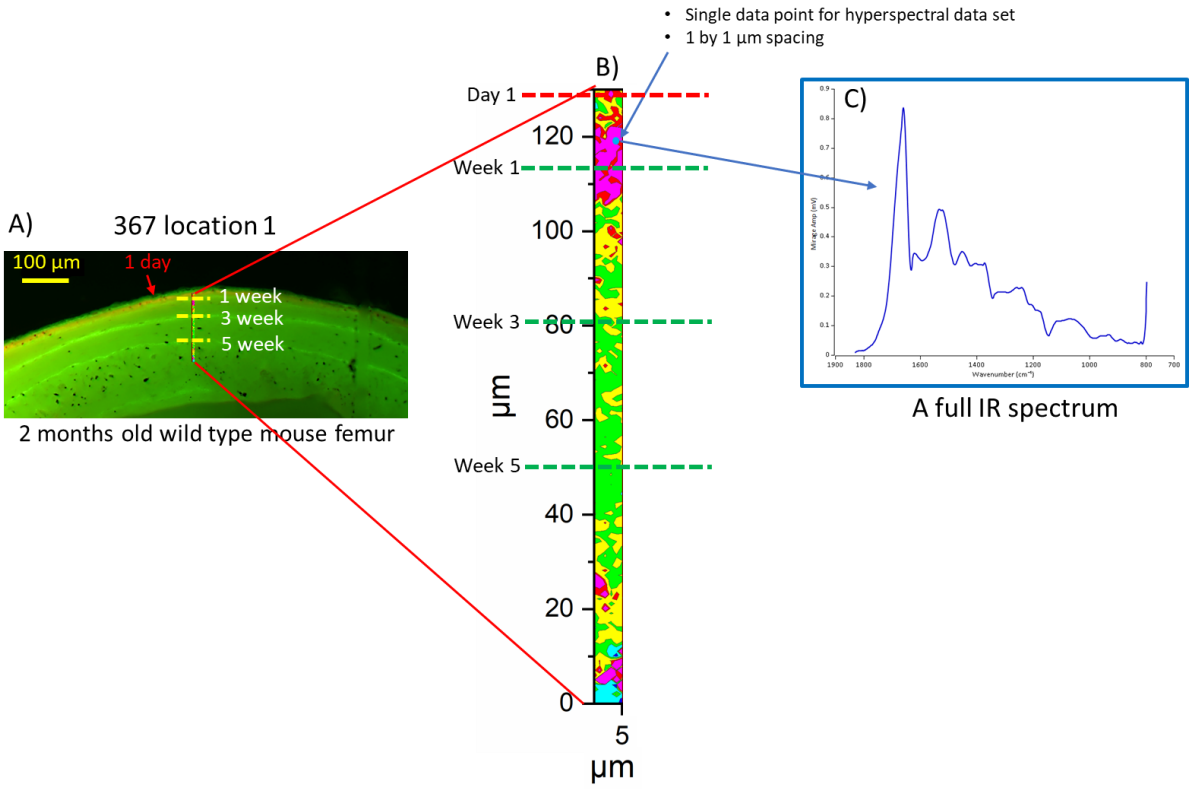

Figure 3.9 Amide I/mineral ratio map (peak area 1694 to 1626 cm^{-1})/(peak area 1130 to 900 cm^{-1}) obtained from hyperspectral optical photothermal infrared (OPTIR) spectroscopy data set. A) Exemplar fluorescence microscope image indicating location of four different tissue ages. B) Exemplar IR Amide I/mineral ratio map. The blue dot represents an approximate step size of IR data collection (1 by 1 μm). C) Exemplar IR spectrum taken from location indicated blue dot obtained from the hyperspectral O-PTIR data set.

3.4.7 O-PTIR data from 2-month-old wild type mouse femurs

Figure 3.9 illustrates O-PTIR hyperspectral data. Hyperspectral data set is obtained from each location of a 2-month-old mouse femur sample. In this chapter, hyperspectral data set is defined as two-dimensional chemical map where each data point is a full IR spectrum rather than

a ratio value from two single wavenumber IR maps. The data collection step size is 1 by 1 μm, generating 786 full IR spectra for each location at minimum. With this type of data set, it is possible to continuously measure and fully capture chemical information from Day 1 to Week 5.

The box plot sets from four samples (N448, 367, 368 and N383) in Figure 3.10 show the IR ratio differences observed in location to location and animal to animal variations. Sample N448 shows the location to location variations; the box plots from N448 location 4 display the declining Amide I/mineral ratio values over tissue age which is consistent the IR ratio trend observed with AFM-IR. On the other hand, N448 location 2 and 3 exhibit tissue regions where the ratio values are higher than the younger tissue regions. In addition to the location to location variation, the animal to animal variation is apparent as well. The IR ratio values from sample 367 and 368 remain consistent whereas the ratio values from sample N383 decrease as tissue becomes mature. Different animals also demonstrate different overall IR ratio ranges. For instance, the average Amide I/mineral ratio values from sample 367 and 368 are around 0.5. On the contrary, the average Amide I/mineral ratio values from sample N448 and N383 are around or higher than 1.

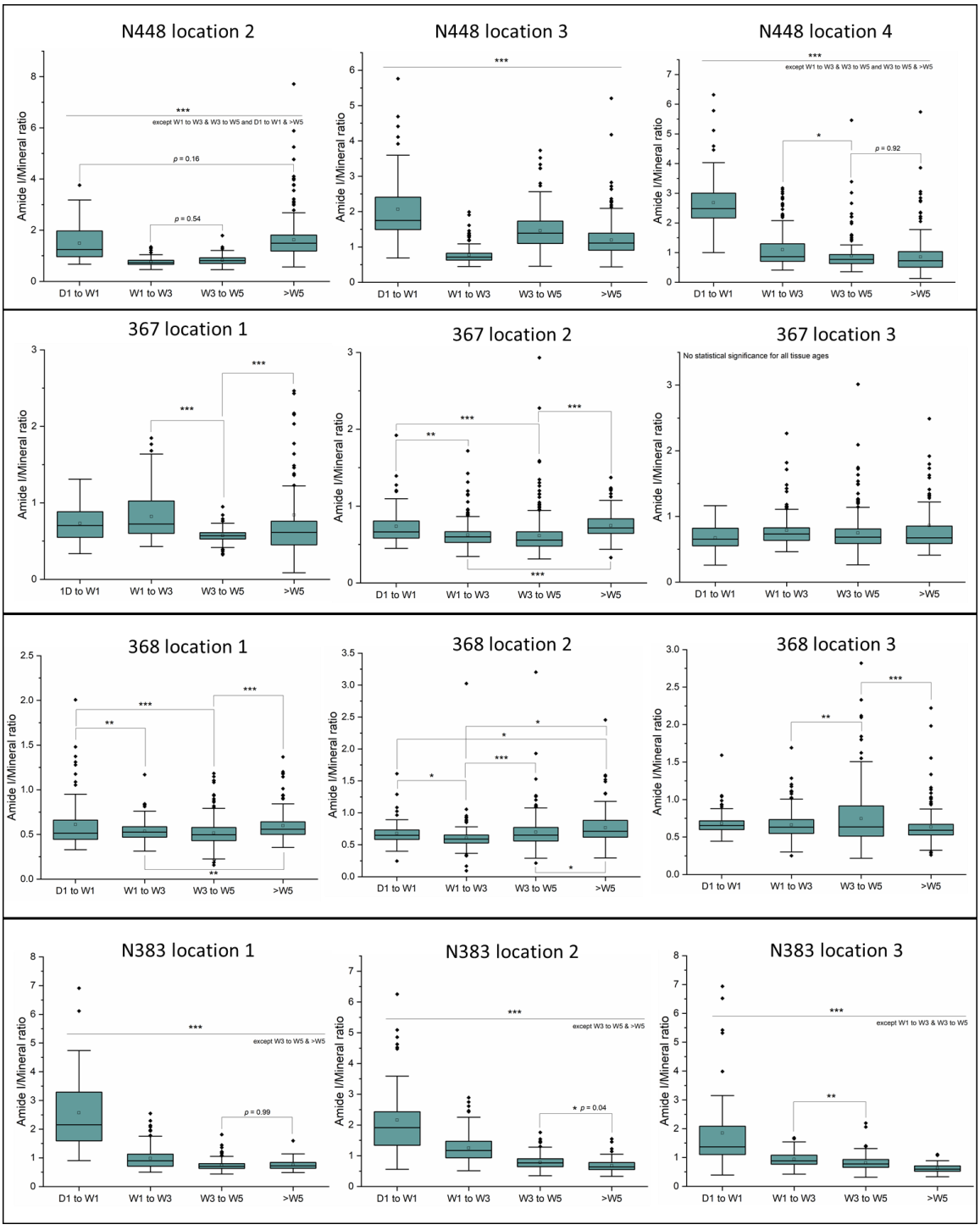

Figure 3.10 Box plots summarizing Amide I/mineral ratio from four 2-month-old wild type mouse femoral samples (N448, 367, 368 and N383) as measured by O-PTIR following approach illustrated in Figure 3.9. Three locations were sampled for each animal. The four tissue ages are assigned based on fluorescence images. The IR ratio maps associated with this data set are provided in Figure B.6 in Appendix B. (* p <0.05, ** p <0.005, *** p < 0.0005). D = day, W = week in all cases.

Table 3.2 Summary of linear mixed effect model results showing how Amide I/Mineral ratio values from D1 to W1, W1 to W3, and W3 to W5 differ from the most mature tissue (>W5 tissue age), including all locations and animals for all WT samples (N448, 367, 368 and N383) measured by O-PTIR.

	Relative Change (%)	Std. Error (%)	Probability
D1 to W1 Tissue Age	-1	6	0.82
W1 to W3 Tissuge Age	-3	6	0.58
W3 to W5 Tissue Age	-8	6	0.19

* IR ratio values from each tissue ages (D1 to W1, W1 to W3 and W3 to W5) from all locations and animals from the four mice femurs are compared to IR ratio values obtained from >W5 tissue age (bone regions of older than week 5 tissue age)

To perform the linear mixed effect model, one data group should be set as a reference point. In this particular analysis, the IR ratio values of Amide I/Mineral from >5W region (tissue older than week 5 age) are compared to the ratio values from D1 to W1, W1 to W3 and W3 to W5. The relative change indicates how the average IR ratio value from each tissue group is different from the average IR ratio value of >W5. The three groups possess 1 to 8% lower IR ratio values compared to >W5. However, the relative changes from D1 to W1 and W1 to W3 are within the error range of the analysis. In addition to that, the statistical analysis suggests the average IR ratio values from D1 to W1, W1 to W3 and W3 to W5 are not significantly different from >W5 based on the *p* values from Table 3.2.

3.5 Discussion

3.5.1 The Amide I/mineral ratio changes from AFM-IR and O-PTIR compared to conventional spectroscopy techniques

Most of the Amide I/mineral ratio data sets (except sample 367 and 368) from AFM-IR and O-PTIR in this chapter demonstrate the IR ratio values decreasing with increased tissue age.

The decreasing ratio values indicate increasing mineralization level with tissue age. This trend is well documented in literature[9,30] and agrees with our overall Amide I/mineral ratio trend. Imbert et al. employed AFM-IR (NanoIR 2) to run a similar experimental procedure on chemically fixed and dehydrated vertebral biopsies from ovariectomized (OVX) sheep. They found increasing mineral to matrix ratio values over tissue age, indicating the increasing mineralization as the ratio values were obtained from younger to more mature bone regions.[24] However, this study did not provide the ratio changes associated with specific tissue ages. Also, the sample they used were chemically dehydrated as our sample sets did not go through any chemical treatments.

Sinder et al. previously performed Raman spectroscopy on the same set of the 2-month-old and 6-month-old mice femur samples used for AFM-IR and O-PTIR. They chose the ratio value of mineral/matrix (proline intensity) as their bone quality parameter instead of matrix/mineral used for our data sets. For the 2-month-old mice femurs samples, the mineral/matrix ratio values increased and peaked at Week 3 tissue age. After the Week 3 tissue age, however, the mineral/matrix ratio values reached plateau. On the other hand, the mineral/matrix ratio values from the 6-month-old samples kept increasing over time.[28]

Our AFM-IR data and Raman data from the 2-month-old sample in Figure 3.3 agree with the findings by Sinder et al. The average Amide I/mineral ratio values from Week 3 and Week 5 are over 30 % reduced, compared to the average ratio values from Week 1. However, the average ratio values remain consistent between Week 3 and Week 5 and these are not statistically different. Also, our ratio values from Raman decrease from 0.23 (Week 1) to 0.1 (Week 3) and 0.1 (Week 5).

The AFM-IR data from the 6-month-old sample in Figure 3.4 is consistent with the ratio trend by Sinder et al. for the horizontal direction; the average Amide I/mineral ratio values keep decreasing in a statistically significant fashion from Week 1 through Week 5 in Figure 3.4. The Amide I/mineral ratio values from both Figure 3.3 and 3.4 are calculated from individual IR spectra with 1 μm spacing, which is similar to how the ratio value were obtained by Sinder et al. with ~ 3 μm spacing in the y-direction.[28]

When the average Amide I/mineral ratio values are extracted from the IR ratio maps with the 33.3 nm data acquisition step size in Figure 3.6, instead of individual full IR spectra, the average IR ratio value trends differ depending on different locations and animals. The difference can come from much higher number of data points from the IR ratio map, capturing chemical variation in more details compared to the full IR and Raman spectra with an order of higher data acquisition step size. Also, the AFM-IR data sets from Figure 3.3 through 3.6 reveal how the range of Amide I/mineral ratio values decreases over time in much finer spatial scale compared to the conventional IR or Raman techniques.

3.5.2 Domain size range comparison between the IR ratio maps and mechanical maps

The nominal domain size range from the mechanical maps by Tai et al.[14] is from ~100 to 500 nm, which agrees with the nominal domain size calculated from the IR ratio maps in Figure 3.7. The mineral component in bone is associated with bone stiffness[7] and the Amide I/mineral ratio values indicate overall mineralization level in bone. Therefore, it is plausible to think that the different nanoscale mineralization level in bone identified by the IR ratio maps can be one of contributing factors for bone to possess nanoscale mechanical heterogeneity. However, our frequency maps in Figure B.7 do not show correlations between the IR ratio maps and frequency maps. This discrepancy could come from the fact that the depth of penetration of the

IR laser, according to the manufacture, is around 1 to 3 μm whereas AFM technique is much more sensitive to a sample surface.

3.5.3 The Amide I/mineral ratio map from AFM-IR, and Ca and P measurement from EDX data

The ratio map in Figure 3.8C show the largest Amide I/mineral changes from Day 1 to Week 1. However, Ca and P concentration in Figure 3.8D remains steady up to 20 μm and starts to increase rapidly after 20 μm. The Amide I/mineral ratio trend and EDX data do not correlate. This discrepancy can be caused by a different spatial resolution (surface) and depth of penetration. EDX typically possesses a spatial resolution about 1 μm[31] and a depth of penetration about several to tens of micrometers.[32] AFM-IR having ~50 nm as a spatial resolution and 1 to 3 μm as a depth of penetration can obtain chemical information with an order of smaller length and several times more sensitive depth scale. Considering these differences between two techniques, it is reasonable to think that EDX is not capable of detecting the mineralization change occurring from Day 1 to Week 1 region.

3.5.4 Chemical variation among different locations and animals observed by O-PTIR

Figure 3.10 demonstrates chemical heterogeneity of Amide I/mineral ratio values across different locations and animals. The box plots from sample N383 display the ratio trend observed by Sinder et al.[28] and in Figure 3.3. However, the box plots from sample 367 and 368 show the similar average IR ratio values across all four tissue ages with 30% reduced average IR ratio values compared to sample N448 and N383. The presence of the Amide I/mineral ratio values from 367 and 368 might lead to the results in Table 3.2 where all three younger tissue ages (Day 1 to Week 1, Week 1 to Week 3, and Week 3 to Week 5) are not statistically different from the most mature tissue age (>Week 5) when the total number of the Amide I/mineral ratio values

from all data sets are considered at the same time. Additionally, the Amide I/mineral IR ratio maps in Figure B.6 in Appendix B reveal the spatially heterogenous nature of the Amide I/mineral ratio values across the tissue regions, which the box plots cannot capture.

In conclusion, although this study is not the first AFM-IR study on bone, it is the first study to combine AFM-IR with the bone samples with fluorescence marks indicating specific tissue ages. Thus, we can understand how the Amide I/mineral ratio values behave as a function of different tissue ages. Also, this is the first application of O-PTIR on characterizing chemical composition of bone with full hyperspectral data sets (rather than IR ratio maps from single wavenumber images) with about a ten-time smaller data acquisition step size, compared to conventional spectroscopy techniques.

3.6 References

[1] H.P. Schwarcz, D. Abueidda, I. Jasiuk, The ultrastructure of bone and its relevance to mechanical properties, Front. Phys. 5 (2017) 1–13.

[2] N. Reznikov, R. Shahar, S. Weiner, Bone hierarchical structure in three dimensions, Acta Biomater. 10 (2014) 3815–3826.

[3] N. Reznikov, M. Bilton, L. Lari, M.M. Stevens, R. Kröger, Fractal-like hierarchical organization of bone begins at the nanoscale, Science. 360 (2018) eaao2189.

[4] A.K. Nair, A. Gautieri, S. Chang, M.J. Buehler, Molecular mechanics of mineralized collagen fibrils in bone, Nat. Commun. 4 (2013) 1724–1729.

[5] A. Gautieri, S. Vesentini, A. Redaelli, M.J. Buehler, Hierarchical structure and nanomechanics of collagen microfibrils from the atomistic scale up, Nano Lett. 11 (2011) 757–766.

[6] J. Chen, T. Ahn, I.D. Colón-Bernal, J. Kim, M.M. Banaszak Holl, The Relationship of Collagen Structural and Compositional Heterogeneity to Tissue Mechanical Properties: A Chemical Perspective, ACS Nano. 11 (2017) 10665–10671.

[7] P. Fratzl, H.S. Gupta, E.P. Paschalis, P. Roschger, Structure and mechanical quality of the collagen–mineral nano-composite in bone, J. Mater. Chem. 14 (2004) 2115–2123.

[8] E.P. Paschalis, R. Mendelsohn, A.L. Boskey, Infrared assessment of bone quality: A review, Clin. Orthop. Relat. Res. 469 (2011) 2170–2178.

[9] A. Boskey, N. Pleshko Camacho, FT-IR imaging of native and tissue-engineered bone and cartilage, Biomaterials. 28 (2007) 2465–2478.

[10] C. de C.A. Lopes, P.H.J.O. Limirio, V.R. Novais, P. Dechichi, Fourier transform infrared spectroscopy (FTIR) application chemical characterization of enamel, dentin and bone, Appl. Spectrosc. Rev. 53 (2018) 747–769.

[11] M.D. Morris, G.S. Mandair, Raman assessment of bone quality, Clin. Orthop. Relat. Res. 469 (2011) 2160–2169.

[12] Z.X. Wang, A.A. Lloyd, J.C. Burket, S. Gourion-Arsiquaud, E. Donnelly, Altered distributions of bone tissue mineral and collagen properties in women with fragility fractures, Bone. 84 (2016) 237–244.

[13] L.M. Miller, R.J. Smith, Synchrotrons versus globars, point-detectors versus focal plane arrays: Selecting the best source and detector for specific infrared microspectroscopy and imaging applications, Vib. Spectrosc. 38 (2005) 237–240.

[14] K. Tai, M. Dao, S. Suresh, A. Palazoglu, C. Ortiz, Nanoscale heterogeneity promotes energy dissipation in bone, Nat. Mater. 6 (2007) 454–462.

[15] H. Yao, M. Dao, D. Carnelli, K. Tai, C. Ortiz, Size-dependent heterogeneity benefits the mechanical performance of bone, J. Mech. Phys. Solids. 59 (2011) 64–74.

[16] M. Fang, K.G. Liroff, A.S. Turner, C.M. Les, B.G. Orr, M.M.B. Holl, Estrogen Depletion Results in Nanoscale Morphology Changes in Dermal Collagen, J. Invest. Dermatol. 132 (2012) 1791–1797. h

[17] J.M. Wallace, B. Erickson, C.M. Les, B.G. Orr, M.M. Banaszak Holl, Distribution of type I collagen morphologies in bone: Relation to estrogen depletion, Bone. 46 (2010) 1349–1354.

[18] J.M. Wallace, B.G. Orr, J.C. Marini, M.M.B. Holl, Nanoscale morphology of Type I collagen is altered in the Brtl mouse model of Osteogenesis Imperfecta, J. Struct. Biol. 173 (2011) 146–152.

[19] M.M. Kłosowski, R. Carzaniga, P. Abellan, Q. Ramasse, D.W. McComb, A.E. Porter, S.J. Shefelbine, Electron Microscopy Reveals Structural and Chemical Changes at the Nanometer Scale in the *Osteogenesis Imperfecta Murine* Pathology, ACS Biomater. Sci. Eng. (2016) acsbiomaterials.6b00300.
[20] A. Dazzi, C.B. Prater, AFM-IR: Technology and applications in nanoscale infrared spectroscopy and chemical imaging, Chem. Rev. 117 (2017) 5146–5173.
[21] A. Dazzi, C.B. Prater, Q. Hu, D.B. Chase, J.F. Rabolt, C. Marcott, AFM-IR: Combining atomic force microscopy and infrared spectroscopy for nanoscale chemical characterization, Appl. Spectrosc. 66 (2012) 1365–1384.
[22] D. Zhang, C. Li, M. Slipchenko, C. Zhang, J.X. Cheng, Depth-resolved mid-infrared photothermal imaging of living cells and organisms at sub-micron resolution, Sci. Adv. 2 (2016) 1–7.
[23] S. Gourion-Arsiquaud, C. Marcott, Q. Hu, A.L. Boskey, Studying Variations in Bone Composition at Nano-Scale Resolution: A Preliminary Report, Calcif. Tissue Int. 95 (2014) 413–418.
[24] L. Imbert, S. Gourion-Arsiquaud, E. Villarreal-Ramirez, L. Spevak, H. Taleb, M.C.H. van der Meulen, R. Mendelsohn, A.L. Boskey, Dynamic structure and composition of bone investigated by nanoscale infrared spectroscopy, PLoS One. 13 (2018) 1–15.
[25] G. Sereda, A. VanLaecken, J.A. Turner, Monitoring demineralization and remineralization of human dentin by characterization of its structure with resonance-enhanced AFM-IR chemical mapping, nanoindentation, and SEM, Dent. Mater. 35 (2019) 617–626.
[26] L. Huang, X. Zhang, J. Shao, Z. Zhou, Y. Chen, X. Hu, Nanoscale chemical and mechanical heterogeneity of human dentin characterized by AFM-IR and bimodal AFM, J. Adv. Res. 22 (2020) 163–171.
[27] J. Chen, J. Kim, W. Shao, S.H. Schlecht, S.Y. Baek, A.K. Jones, T. Ahn, J.A. Ashton-Miller, M.M. Banaszak Holl, E.M. Wojtys, An Anterior Cruciate Ligament Failure Mechanism, Am. J. Sports Med. 47 (2019) 2067–2076.
[28] B.P. Sinder, W.R. Lloyd, J.D. Salemi, J.C. Marini, M.S. Caird, M.D. Morris, K.M. Kozloff, Effect of anti-sclerostin therapy and osteogenesis imperfecta on tissue-level properties in growing and adult mice while controlling for tissue age, Bone. 84 (2016) 222–229.
[29] C. Shi, G.S. Mandair, H. Zhang, G.G. Vanrenterghem, R. Ridella, A. Takahashi, Y. Zhang, D.H. Kohn, M.D. Morris, Y. Mishina, H. Sun, Bone morphogenetic protein signaling through ACVR1 and BMPR1A negatively regulates bone mass along with alterations in bone composition, J. Struct. Biol. 201 (2018) 237–246.
[30] P. Roschger, B.M. Misof, Basic Aspects of Bone Mineralization, Springer Nat. (2020) 89–113.
[31] C. Notthoff, M. Winterer, A. Beckel, M. Geller, J. Heindl, Spatial high resolution energy dispersive X-ray spectroscopy on thin lamellas, Ultramicroscopy. 129 (2013) 30–35.
[32] W. Chrzanowski, F. Dehghani, Standardised chemical analysis and testing of biomaterials, Woodhead Publishing Limited, 2013.

Chapter 4

Conclusions and Future Directions

4.1 Abstract

Two novel material characterization techniques (PALS and PTIR) were employed to reveal the hierarchical nature of the nanoscale pore structure in bone, changes of average Amide I/mineral ratio values and their ranges, and the Amide I/mineral domain size range in bone. We found that bone has five distinct pore sizes: 0.6 nm (intra collagen molecule); 1.1 nm (inter collagen molecule); 1.9 nm (two terminal ends in collagen microfibril); 4 nm (interface between collagen and mineral structure); and 5-6 nm (spacing between two mineral plates). PALS data on the deproteinized bone samples suggests that the nanoscale mineral structure is likely to be interconnected. We also deduced a mineral plate thickness of around 4-8 nm based on our PALS and SSA data. We observed that the average Amide I/mineral ratio values and their ranges decrease as a function of tissue age. Finally, we found that bone has Amide I/mineral domain size around ~50 to 500 nm, which agrees with the length scale of the nanomechanical heterogeneity. Future research directions should focus on combining nanoindentation, PTIR and PALS for the same sample to highlight how disease and/or genetic mutation can affect nanoscale mechanical, chemical and structural aspects in bone and how these three properties are correlated.

4.2 Summary of key findings

The hierarchical structure of collagen and mineral components in bone have been extensively studied by various techniques such as AFM, SEM, TEM and XRD. However due to the spatial resolution limitations of readily available characterization techniques to probe pores (μ-CT) and chemical composition (FTIR or Raman spectroscopy), understanding nanoscale porosity and chemical composition has been restricted. Now with three novel characterization techniques (PALS, AFM-IR and O-PTIR), it is possible to explore new porosity and chemical compositional information in bone.

4.2.1 Hierarchical nature of nanoscale porosity in bone revealed by positron annihilation lifetime spectroscopy

PALS has been employed to characterize nanoscale porosity in ceramic and semi-conducting fields for over five decades. However, to our best knowledge, this is the first application of PALS for bone. We identified pores with mean diameter of 0.6 nm that suggest porosity within the collagen molecule regardless of the presence of mineral and/or water. After the dehydration process, we found three additional pore sizes; mean diameters of 1.1 nm, 1.9 nm, and 4.0 nm—spaces that are hypothesized to associate with inter-collagen molecular spaces, terminal segments (d-spacing) within collagen microfibrils, and interface spacing between collagen and mineral structure, respectively. We provide a completely independent analysis of the average spacing between the nanoscale mineral plates (5-6 nm) using PALS and another fully independent analysis method using the specific surface area (SSA) of deproteinized samples. We show that the nanoscale pore structure surrounding the mineral structure is interconnected after the deproteinization process, suggesting that the nanoscale mineral structure is interconnected rather than constructed in a parallel fashion, which is the more conventional model of the mineral

structure in bone. This finding is supported by an independent electron microscope study probing nanoscale mineral structure by Reznikov et al.[1] recently published in Science.

4.2.2 Atomic force microscopy-infrared spectroscopy (AFM-IR) and optical photothermal infrared spectroscopy (O-PTIR) characterization of wild type mice femurs

This is the first study to combine AFM-IR with the bone samples with fluorescence marks indicating specific tissue ages. Thus, we can understand how the Amide I/mineral ratio values behave as a function of different tissue ages. We found that with the Amide I/mineral ratio values from individual full IR spectra, the IR ratio values decreased rapidly around Week 1 tissue age. After the Week 1 tissue age, the IR ratio values remain constant. This finding was in agreement with our own Raman data and Raman data from Sinder et al.[2]. In addition to the Amide I/mineral ratio value changes over tissue age, the AFM-IR data exhibited decreased IR ratio variation (shown by the box width changes) as tissue became more mature, which Raman spectroscopy or other conventional FTIR techniques cannot detect. We calculated the domain size range from the Amide I/mineral IR ratio maps acquired by AFM-IR. Our domain size analysis obtained from the IR ratio maps displayed the diameter range from ~50 to 500 nm, which agrees with the length scale of the nanomechanical heterogeneity by Tai et al.[3] Our linear mixed effect model analysis showed there was no significant Amide I/mineral average difference among the four tissue ages, considering all IR ratio values from different locations and animals. However, our box plots from individual animals showed significant location to location and animal to animal chemical variations of the Amide I/mineral ratio values.

4.3 Future Directions

4.3.1 Different genotype animal samples characterized by positron annihilation lifetime spectroscopy

Chapter 2 was only concerned with characterizing porosity profile for healthy bone samples. The next step for this project is to move onto animal samples with different genotypeand disease and discover how the genetic modifications and disease affect porosity in bone. We have preliminary data showing statistically significant pore differences between wild type and Osteogenesis Imperfecta (OI) mice samples. This specific OI mutation (known as Brtl[4]) affects singe amino acid at 349^{th} position per single collagen molecule. PALS data from Brtl OI samples could elucidate how the genetic modification affects the triple helical structure of collagen molecules. Among different animal models that mimic OI conditions, there are two available animal models that affect two different pore sites in the collagen structure in bone; 1) PPIB OI model[5] that impairs 3-hydroxylation of collagen molecule 2) C-propeptide defected OI model[6] that alters the terminal end of the collagen molecule. Both models potentially affect 1.1 nm (inter-collagen molecular spaces) and 1.9 nm (terminal segments (d-spacing)). PALS results from the three OI models can elucidate how each genetic modification would affect three pores sites identified by PALS study in Chapter 2.

Another important aspect for the future direction of the PALS project is to study the relationship between nanoscale porosity changes and local mechanical properties. Since PALS is an inherently local measurement, a conventional bulk mechanical testing such as 3-point bending would not be appropriate. To measure localized mechanical properties of bone, two main methods are used: AFM-based nanoindentation[3]; and conventional nanoindentation[2]. If one

can isolate or mark a smaller region of interest for PALS prior to the nanoindentation, it would be possible to correlate the nanoscale porosity and mechanical property changes.

To estimate the mechanical properties of mineralized collagen fibrils where the mechanical properties are difficult to determine by the nanoindentation, simulations have been utilized. The Buehler group at MIT estimated mechanical properties of pure collagen microfibrils[7] and mineralized collagen fibrils.[8] PALS can provide two types of pore information (pore size and pore population) for intra collagen molecule, inter collagen molecule, two terminal ends within collagen microfibril, the interface between the collagen and mineral structure, and spacing between two mineral plates in bone. If there are nanoscale pore size changes induced by disease and genetic mutation, it is possible to estimate how the nanoscale structure of the collagen microfibrils and/or mineralized collagen fibrils are affected and plausible to estimate the mechanical property differences caused by the structure changes. If diseases and genetic mutations do not inducepore size changes but show different pore populations, it is plausible to determine whether an increasing number of pores for a particular bone structure are sufficient to lead to a critical pore size and an eventual crack propagation, weakening the bone mechanical properties.

4.3.2. Obtaining nanoscale mechanical maps for bone samples

We found that the Amide I/mineral ratio values and their frequency maps do not correlate. The Bruker NanoIR 3 in our lab is equipped with Lorentz Contact Resonance (LCR) imaging mode[9] which uses the Lorentz force to generate oscillation instead of IR induced thermal expansion and contraction by the QCL laser. Alternatively, one can use a bone sample with a fiducial mark and image the bone with AFM-based nanoindentation, followed by

AFM-IR chemical imaging to see if there are any correlations between nanoscale mechanical maps and chemical map for the same region of interest.

In this thesis, two types of bone samples were separately measured by PALS and two PTIR techniques. Chapter 2 and Chapter 3 established experimental setup, condition, procedure, data processing, and data analysis methods. In these chapters, data is presented describing nanoscale porosity and Amide I/mineral domain size range for healthy bone samples. Future research directions should combine nanoindentation, PTIR, and PALS for the same sample to highlight how disease and/or genetic mutations can affect nanoscale mechanical, chemical and structural aspects in bone and how these three aspects are related.

4.4 References

[1] N. Reznikov, M. Bilton, L. Lari, M.M. Stevens, R. Kröger, Fractal-like hierarchical organization of bone begins at the nanoscale, Science. 360 (2018) eaao2189.

[2] B.P. Sinder, W.R. Lloyd, J.D. Salemi, J.C. Marini, M.S. Caird, M.D. Morris, K.M. Kozloff, Effect of anti-sclerostin therapy and osteogenesis imperfecta on tissue-level properties in growing and adult mice while controlling for tissue age, Bone. 84 (2016) 222–229.

[3] K. Tai, M. Dao, S. Suresh, A. Palazoglu, C. Ortiz, Nanoscale heterogeneity promotes energy dissipation in bone, Nat. Mater. 6 (2007) 454–462.

[4] A. Forlino, F.D. Porter, L. Eric J, H. Westphal, J.C. Marini, Use of the Cre/lox recombination system to develop a non-lethal knock-in murine model for osteogenesis imperfecta with an α1(I) G349C substitution. Variability in phenotype in BrtlIV mice, J. Biol. Chem. 274 (1999) 37923–37931.

[5] W.A. Cabral, I. Perdivara, M.A. Weis, M. Terajima, A.R. Blissett, W. Chang, J.E. Perosky, E.N. Makareeva, E.L. Mertz, S. Leikin, K.B. Tomer, K.M. Kozloff, D.R. Eyre, M. Yamauchi, J.C. Marini, Abnormal Type I Collagen Post-translational Modification and Crosslinking in a Cyclophilin B KO Mouse Model of Recessive Osteogenesis Imperfecta, PLoS Genet. 10 (2014).

[6] K. Lindahl, A.M. Barnes, N. Fratzl-Zelman, M.P. Whyte, T.E. Hefferan, E. Makareeva, M. Brusel, M.J. Yaszemski, C.J. Rubin, A. Kindmark, P. Roschger, K. Klaushofer, W.H. Mcalister, S. Mumm, S. Leikin, E. Kessler, A.L. Boskey, Ö. Ljunggren, J.C. Marini, COL1 C-propeptide cleavage site mutations cause high bone mass osteogenesis imperfecta, Hum. Mutat. 32 (2011) 598–609.

[7] A. Gautieri, S. Vesentini, A. Redaelli, M.J. Buehler, Hierarchical structure and nanomechanics of collagen microfibrils from the atomistic scale up, Nano Lett. 11 (2011) 757–766.

[8] A.K. Nair, A. Gautieri, S. Chang, M.J. Buehler, Molecular mechanics of mineralized collagen fibrils in bone, Nat. Commun. 4 (2013) 1724–1729.

[9] B. Lee, C.B. Prater, W.P. King, Lorentz force actuation of a heated atomic force microscope cantilever, Nanotechnology. 23 (2012).

Appendices

Appendix A

Hierarchical Nature of Nanoscale Porosity in Bone Revealed by Positron Annihilation Lifetime Spectroscopy

In collaboration with Prof. David W. Gidley*, Dr. Aaron W. Thornton, Dr. Antek G. Wong-Foy, Prof. Bradford G. Orr*, Prof. Kenneth M. Kozloff, Prof. Mark M. Banaszak Holl[6*]

Experimental Schematic

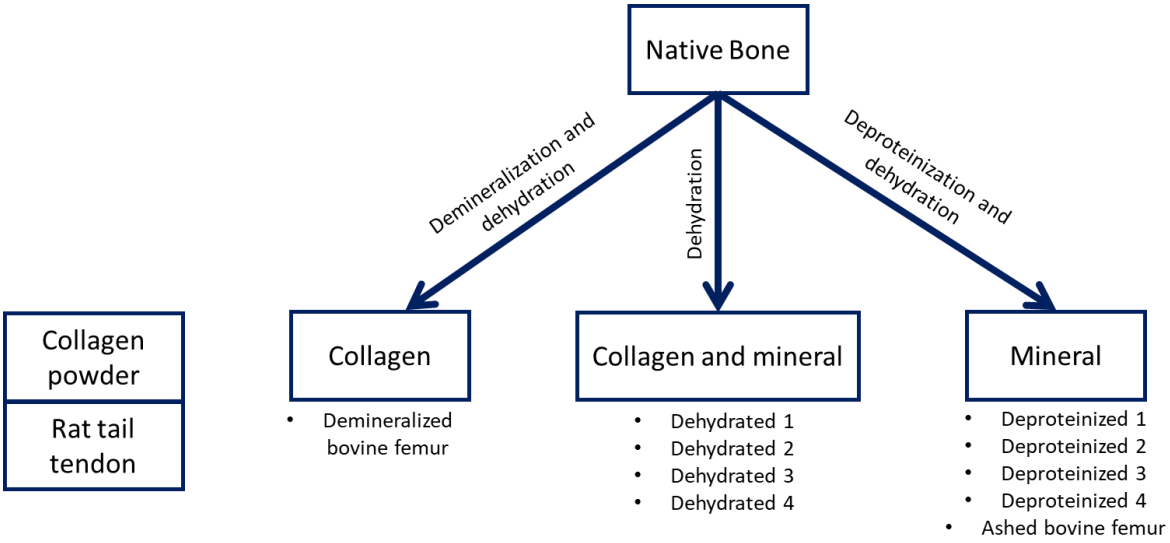

Figure A.1 An experimental schematic showing how each desired component of bovine cortical femur bone was obtained.

A.1 Deduced mineral plate thickness based on PALS data and volume fraction of water, collagen and mineral

The weight of water component in bone was the weight difference between the fully hydrated and dehydrated conditions. The weight difference between the dehydrated and

deproteinized (fully dehydrated) conditions gave the weight of collagen component. The weight of the sample after deproteinization with dehydration was the weight of pure mineral, assuming no residual protein remained in bone. For this study, bone volume was utilized to calculate the volume factions of each component since the bone volume provided volume from physical material excluding voids created by cracks inside bone. A caliper measurement for each chemical state provided similar measured volume values compared to the micro-CT measurement. The density of the fully hydrated bovine femur was 2.03 g/cm^3. The measured weight values for each component were converted into the volume values by utilizing the known densities of water (1.0 g/cm^3), collagen (1.3 g/cm^3) and mineral (3.16 g/cm^3). The total volume summed from the converted volumes should theoretically equal to the measure total volume. However, the calculated total bone volume was around 91%. The discrepancy between the calculated and measured total bone volume is explained further in the discussion section.

Table A.1 Summary of mass and bone volume of fully hydrated, dehydrated and deproteinized bovine femur.

	Weight (g)	Measured bone volume by micro-CT (mm^3)
Fully hydrated (total bone weight)	0.7517	370
Dehydrated	0.6606	342
Deproteinized with drying	0.5887	367

Dehydration condition for dehydrated and deproteinized samples: drying at 80 °C under vacuum for overnight

A.2 Estimate of positronium diffusion length, ℓ, in deproteinized bone

A randomly diffusing particle with MFP = 10 nm will diffuse after N total collisions a distance of

$$l = MFP\sqrt{N/3}$$

For Ps with a mean velocity of v and a lifetime of τ ~100 ns the total number of collisions in one lifetime is

$$N = \frac{v\tau}{MFP}$$

The thermal velocity of Ps at room temperature is ~ 8 x 10^6 cm/sec and therefor the thermal diffusion length of Ps in deproteinized bone is ~ 5 μm. This would be a lower limit on ℓ since thermal velocity is a minimum estimate on the Ps velocity amongst the mineral plates.

A.3 PALS results on ashed bovine femur sample and a proposed schematic showing how the nanoscale mineral structure might change under the high heat condition

When the additional 2% of water weight is removed after the ashing process (the mineral content is 66%), the deduced values of X_{slab} from both intact and granulated ashed bone samples are 2.5 times larger than the chemically deproteinized (100 °C dried) sample and the fitted Ps intensity values from the ashed samples are 3 times lower (Table A.2). The intact sample has its macroscopic sample size nominally consistent with the original bone volume, suggesting that there is an internal microscopic rearrangement of the mineral plates while still conserving the total macroscopic pore void volume. A granulated sample (10-100 μm particle size) exhibited the same Ps intensity and lifetime compared to the intact ashed sample, consistent with the length scale of the internal rearrangement being at the microscopic level. This factor of ~3 drop in Ps intensity with a concomitant increase in X_{slab} for the ashed samples in Table A.2 suggests that several adjacent mineral plates (nominally a 3-plate cluster) (Figure A.2**)** are collapsing together to reduce the mineral plate surface area by a factor of ~3 while increasing the average cluster-to-cluster spacing by the same factor. This is fully consistent with observation of the mineral

"densifying" wherein the specific surface area of the mineral structure decreases at ashing temperatures >500 ˚C.[1]

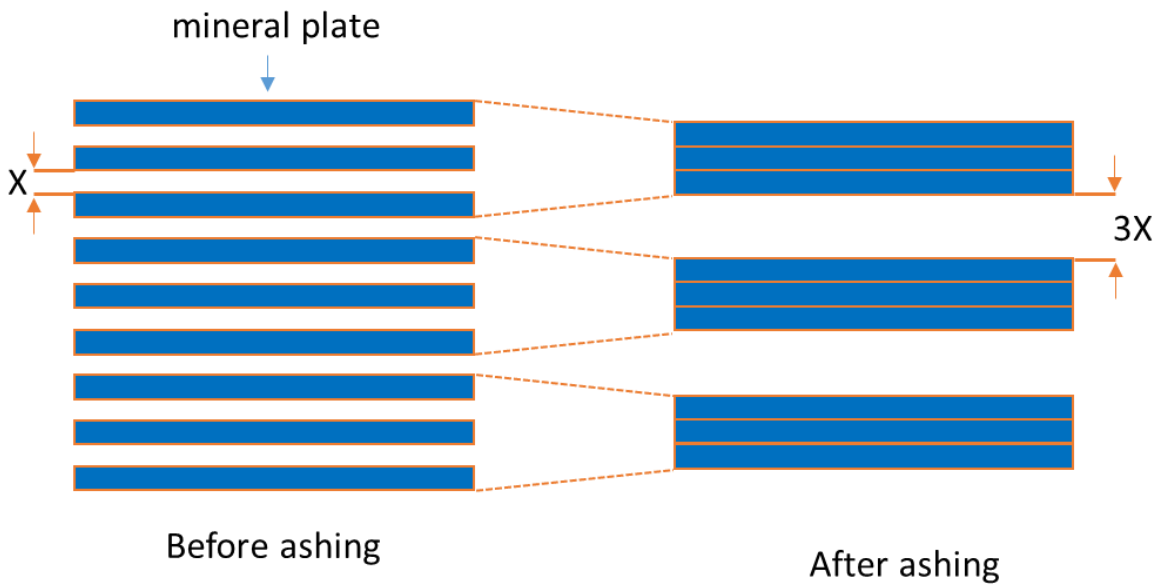

Figure A.2 A proposed mineral plate spacing change before and after ashing at 600 °C of bovine femur. The 600 °C ashed sample has the average plate spacing, X, which is about 3 times larger than deproteinized and dehydrated sample and Ps intensity which is about 3 times lower.

Table A.2 Summary of Ps lifetime components and corresponding pore sizes based on different geometries from ashed and chemically deproteinized samples.

Sample	Ps lifetime	Ps intensity	X_{slab}	$D_{cylinder}$	D_{sphere}
600 °C ashing (intact)	124.1±0.4 ns	3.4 %	11.3 ±0.3 nm	22 nm	32 nm
600 °C ashing (granulated)	125.0±0.3 ns	3.7 %	12.0 ± 0.3 nm	23 nm	33 nm
Chemically deproteinized 100 °C dehydrated	101.3±0.3 ns * mean or peak	11.3 %	4.8 ± 0.4 nm	8.4 ± 0.1 nm	12.1 ±0.1 nm

*Value of weighted mean of a bimodal lifetime distribution or the peak lifetime of a continuum distribution

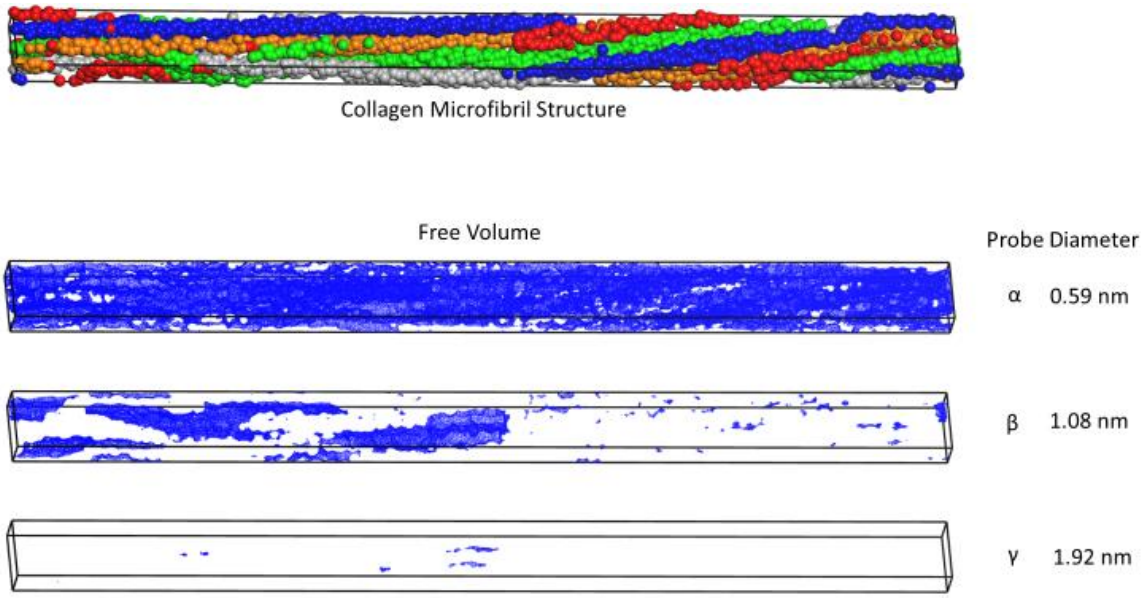

Figure A.3 Visualization of free volume for each lifetime component (α, β and γ). The top image is the constructed collagen microfibril structure based on the known collagen structure. The below three images spatially represent free volume (highlighted as blue) based on the three different probe diameter values; 0.59 (α indicates pores within collagen molecule), 1.08 (β indicates pores between collagen molecules) and 1.92 ns (γ indicates pores located at the terminal segments within the collagen microfibril) diameter sizes are selected based on the experimentally determined pore sizes by the PALS data.

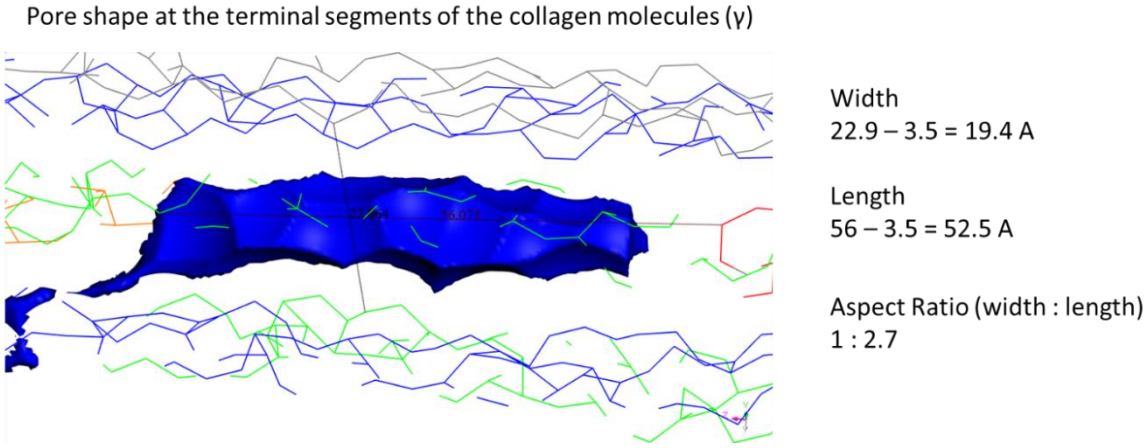

Figure A.4 Visualization of a pore shape at the terminal segments of the collagen molecules (noted as γ). The aspect ratio (width over length) of the pore suggests that the pore shape at the terminal segments is more likely to be a cylindrical model.

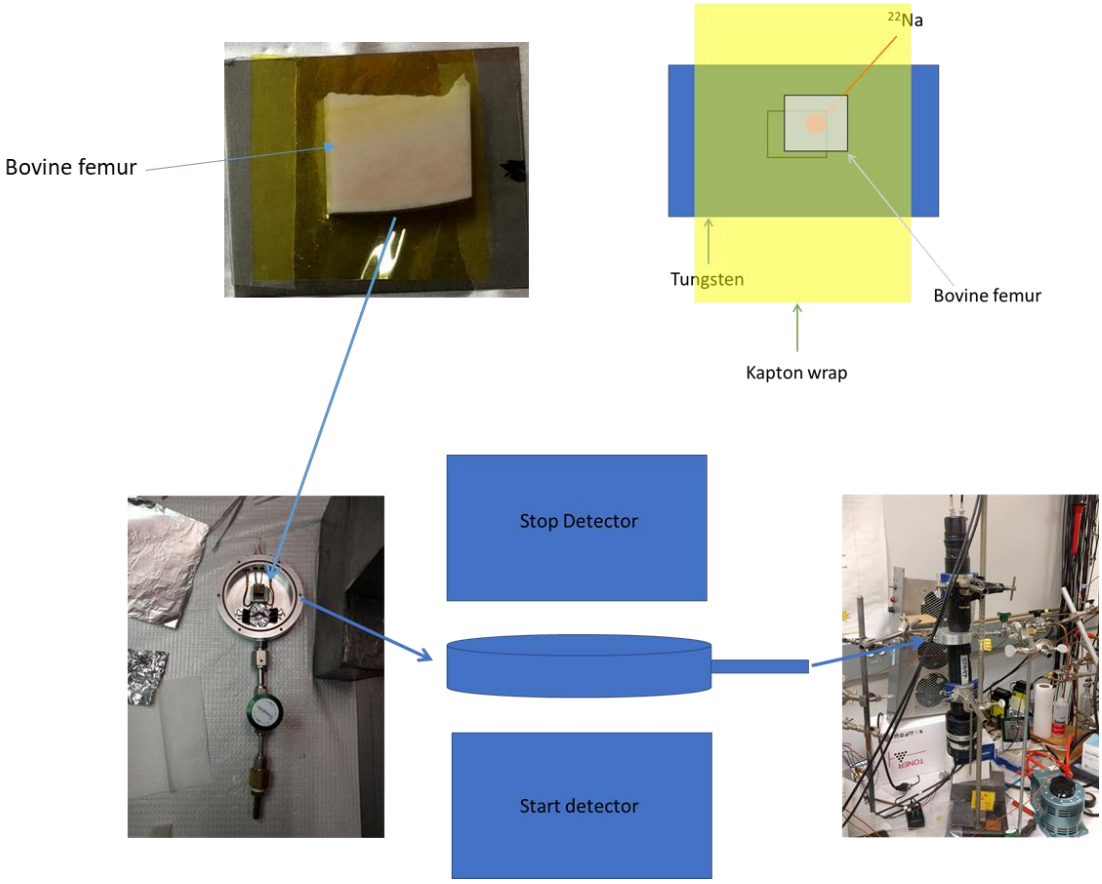

Figure A.5 Overall schematic showing how a bone sample is loaded in the sample chamber with the Kapton wrap to prevent radioactive contamination. The picture on bottom right shows the instrumentation setup to collect PALS signal.

A.4 References

[1] A.S. Posner, R.A. Beebe, The surface chemistry of bone mineral and related calcium phosphates, Semin. Arthritis Rheum. 4 (1975) 267–291.

Appendix B

Atomic Force Microscopy-Infrared Spectroscopy (AFM-IR) and Optical Photothermal Infrared Spectroscopy (O-PTIR) Characterization of Wild Type Mice Femurs

In collaboration with Max Jueckstock, Dr. Diana Dillstrom, Dr. Gurjit S. Mandair, Dr. James Henderson, Dr. Benjamin P. Sinder, Prof. Kenneth M. Kozloff*, Prof. Mark M. Banaszak Holl*

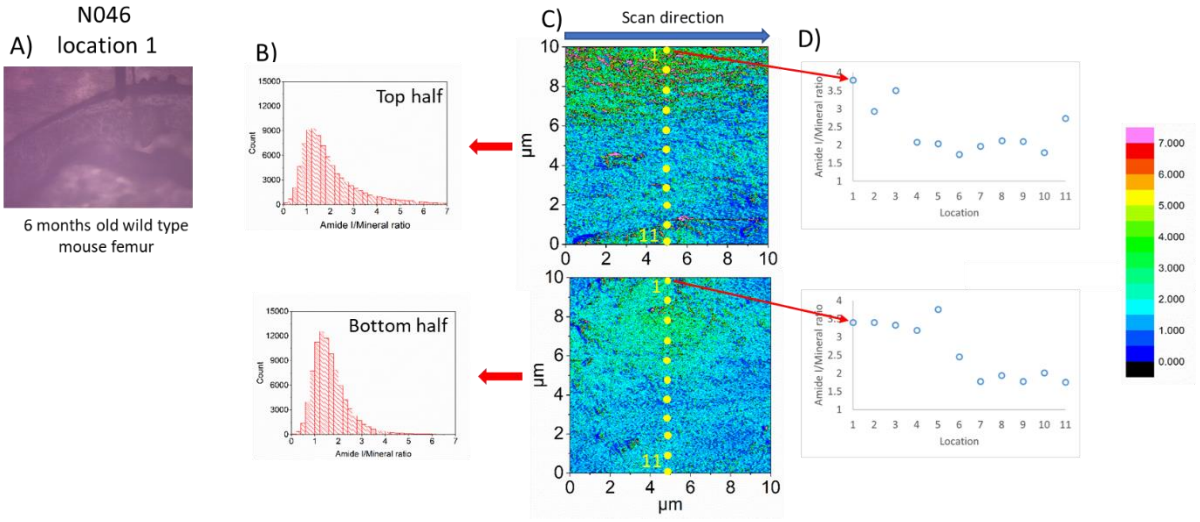

Figure B.1 Amide I/mineral ratio (1666 cm^{-1})/(1042 cm^{-1}) maps for 6-month-old wild type mouse femur. A) Optical image of obtained from AFM-IR microscope. B) Histograms derived from Amide I/mineral ratio map C) Amide I/mineral IR ratio maps D) Scatter plot of Amide I/Mineral ratio values obtained from independently measured IR spectra taken at locations indicated by the yellow circles. The ratio values obtained from the spectra are in good agreement with the ratio values obtained from the two single wavenumbers employed when obtaining the IR ratio map. This data set was collected on a Bruker nanoIR3 instrument.

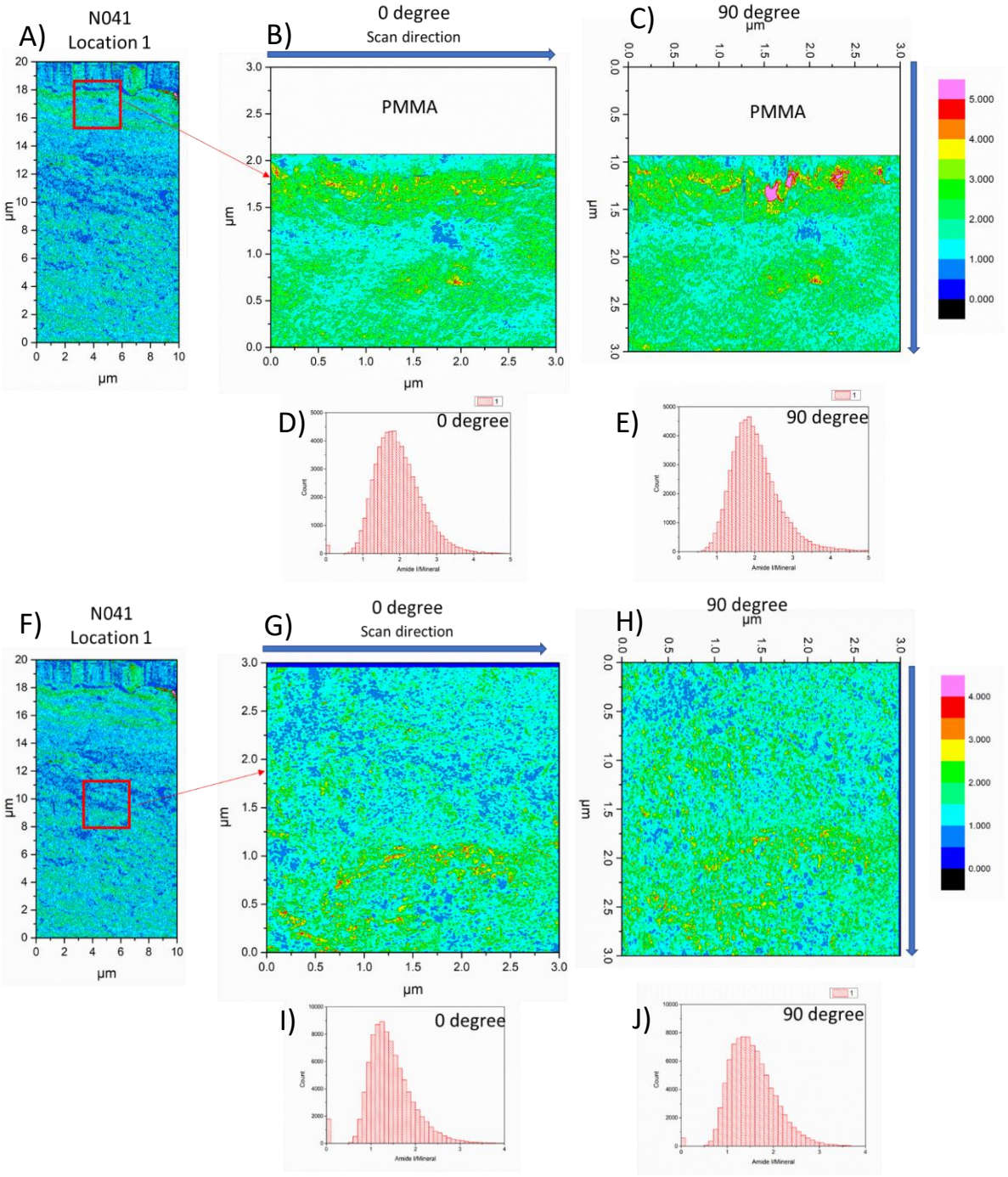

Figure B.2 Amide I/mineral ratio (1676 cm^{-1})/(1080 cm^{-1}) maps as a function of scan angle obtained using AFM-IR. A) IR ratio map B-C) IR ratio maps obtained at 0-and 90-degree scan angles. D-E) Histograms of Amide I/mineral ratio for 0-and 90-degree scan angles. F) IR ratio map G-H) IR ratio maps obtained at 0-and 90-degree scan angles. I-J) Histograms of Amide I/mineral ratio for 0-and 90-degree scan angles.

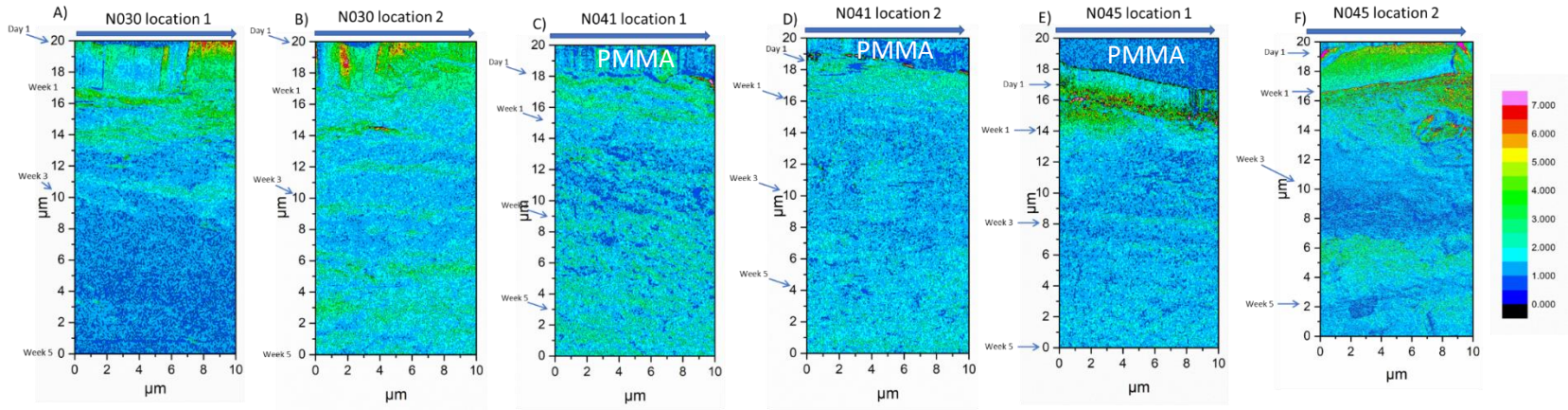

Figure B.3 Amide I/mineral ratio maps obtained by AFM-IR. These 6 images represent and share the same IR ratio values used for creating the box plots in Figure 3.6.

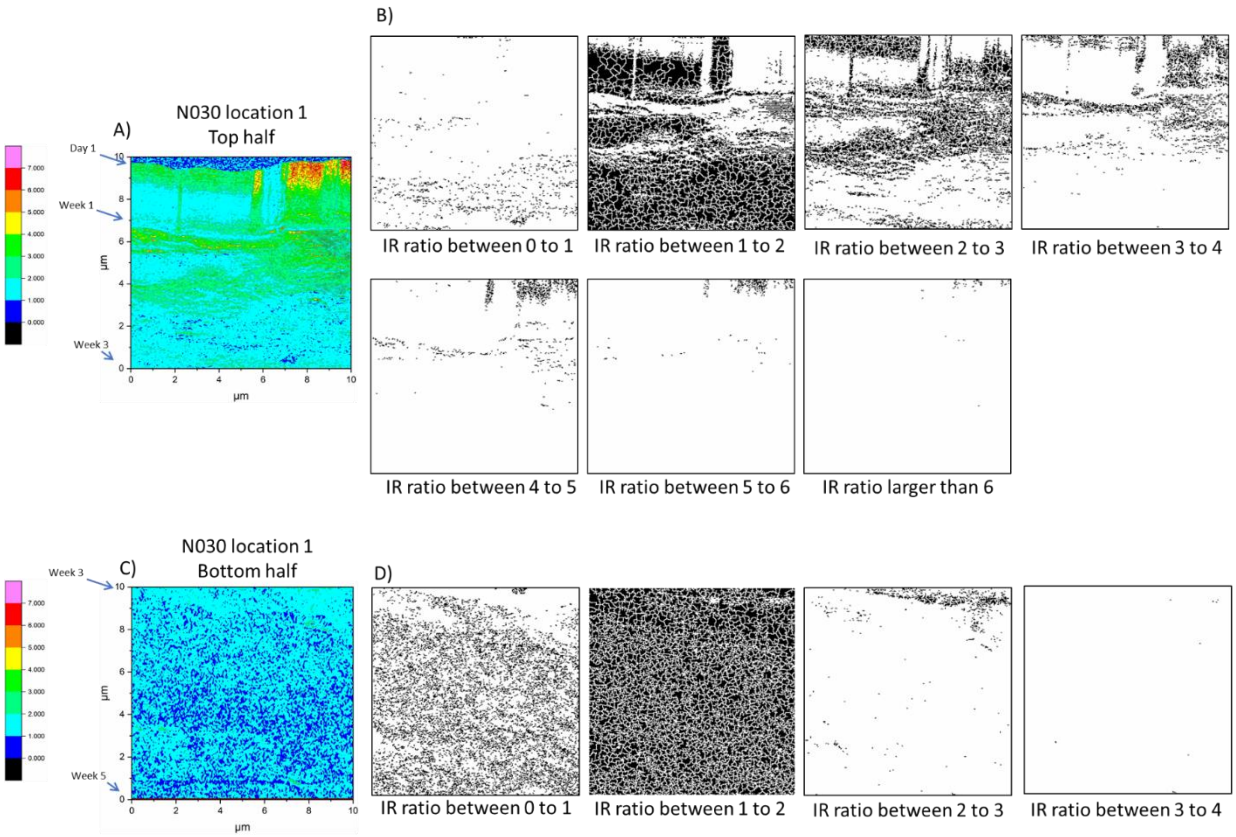

Figure B.4 Amide I/mineral ratio (1676 cm^{-1})/1080 cm^{-1}) maps obtained using AFM-IR. Panel A) and C) are the top half and bottom half images of N030 location 1 found in Figure 5 and 7. For the top half image in panel A), the PMMA portion is cropped for panel B) to avoid including PMMA the domain analysis. Panel B) and D) show images thresholded by watershed analysis. The block regions are the region of interest for each IR ratio image and measured by Fiji. Panel D) has only four images since there are no IR ratio values larger than 4 for the bottom half IR ratio map of N030 location 1. The 10 by 20 µm region is divided into two 10 by 10 µm images to maintain the identical x and y step size during the IR data collection.

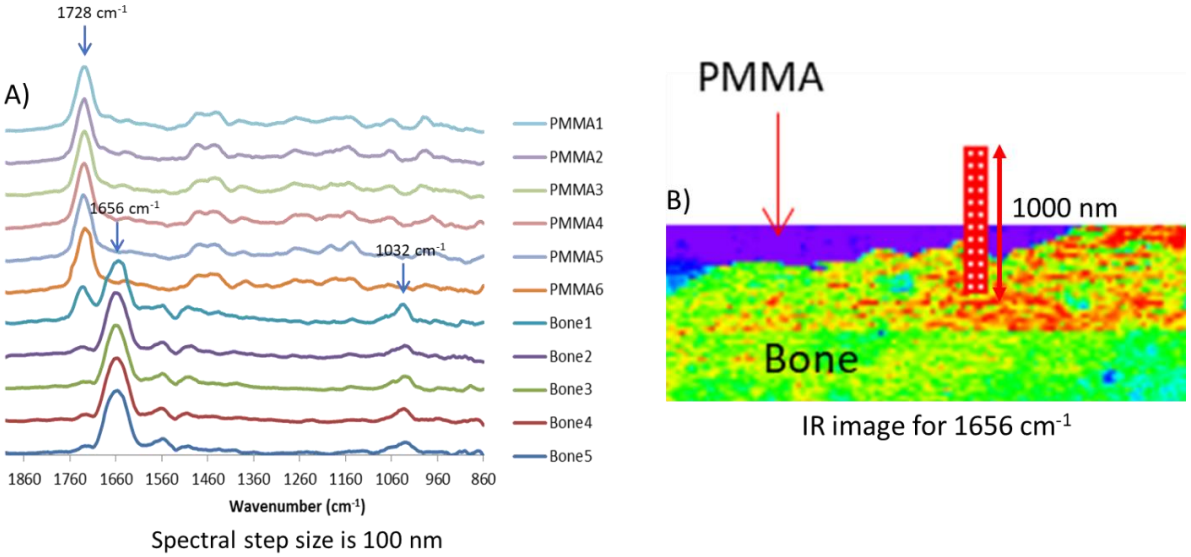

Figure B.5 Assessment of the transition between the bone specimen and the poly(methylmethacrylate) (PMMA) embedding plastic. A) IR spectra collected by AFM-IR on the interface between PMMA and bone. B) Series of red square with step size of 100 nm indicate locations of IR spectra from panel A) overlaid on single wavenumber (Amide I - 1656 cm^{-1}) intensity map obtained by AFM-IR. Day 1 data were selected by looking for the presence of the red dye in the fluorescence microscope image and then confirming the disappearance of the PMMA embedding plastic and the appearance of the collagen-related Amide I feature (~1656 cm^{-1}) peak and mineral derived phosphate feature (~1032 cm^{-1}).

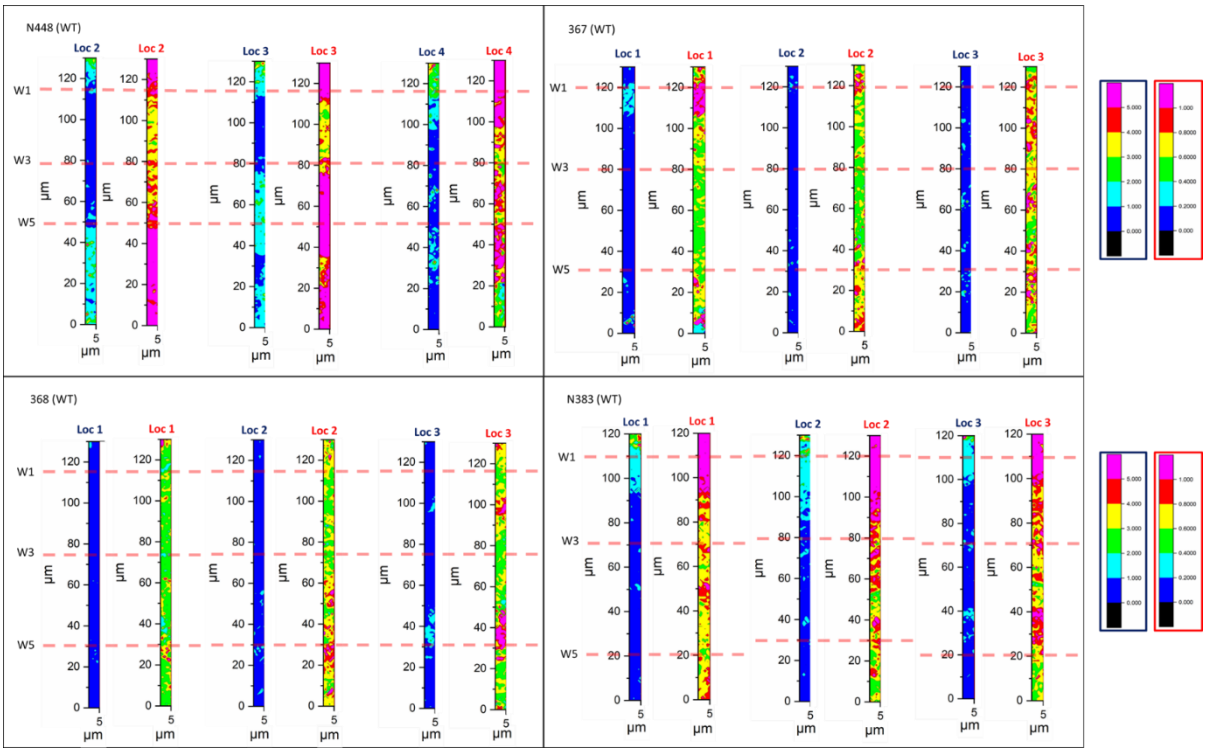

Figure B.6 Amide I/mineral ratio (peak area 1694 to 1626 cm^{-1})/(peak area 1130 to 900 cm^{-1}) maps. The ratio maps, derived from OPTIR hyperspectral data sets, are shown using two different color scales so as to highlight the overall matrix/mineral ratio changes (identified by blue sample IDs and blue scale bar) as well as the matrix/mineral ratio changes between 0 and 1 (identified by the red sample IDs and red scale bar).

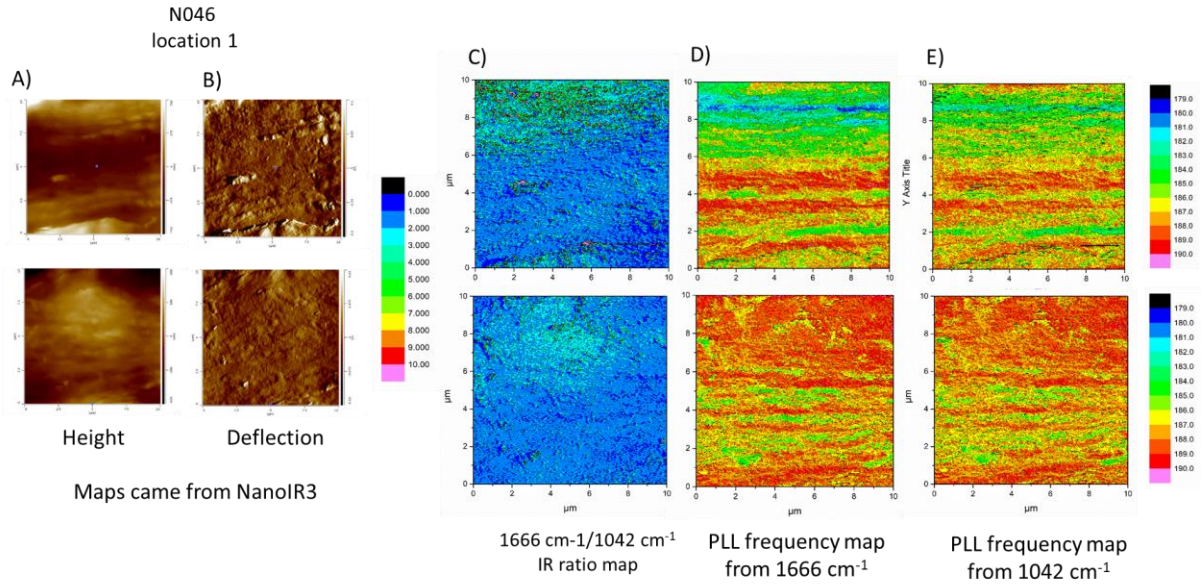

Figure B.7 Amide I/mineral ratio (1666 cm^{-1})/(1042 cm^{-1}) maps and frequency maps for 6-month-old wild type mouse femur. A) AFM height images for N046 location 1 B) Deflection images C) Amide I/mineral ratio images D) Frequency images set for 1666 cm^{-1} wavenumber E) Frequency images set for 1042 cm^{-1} wavenumber. Regardless of which wavenumber is selected to measure frequency changes, frequency maps with different wavenumbers should be consistent since stiffness as a material property should not change as a function of different wavenumbers.